Multiscale global atmospheric transport and convective precipitation

by

Daniele Rosa

A dissertation submitted in partial satisfaction of the
requirements for the degree of
Doctor of Philosophy

in

Earth and Planetary Science

in the

Graduate Division

of the

University of California, Berkeley

Committee in charge:

Professor William D. Collins, Chair
Professor Inez Fung
Professor Bruce Buffett
Professor John C. H. Chiang

Spring 2014

Multiscale global atmospheric transport and convective precipitation

Abstract

Multiscale global atmospheric transport and convective precipitation

by

Daniele Rosa

Doctor of Philosophy in Earth and Planetary Science

University of California, Berkeley

Professor William D. Collins, Chair

Freshwater from precipitation is an indispensable resource for life and a driver for many biological and geological processes. In this dissertation we present four papers and an investigation in progress using conventional and multiscale global climate models with the long term goal of understanding the physical mechanisms responsible for the observed precipitation trends and distributions. We use the multiscale model because, in contrast to conventional models, it has an explicit treatment of cloud and precipitation processes. We test the hypothesis that the multiscale approach should, in principle, generate more realistic estimates of tracer concentration and convective precipitation fields which are known to be sensitive to cloud-scale physical processes.

Atmospheric convection associated or not with precipitation produces vertical transport of surface-emitted compounds which can then affect convection itself, and hence precipitation, by altering the atmospheric radiative budget or through cloud microphysical processes. In two papers we evaluate the multiscale method on simulating the global transport of passive tracers and dust contrasting model outputs and in situ observations. We force our climate simulations with observationally derived meteorology. Therefore we can attribute the differences between the multiscale and the conventional methods to the differences in vertical transport. The multiscale model simulates realistic atmospheric concentrations of passive tracers and is, to a small degree, better than the conventional model in the lower and upper troposphere. Comparing global maps of passive tracers and dust from simulations, we find that the multiscale model simulates higher concentrations in the upper troposphere. This characteristic should emerge from the overall more efficient vertical transport from synthetic thermals in the explicit cloud treatment.

We evaluate the multiscale model and a group of the latest versions of standard climate models on the intensity distribution of precipitation. In two papers we focus our analysis on sub-daily precipitation for a highly convective region and contrast model output with observationally derived precipitation rates. The multiscale model greatly improves the simulation of convective precipitation distribution with respect to its conventional counterpart. A comparison of the precipitation efficiency between the two models suggests that the improvement

should be due to the higher rate of production of cloud water from vertical advection from the multiscale model as opposed to the rate of conversion of cloud water to precipitation from cloud microphysical processes. Extending the analysis of the precipitation intensity distribution to other state of the art climate models, we find that the models which implement mechanisms for inhibiting convective precipitation at low level of instability are more realistic.

We present work in progress where the multiscale model is the tool of choice for understanding the physical processes responsible for the observed precipitation trends in the region of the Indian monsoon and for attributing these trends to anthropogenic aerosol emissions. In addition to the realistic representation of convection and transport, the multiscale model can simulate better than other models the intraseasonal precipitation variability thought to be important for the dynamics of the monsoon.

Contents

List of Figures

List of Tables

Acknowledgments

I would like to thank my advisor Bill Collins for being an inspiring role model and supporting me. I thank the Earth & Planetary Science department people and my thesis committee members, Inez, Bruce, and John, for giving me precious advice and comments. I thank my family and my friends for keeping me company along the path.

Thank you to the people that created and participated to the Center For Multiscale Modeling of Atmospheric Processes (www.cmmap.org). Thank you to them for the financial, scientific, and technical support I received.

The work in chapter 2 is published as D. Rosa, J. F. Lamarque, and W. D. Collins. Global transport of passive tracers in conventional and superparameterized climate models: Evaluation of multi-scale methods. English. In: Journal Of Advances In Modeling Earth Systems 4 (2012). issn: 1942-2466. doi: 10.1029/2012MS000206. D. Rosa and W. D. Collins designed the numerical experiment. D. Rosa performed the model development and setup, the data analysis, and wrote the paper. J. F. Lamarque provided the chemistry module for the simulations. All authors contributed to the interpretation and final manuscript preparation.

The work in chapter 3 is published as Hsieh, W. C., D. Rosa, and W. D. Collins (2013), Global dust simulations in the multiscale modeling framework, J. Adv. Model. Earth Syst., 5, 1531, doi:10.1029/2012MS000150. W. C. Hsieh and W. D. Collins designed the numerical experiment. D. Rosa and Hsieh performed the model development and setup. Hsieh performed the data analysis and wrote the paper. All authors contributed to the interpretation and final manuscript preparation.

The work in chapter 4 is published as F.Li, D.Rosa, W. D.Collins, and M. F.Wehner (2012), Super-parameterization: A better way to simulate regional extreme precipitation?, J. Adv. Model. Earth Syst., 4, M04002, doi:10.1029/2011MS000106. D. Rosa and W. D. Collins designed the numerical experiment. D. Rosa performed the model development and setup. F. Li and M. F. Wehner performed the data analysis and wrote the paper. All authors contributed to the interpretation and final manuscript preparation.

The work in chapter 5 is published as Rosa, D., and W. D. Collins (2013), A case study of subdaily simulated and observed continental convective precipitation: CMIP5 and multiscale global climate models comparison, Geophys. Res. Lett., 40, 59996003, doi:10.1002/2013GL057987. D. Rosa and W. D. Collins designed the numerical experiment. D. Rosa performed the data analysis. All authors contributed to the interpretation and final manuscript preparation.

Chapter 1

Introduction

In this dissertation we present four papers and an investigation in progress using conventional and multiscale global climate models sharing the long term goal of understanding the physical mechanisms responsible for the observed precipitation trends and distributions. We study the atmospheric vertical transport by cloud convective processes and the character of subdaily continental convective precipitation. The importance of these investigation for understanding global climate impacts from changes in precipitation patters is presented in the following sections with references to the original papers and the corresponding chapter in this dissertation. In this section we explain why we choose the multiscale climate model.

Atmospheric cloud processes have been investigated by the scientific community for decades but they still represent the major source of uncertainty for climate projections. The challenge arises from the inherent chaotic nature of atmospheric dynamics and from the difficulty of monitoring large and fast moving systems. In the conventional approach to modeling cloud processes, the interaction of a cloud ensemble with the surrounding environment is considered and assumptions are made about dynamics and distribution of individual clouds withing the ensemble. The spatial scale of the ensemble is 100 Km whereas the spatial scale of an individual cloud is about one Km. The link between scales is accomplished through a closure assumption that is suggested by empirical evidence but uses tunable parameters which is the reason why this approach is called cloud parameterization. Nonetheless, there are at present alternatives to cloud parameterizations which have the advantage of not requiring assumption about the behavior of a cloud ensemble. This is possible because more computational power is available which allows the scientific community to use fine numerical discretizations of the atmosphere down to the scale of the individual cloud, hence cloud models where the equations of motion are more based on basic physics principles. These so called cloud resolving models are believed to be better surrogates of real systems. A promising approach for simulating the global climate that combines a model for the dynamics of the global atmosphere and cloud resolving models is the multiscale modeling framework: large-scale atmospheric processes are distretized on a coarse grid, cloud processes are discretized on a fine grid, and the two scales interact via forcing terms. The fidelity of a global climate model based on the multiscale modeling framework on simulating a realistic climate has been proven, but it has never been used to study the atmospheric vertical transport from cloud convection like we do in this work. We also study subdaily continental convective precipitation in more details than in previous work and compare the results of the multiscale modeling framework with state of the art climate models based on conventional cloud parameterization.

1.1 Atmospheric vertical transport

The composition of the atmosphere influences cloud processes but it is also determined by the mixing effect of cloud motion. In particular, cloud convection generate strong vertical transport which lifts surface-emitted compounds into the free troposphere. Therefore, to study the characteristics of cloud convection and speculate about their implications for climate due to effects on the atmospheric composition we compare concentrations of vertical profile of short-lived passive tracers and dust surface values between observationally derived and simulated data and global maps of the same simulated concentrations fields. Imposing the same large-scale meteorological flow to our simulations, differences in concentration fields should arise primarily from differences in cloud convective transport. This work is important for precipitation variability because atmospheric vertical transport of radiatively active compounds can alter the Earth's surface radiative balance, and therefore change the overall amount of moisture flux from surface evaporation which then falls as precipitation; or it can alter local atmospheric stability to convection and large scale moisture convergence, hence changing the geographical distribution of precipitation. Our studies on atmospheric transport are presented in chapters 2 and 3 and published on peer reviewed journals [105, 44].

1.2 Continental convective precipitation

Precipitation is an inherently complex process to simulate because it is also a product of some cloud processes. Nonetheless, a great effort is devoted to understanding and modeling precipitation because it is a vital resource for human activities. Convective precipitation depends on dynamics that operate at the cloud scale whereas stratiform precipitation operates at a larger spatial scale. Although both contribute to determining the overall character of precipitation, convective precipitation, particularly over land, is responsible for most of the subdaily variability. Therefore, we study the intensity distribution, the diurnal cycle, and the persistence of subdaily continental precipitation rates for a well populated area mainly exposed to high convective activity. Estimates from the multiscale modeling framework and from the the latest climate models are compared against observationally derived precipitation rates. This comparison highlights the improvements emerging from solely simulating cloud processes explicitly and the fidelity of this approach with respect to a larger group of conventional approaches. It also allows the evaluation of model assumptions regarding the physics of convective precipitation that generate more realistic estimates of precipitation rates.

Our studies on convective precipitation are presented in chapters 4 and 5 and published on peer reviewed journals [72, 104].

1.3 Monsoon precipitation

In the context of a changing climate, it is desirable to be able to attribute changes in precipitation patters to anthropogenic activity or natural variability, and make reliable projections of future precipitation patterns. Therefore, it is important that climate models can reproduce observed trends and that the physical processes responsible for such trend are identified. In the region of the Indian monsoon where about a quarter of the world rice is grown, decadal changes in precipitation trends and their negative impacts on rice production has been documented and attributed to anthropogenic emission of aerosols. Nonetheless, the debate on the contributions from the different physical processes responsible for such changes is not settled. Proposed explanations involve changes from the radiative effect of anthropogenic aerosols to local atmospheric stability, large scale circulation, or a combination of both. Our work on atmospheric transport and convective precipitation with the multiscale climate model, plus the established and almost unique ability of this model to reproduce the intraseasonal variability thought to be important for the dynamics of monsoons, allow us to plan an original numerical experiment from which we might be able to diagnose the contributions to precipitation changes from the different processes. Our study in progress on monsoon precipitation is presented in chapter 6.

Chapter 2

Global transport of passive tracers: evaluation of multi-scale methods

We test the fidelity of simulated atmospheric transport, an important process for climate, because a realistic representation of this process is necessary for realistic climate simulations. We compare a conventional and a multiscale climate model to aircraft measurements of passive tracer concentrations using a metric for the relative change with height of this field. In the next chapter we continue testing the fidelity of simulated atmospheric transport comparing simulated and observed dust concentrations.

2.1 Introduction

Accurate simulations for the transport of radiatively active atmospheric compounds are essential for the fidelity of climate projections. Reliable atmospheric transport models are also needed to determine local pollution burdens from known remote sources and to estimate the distribution of remote sources from local burdens.

Atmospheric transport from cloud convection is particularly important for the vertical distribution of short-lived atmospheric compounds such as ozone and aerosols [76, 117]. The radiative forcing by ozone is a significant driver for climate change [96], and it is also an important pollutant in the set of compounds that govern surface air quality [130]. The concentrations of tropospheric ozone and its precursors are strongly influenced by convective activity [103, 90]. Likewise, aerosols can cause large direct and indirect radiative forcings that are significant drivers of climate change, but are subject to large uncertainties due to incomplete understanding of the interactions between aerosols and other components of the the climate system like clouds and surface albedo [30]. The effects of vertical dispersal are one of the principal sources of uncertainty in these estimates of radiative forcing [108].

Generally, while large-scale flow operates from synoptic to global spatial and temporal scales, cloud convection transports atmospheric compounds from the planetary boundary layer (PBL) to the upper troposphere across vertical and horizontal spatial scales of kilometers and on time scales from hours to a day. Therefore, the horizontal and vertical distributions of passive tracers with characteristic lifetimes close to the timescales of convective activity can be highly heterogeneous in space and time and can retain a strong dependence on the distribution of sources and sinks.

The main purpose of this study is to compare global simulations of short-lived surface-emitted passive tracers performed with parameterized and cloud-resolving treatments of cloud convective transport. We evaluate the fidelity of the simulations by comparing the simulated against observed vertical concentration profiles. We conducted two simulations using the National Center for Atmospheric Research Global Climate Model (GCM) Community Atmosphere Model version 3 (CAM; Collins et al., 2006) with identical meteorological analyses but with two alternative treatments of cloud convection within each atmospheric column.

The first treatment of cloud convection is based upon an ersatz about the statistical behavior of individual convecting clouds that determines the net vertical transport of a mesoscale ensemble of convecting cloud systems [37, 140, 9]. It serves as the default treatment of cloud convection in CAM. In addition to the treatment we test here, there are several parametric formulations for treating cloud convection that are commonly used for chemical transport and climate simulations. The diversity among these representations of cloud convection is the most likely cause for much of the spread in chemical distributions [43, 141, 122].

Hence, we investigate a second treatment of cloud convection using the "Super-Parameterized" CAM (SPCAM) in which the convective transport is determined from a cloud-resolving model (CRM) embedded in CAM that explicitly simulates physical and dynamical processes at the cloud scale [60]. This treatment can in principle replace, or in practice serve as a benchmark for current cloud parameterizations since its computational cost is about two orders of magnitude higher than that of CAM.

SPCAM is a promising alternative to the current approaches for climate predictions. Atmospheric general circulation simulations using SPCAM and CAM have comparable biases in precipitation, precipitable water, top-of-the atmosphere radiative fluxes, and cloud radiative forcing with respect to observed climatologies [60, 57]. However, SPCAM exhibits more realistic diurnal variability of non-drizzle precipitation and convective intraseasonal variability than CAM. CRMs, including the one embedded in SPCAM, produce more realistic simulations of atmospheric columns forced with a variety of observed meteorological regimes compared to models utilizing conventional convective parameterizations [134, 135].

Our numerical experiments are specifically designed to understand the implications for climate and pollutant dispersion simulations by comparing SPCAM to CAM in a controlled large-scale flow. We operate both models in the Chemical Transport Model (CTM) mode in which we set the large-scale flow to observationally derived dynamic and thermodynamic fields derived from meteorological reanalysis. Therefore the lateral winds governing the transport from the large scale atmospheric flows are identical and reasonably realistic in both simulations. Feedbacks from, and hence divergent simulations due to, differences in cloud-scale convective processes are not permitted. Due to this experimental design, contrasting passive tracer distributions should arise primarily from differences in the sub-grid vertical convective transport.

It is well known that simulated concentrations of tracer compounds are sensitive to the treatment of convective processes. Differences in concentrations between simulations and observations and among simulations range from a few percent to much greater values, and in general the discrepancies are inversely proportional to the tracer lifetimes [76, 50, 29, 23, 122]. We apply the CTM framework to radon-222 (Rn) and methyl iodide (CH_3I) following previous studies ([23] and references therein). These tracers have short lifetimes that make their concentrations more sensitive to transport processes, do not evolve through complex chains of chemical reactions and do not interact strongly with the hydrological cycle. Nonetheless, our results can inform subsequent investigations about radiatively active compounds and pollutants that have lifetimes comparable to the lifetimes of the tracers used in this study but require greater modeling complexity.

To quantify the fidelity of the models to *in situ* tracer measurements, we propose a metric for the vertical profile of tracer concentrations designed to highlight differences in the effects of convective entrainment and detrainment between the two simulations.

Instead of using short-lived passive tracer concentrations to investigate vertical transport from cloud convection, one could compare the vertical velocities of convective air masses and have a more direct test for the velocity spectrum produced by convective parameterizations. Observations of these velocity fields are becoming more readily available thanks to the increasingly widespread deployment of Doppler radar instruments [86, 124], but useful data still remain relatively scarce due to the inherent difficulties of collecting these observations from aircraft in dangerous environmental conditions [67, 74].

2.2 Methods

We simulate the global transport of two passive tracers using CAM and SPCAM in CTM mode over the period 1996-2006. In these experiments, the tracers are emitted at the surface of the Earth, and the models are forced by meteorological reanalysis. Test and control simulations from SPCAM and CAM respectively are obtained by using the super-parameterized and conventional treatments of cloud convection. The volume mixing ratio (VMR) vertical profiles and Local Convective Indices (LCI) of the tracers from CAM and SPCAM are compared against observational estimates from field campaigns. The LCI measures the concentration of the tracer relative change with height to quantify the fractional changes in VMR due to entrainment and/or detrainment between convection and its surrounding environment (see section 2.2 for more details). Since the LCI is based upon relative changes in the vertical direction, it is insensitive to local errors in the absolute magnitude of modeled versus actual emissions. Outside of convective systems, the LCI measures large-scale cross-isentropic gradients in tracer concentration imposed by sources and vertical mixing upwind of the region of interest and by large-scale vertical motions resolved by the model. When possible the comparisons are *precise*, that is the simulated and observed period match exactly. Otherwise, the comparisons are *climatological*, that is the long-term simulated and observed intra-annual period match.

Global circulation model

We use the CAM version 3.5.36 from National Center for Atmospheric Research with a latitudinal and longitudinal horizontal resolution of 1.9°x2.5°, a vertical discretization of twenty-eight levels, the finite-volume dynamical core, and a time step of thirty minutes. We run CAM in CTM mode [81, 64] using six-hourly meteorological reanalysis data from the National Center for Environmental Prediction ([55]). Vertical profiles of horizontal winds and temperature, and surface values of pressure, wind stress, sensible heat flux, and water vapor flux are linearly interpolated in time and space onto the atmospheric grid of CAM. The modeled atmospheric fields are output every three simulated hours.

Planetary boundary layer and cloud convection treatments

In CAM, PBL and cloud convective processes are not resolved because its grid is too coarse to allow an explicit numerical solution. The vertical diffusive processes in the PBL and free troposphere are parameterized using local and non-local transport terms [9]. Both deep and shallow convection are parameterized as well [37, 140]. The treatment for convection in CAM is based on statistical models for a mesoscale ensemble of convective cloud systems that calculate mass vertical fluxes (up- and down-drafts) on the assumption that the cumulus ensemble consumes the atmospheric instability quantified by the convective available potential energy, with a characteristic timescale estimated from observations. Here, we refer to this treatment plus the host GCM as CAM.

In the version of CAM developed by the Center for Multi-scale Modeling of Atmospheric Processes (CMMAP[1]), cloud processes are represented using the CRM: System for Atmospheric Modeling (SAM) [59]. SAM is embedded in each atmospheric column of the GCM and coupled to the large-scale flow with relaxation terms [60]. Because in this study the large-scale flow is prescribed using the CTM framework, the cloud processes within the GCM cannot affect it.

The cloud treatment in SPCAM is more *explicit* than that in CAM because it discretizes each GCM atmospheric column on a finer grid, and therefore it can incorporate more detailed approximations of cloud convective dynamics including the anelastic approximation and a closure scheme for small-scale turbulence. When there is local adiabatic heating, the CRM embedded in SPCAM allows convective thermals of sizes comparable to real clouds to form, and the coupling with the GCM allows the large-scale flow to affect the local flow. We use a two-dimensional version of the CRM with sixty-four 2-km-wide horizontal grid cells oriented in the East-West direction within each column of CAM, a vertical grid structure identical

[1]http://www.cmmap.org

to that in CAM, and a time step of twenty seconds. Here, as in previous papers, we refer to this treatment as the SPCAM parameterization.

Chemical passive tracers

To simulate the chemical passive tracers Rn and CH_3I in CAM and SPCAM, we use the Model for OZone and Related chemical Tracers (MOZART; Emmons et al., 2010 and Lamarque et al., 2011). Since the sources and sinks of the tracers are calculated at the spatial and temporal resolution of the GCM, these operate in an identical manner in CAM and SPCAM.

The prescribed surface emission of Rn is similar to that used in other studies [e.g. 50, 23]. It is constant and non-zero only over non-frozen land. Its value is 10^4 atoms $m^{-2}s^{-1}$ between 60° S and 60° and is half that between 60° N and 70° N with no emission for Greenland. Rn decays with a lifetime of 5.51 days.

The prescribed surface emission of CH_3I is taken from *Bell et al.* [2002]. Monthly-mean fluxes of CH_3I are applied cyclically to all simulated years. Approximately 70% of the total emission is from the ocean and attains its peak values at mid-latitudes between spring and summer. About 24% of the total emission comes from rice paddies in south-eastern Asia with the largest occurring between June to October. Atmospheric CH_3I has a lifetime that varies between two and six days depending primarily on photolysis (99%) and secondarily on chemical reaction with the hydroxyl radical OH (1%).

Transport of the passive tracers

There are two types of passive tracer transports in our simulations. One is the large-scale horizontal and vertical advective transport due to horizontally divergent large-scale flow that is resolved on the GCM atmospheric grid. The other is the advective and diffusive vertical transport due to PBL and cloud convective processes that is not resolved on the GCM grid balance by either large-scale convergence or divergence.

Within each atmospheric column, the net vertical large-scale mass transport can be non-zero. While the net vertical convective mass transport is strictly zero, it can still cause considerable internal mixing and thereby alter the tracer concentrations in the GCM column. The operator of the large-scale transport is identical in both simulations [102] because the runs are performed in CTM mode with identical meteorology. The convective transport operating at the GCM sub-grid scale is radically different. The CAM parameterization described in section 2.2 represents the transport of passive constituents using a formulation consistent with the magnitude of the vertical mass fluxes diagnosed by the GCM sub-grid parameterizations [17]. For SPCAM, we have implemented the passive tracer transport using the advective and diffusive dynamics of the CRM [59] by neglecting any source or sink mechanism for the tracers at the CRM scale. Given the estimates reported in section 4 of *Khairoutdinov et at.*, [2008] , we expect at least 70% of the vertical transport to be the result of explicitly resolved advective dynamics and the remainder of parameterized diffusive fluxes. To introduce coupling between the concentrations of the tracers simulated by the

GCM and CRM, we have implemented relaxation terms for the tracer VMRs [60]. Contrary to one-way coupling applied to the meteorological fields used to drive the models in CTM mode (section 2.2), the coupling of the tracer concentration is fully bi-directional, i.e., the up-scale effects of the CRM on the tracer distributions within the parent GCM are included in our simulations.

Local Convective Index

The surface emission for the tracers prescribed in our simulations is, presumably, a highly idealized approximation of the actual heterogeneous distribution of emissions (see [6] and references therein for CH_3I, and [138] for Rn). Therefore in addition to comparing vertical profiles of the tracer VMRs, we also compare the relative change with height in VMR. Following the formulation of a similar metric of model fidelity developed by *Bell et al.* [2002] , we quantify the relative change by the Local Convective Index (LCI):

$$\mathrm{LCI} = \Delta \ln q / \Delta h, \tag{2.1}$$

where q is the VMR and h is the height above sea level. For short lived tracers like the ones used here, the LCI has proven to be a useful tool for analyzing the vertical convective transport biases of the models, although it cannot separate these from biases arising from large scale transport or source and sink processes. We calculate discrete approximations of equation 2.1 for observations and simulations using VMR values from adjacent vertical levels.

Case studies

To test the fidelity of the simulations we have used measurements from a number of field campaigns, specifically (i) PEM-Tropics A [42], (ii) PEM-Tropics B [98], (iii) ACCENT [91], (iv) TRACE-P [52], (v) Pre-AVE[2], (vi) INTEX-A [115], (vii) CR-AVE[3], (viii) INTEX-B [114], (ix) ARCTAS [51], (x) ABLE-2B [93], (xi) Rn profiles from flights originating from Moffett Field, California [63], (xii) Rn profiles from a series of campaigns over mid latitude continental land in the northern hemisphere [73], and (xiii) PBL Rn profiles in the SE Australia [131]. We have partitioned the data based on the various missions, time periods, and locations of the observations. The case studies are summarized in Table 2.1.

Precise comparisons of tracer profiles are conducted using simulated VMRs for which the model time steps and grid-point coordinates are the closest to the times and locations of the observed VMRs. Specifically, for each VMR measurement, a matching VMR value is extracted from the simulation such that its discrete location is the closest to the observational

[2] Pre-AURA Validation Experiment. http://www.espo.nasa.gov/missions.php

[3] Costa Rica Aura Validation Experiment. http://www.espo.nasa.gov/missions.php

location (with respect to latitude, longitude, and height) and its three-hourly time step is the closest to but less than the observational time. *Climatological* comparisons are similar but a simulated VMR value is taken from each simulated year by matching the relative time of year for each measurement. Note that for the case study ALLY07_NHCON_LIU (Table 2.1), the original observation time is not available for all data points, and we assume these missing times are uniformly randomly distributed between 9 a.m. and 9 p.m.. In addition, for some data points only the month in which the observations have been taken is available. For the purposes of temporal matching, we assume that dates of the measurements are uniformly distributed in that time period. Observed and simulated values are binned on discrete vertical layers of depth of 1, 3, 5, 5, and 6 Km, and midpoints at 0.5, 2.5, 6.5, 11.5, and 17 Km of altitude, respectively. We have opted for a coarse vertical grid to focus on the main feature of the profiles, and we have chosen the bins to approximately match the regions where the simulated values differ the most between models.

The biases between simulations and observed LCIs are calculated on leaps between adjacent atmospheric layers which are referred to here as Planetary Boundary Layer Leap (PBLL; 0.5–2.5 Km), Low Troposphere Leap (LTL; 2.5–6.5 Km), Mid Troposphere Leap (MTL; 6.5–11.5 Km), and Upper Troposphere Leap (UTL; 11.5–17 Km).

2.3 Results

First, we show precise and climatological comparisons between simulations and observations for the VMR vertical profiles of Rn and CH_3I . Next, we compare global and zonal climatological VMRs of the tracers.

Comparison of modeled and observed methyl iodide

The root mean square errors between modeled and observationally estimated LCIs are shown in Fig. 2.2, xv after averaging over all CH_3I field campaigns listed in Table 2.1. Our primary general is that the mean LCI biases from SPCAM are smaller than the biases from CAM for the PBLL, MTL, and UTL, but larger for the LTL; however, the statistical uncertainty is large. LCI biases are smaller for precise comparisons than for climatological ones for the PBLL and UTL, but larger for the LTL and MTL. The mean differences between the modeled and observed VMR profiles and the resulting LCI values constructed by averaging over each individual field campaign are displayed in Fig. 2.1 and 2.2. In general, both models overestimate the decrease of CH_3I VMR with altitude in every layer except for the MTL. The VMR from SPCAM and CAM profiles differ from each other from a few to tens of percent. The biases in SPCAM and CAM, which can be about one or two orders of magnitude at altitudes below 10 Km and at 18 Km, respectively, (Fig. 2.1, iv and 2.1, ix), are generally greater than the differences between the two models.

We provide more details about the comparisons in the following paragraphs and comment on some of them to highlight some peculiarities of individual or several case studies.

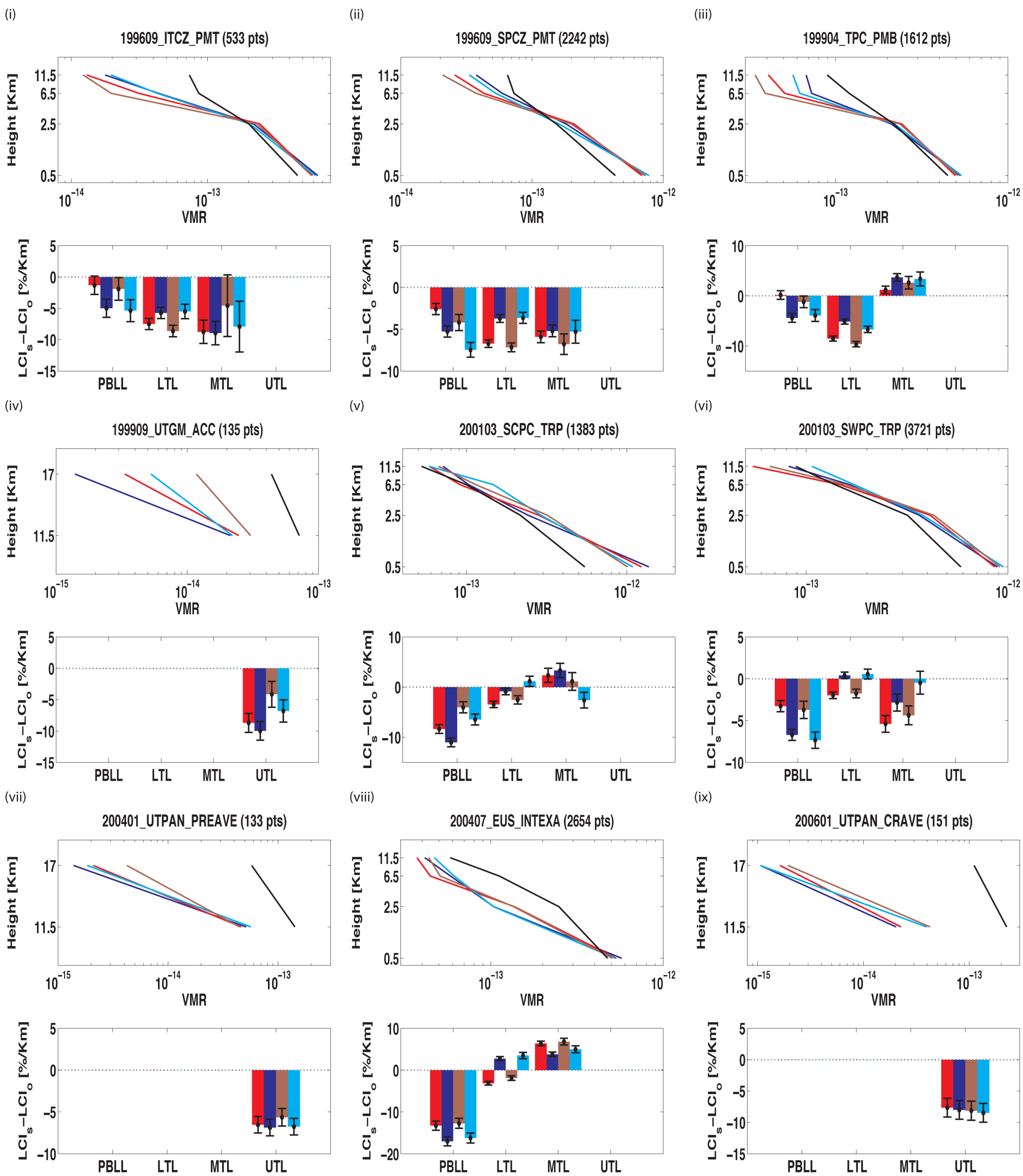

Figure 2.1: See caption of Fig. 2.2.

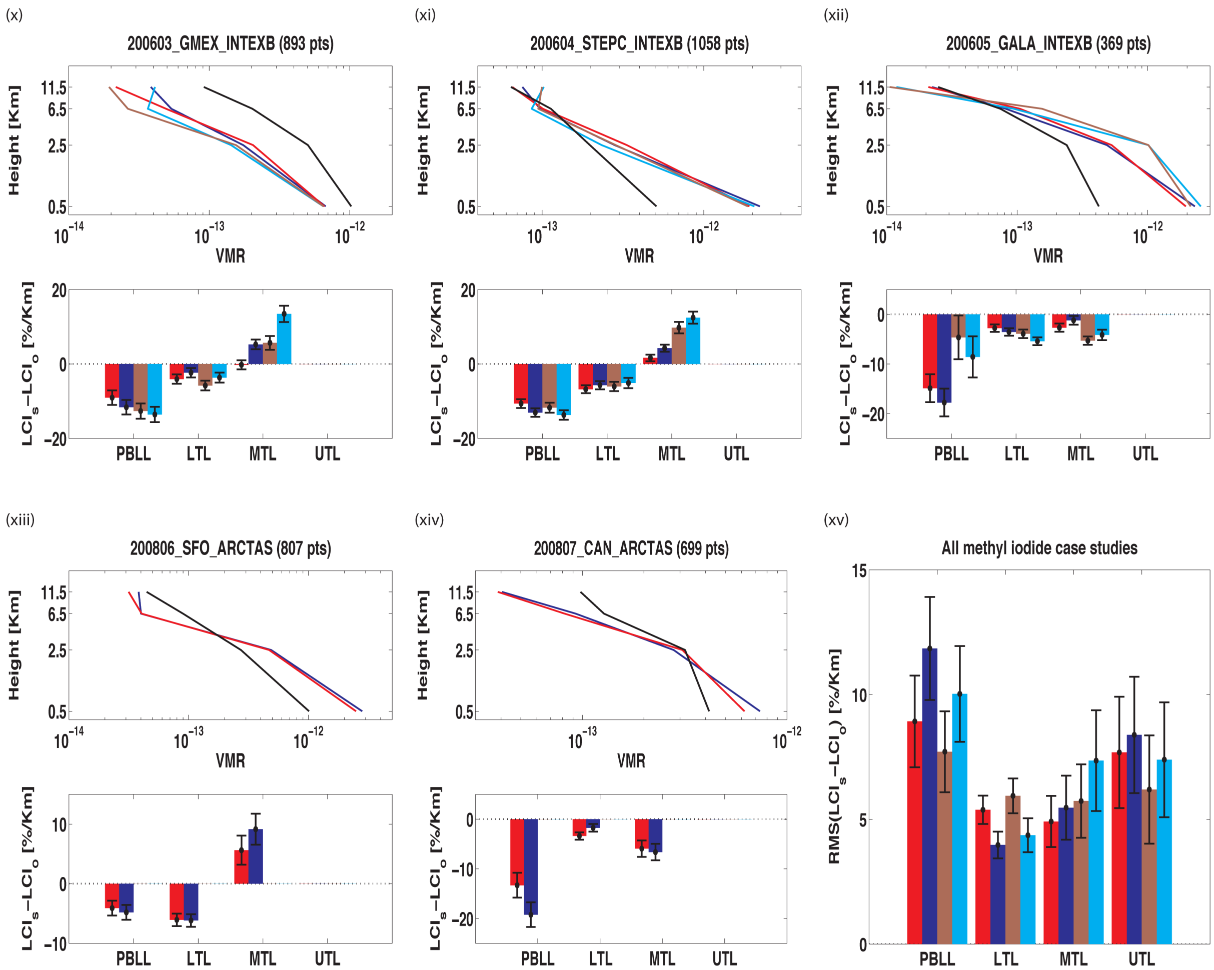

Figure 2.2: Comparisons between simulated and observed vertical profiles and LCI biases in the PBLL, LTL, MTL, and UTL for CH_3I. Climatological/precise values are shown in red/brown for SPCAM and blue/cyan for CAM, respectively. Observed profiles are shown in black. Standard errors are not shown because they are much smaller than the differences between mean values. Below each profile comparison, LCI biases are shown with bars at one standard error. Panel (xi) shows the root mean square (RMS) and its standard error for LCI biases in all the profiles.

Over the central tropical Pacific ocean and the South Pacific Convergence Zone, the models have negative CH_3I VMR biases in the mid and upper troposphere (Fig. 2.1, i,ii, and iii). The simulated profile is close to the observed one up to approximately 2.5 Km, above which it decreases quickly. The biggest LCI biases occur for the LTL, whereas the smallest ones occur in the PBLL. The LCI biases in SPCAM are smaller than those in CAM for the PBLL but bigger for the LTL.

Over the sub-tropical Pacific ocean, the models have positive CH_3I VMR biases in the low troposphere with smaller biases in the mid and upper troposphere (Fig. 2.1, v, and vi; Fig. 2.2, xi). Contrary to the case studies over the central tropical Pacific ocean and the South Pacific Convergence Zone, the biggest LCI biases occur for the PBLL whereas the smallest ones occur for the LTL. LCI biases in SPCAM are smaller than those in CAM for the PBLL but bigger for the LTL.

Over the east coast of the United States, the models have no CH_3I VMR biases in the PBL, but they have negative biases in the mid and upper troposphere (Fig. 2.1, viii). The LCI biases in both models are notably large and negative for the PBLL; LTL LCI biases are negative for SPCAM and positive for CAM, whereas MTL LCI biases are positive for both models. A possible interpretation of these features is that CAM, and to a lesser degree SPCAM, may have not enough mixing in the PBL or may be depleting the cloud layer too much between 1 and 4 Km due to excessive convective activity. Precise and climatological comparisons have comparable LCI biases.

Over the Gulf of Mexico, the models have negative CH_3I VMR biases increasing with altitude (Fig. 2.2, x). The LCI biases in SPCAM are smaller than those in CAM for the PBLL and MTL, and bigger for the LTL. Climatological comparisons have smaller LCI biases than precise comparisons, especially for the MTL.

Over the Gulf of Alaska, the models have positive CH_3I VMR biases in the PBL that decrease with altitude (Fig. 2.2, xii). The LCI biases in SPCAM are smaller than those in CAM for the PBLL, but comparable for the LTL and MTL.In the PBL, the LCI biases from the precise comparison are much smaller than the corresponding climatological biases. This case study shows that both models can respond properly to large-scale conditions and reproduce better estimates of real tracer distributions. We do not find a similar difference between precise and climatological comparisons for the other case studies possibly due to the little sensitivity of the models to or errors in the other large-scale conditions.

Over the San Francisco Bay and Canada, the models look similar. They have positive CH_3I VMR biases in the PBL and negative biases in the upper troposphere (Fig. 2.2, xiii,xiv). These are regions of low average rainfall and convective activity. Nonetheless, the LCI biases from SPCAM are smaller than those over CAM for the PBLL over CANADA (Fig. 2.2,xiv). SPCAM does not deplete the layer between 1 and 4 Km as much as CAM does, resulting in a better match with the VMR change with height of the observed tracer. This again suggests an underestimation of mixing in the PBL by CAM and, to a lesser degree, SPCAM.

For the profiles at high altitude between 9 to 20 Km, over the Central Americas, the models consistently underestimate the observed CH_3I VMR (Fig. 2.1, iv,vii; Fig. 2.1, ix). However, the VMR and LCI biases from SPCAM are smaller than those from CAM. We suspect this could be due to convective overshooting at the CRM scale, a feature that is missing in CAM. Precise comparisons have smaller LCI biases than climatological ones only for one case study (Fig. 2.1, iv).

Comparison of modeled and observed Radon

Mean VMR profiles and LCI biases for simulated Rn are shown in Fig. 2.3. For the coastal mid latitude case (Fig. 2.3, ii), climatological VMRs from SPCAM and CAM look similar. This is also the result for a CH_3I case referring to a nearby location (Fig. 2.2, xiii). We interpret the similarity of the models to lack of vertical transport by convective processes that are the primary source of the differences between simulated profiles. Rn has a longer lifetime than CH_3I, and the factors that determine LCI of the the models in the MTL are the contribution of Rn emitted upwind of the case study site in Asia and the integrated vertical and horizontal transport (results not shown; we used different tags for Rn emitted in the Americas and Eurasia). We show that the MTL LCI bias from SPCAM is slightly smaller although this result has little statistical confidence. Another continental case is a reconstruction using more heterogeneous measurements in time and space that has often been used in studies similar to ours (Fig. 2.3, iii; [73]). We assert that the similarity between models is the result of averaging across heterogeneous sampling locations. The LCI biases from SPCAM are bigger than those from CAM and the statistical confidence is even smaller than the prior case.

The remaining case studies are limited to the first 4 Km in height and refer to two climatologically very different regions. Over the wet tropical Amazon forest, models have positive Rn VMR biases (Fig. 2.3,i; for this case study, *Pereira et al.* [1991] estimated a ground flux between 1/2 and 1/3 of what we prescribed here). The LCI biases from SPCAM LCI biases are much smaller than those from CAM for the PBLL, confirming the general conclusions for the CH_3I case studies. Over the SE Australia, a region with little mean rainfall, models have negative Rn VMR biases (Fig. 2.3, iv,v, and vi). The SPCAM LCI bias is bigger than that of CAM in one case (Fig. 2.3,vi) for which precise comparisons have bigger biases than climatological ones. For the case study with the biggest measurement sample size, the PBLL LCI bias in SPCAM is smaller than that in CAM.

Global patterns from simulations

Some coherent patterns associated with the regions of cloud convective activity are evident in the differences between zonal and global time-mean distributions of Rn and CH_3I by CAM and SPCAM. We focus on the broad features for the low and mid latitudes and, implying all altitudes in an approximate sense, consider 4 vertical areas: the PBL between the surface and 1 Km, the LT between 1 and 4 Km, the MT to UT region between 4 and 12 Km, and the UT to LS region above 12 Km. In general, at latitudes where most of the convective activity occurs in the tropics and subtropics, SPCAM introduces a vertical quadrupole pattern of VMR differences relative to CAM. The quadrupole is characterized by

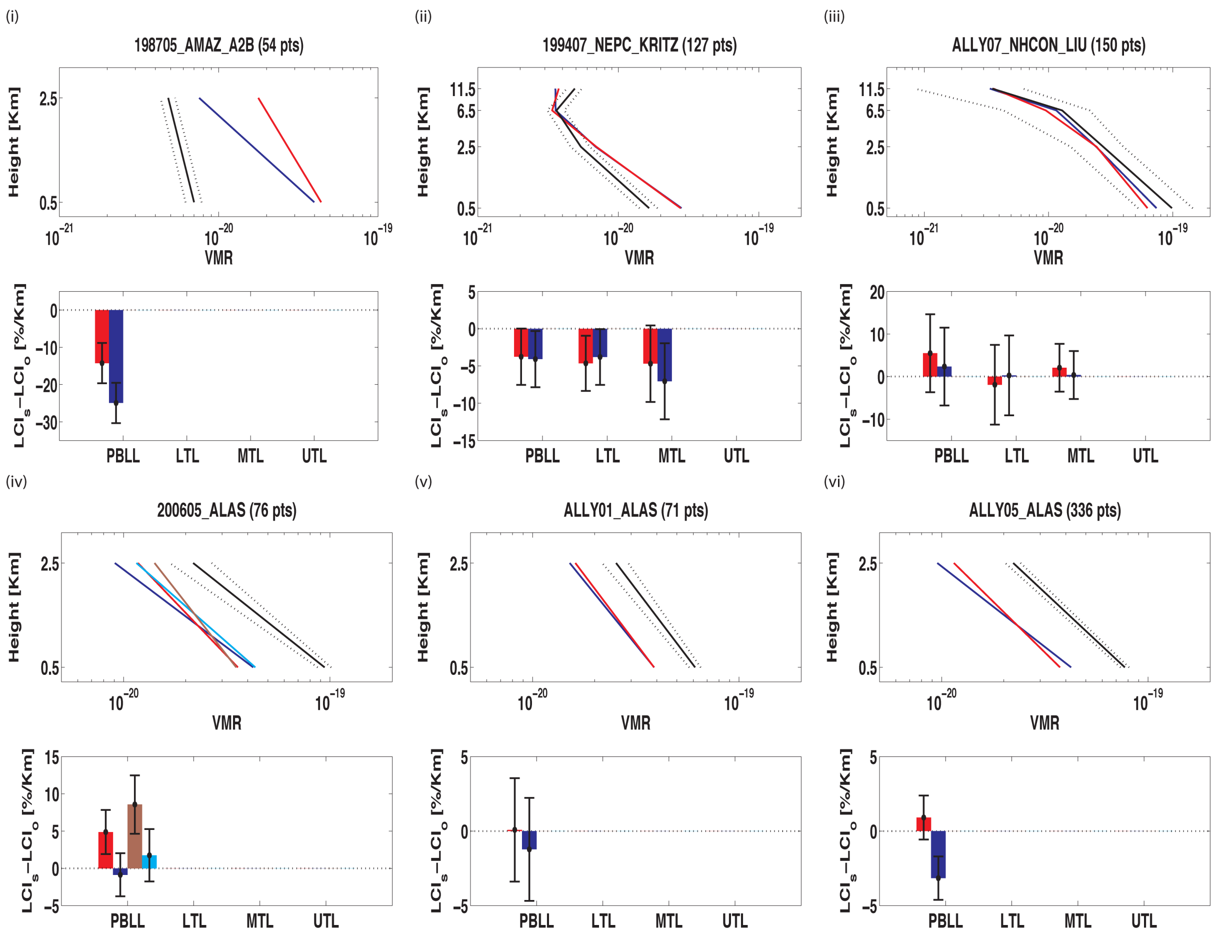

Figure 2.3: Comparisons between simulated and observed vertical profiles and LCI biases in the PBLL, LTL, and MTL for Rn. Climatological/precise values are shown in solid red/brown for SPCAM and solid blue/cyan for CAM, respectively. Observed profiles are shown in black. Standard errors are shown in dashed black and only for observed values because the standard errors for the models are much smaller than the differences between mean values. Below each profile comparison, LCI biases relative to the observations are shown with error bars in black at one standard error.

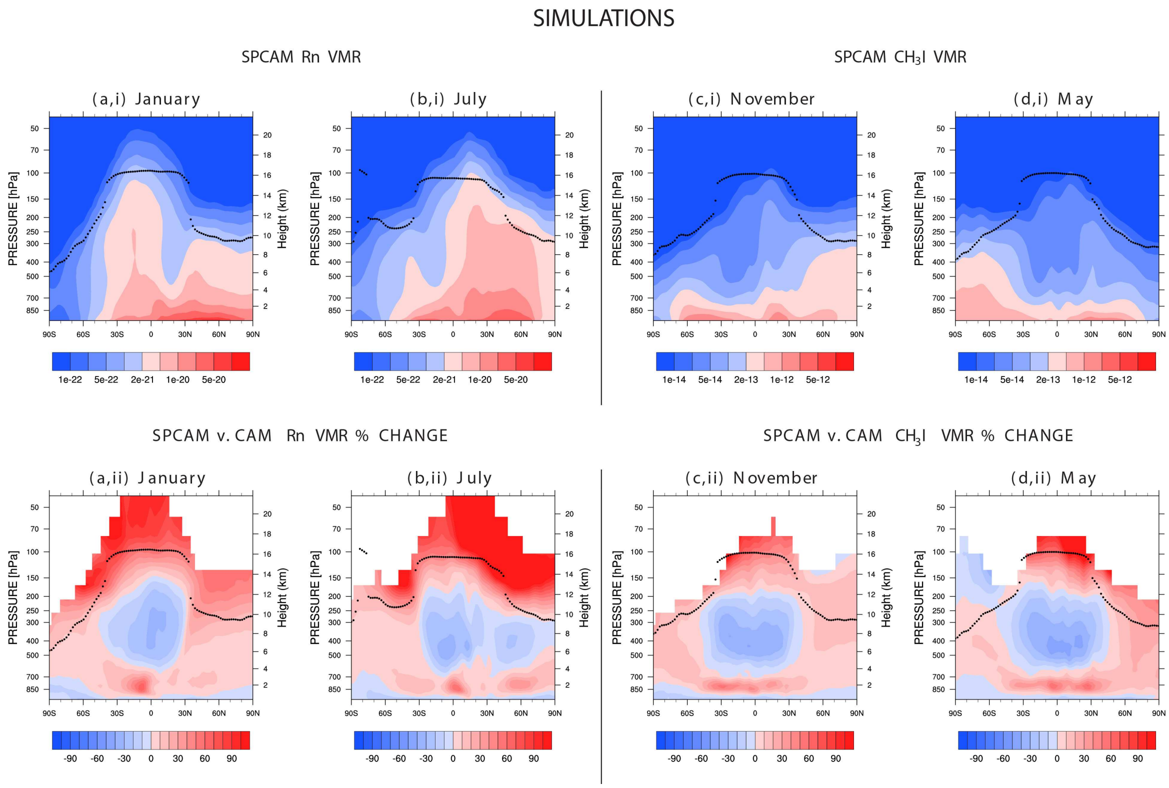

Figure 2.4: Simulated zonal climatologies for Rn for January (a) and July (b), and for CH_3I for November (c), and May (d). The total VMR is plotted on a logarithmic color scheme for the top panels (i) and SPCAM versus CAM percentage differences for the bottom ones (ii). We blank out the areas in which the VMR is three orders of magnitude below the global average between ground and 500 mb. The tropopause line is marked in black.

depletion of the PBL, enrichment of the LT, depletion of the MT to UT, and enhancement of the UT to lower stratosphere (LS) (Fig. 2.4). We provide interpretations of the simulated patters using model outputs averaged at the GCM grid level to relate the patterns to the underlying physical processes. The convective mass fluxes look reasonable for both models, but we do not show these fields because the fluxes have different definitions and hence are not directly comparable. For SPCAM, the fluxes are defined at the CRM grid-scale and involve threshold parameters for the vertical velocity and water path, whereas for CAM the fluxes are calculated by the deep and shallow convective parameterizations at the GCM grid-scale.

For the transport of short-lived tracers like the ones implemented here, *Lawrence and Rasch* [2005] have studied the implications of decomposing the deep convective scheme in CAM from its "bulk" implementation into its original "plume" formulation. They find a pattern for the fractional differences in the simulated VMRs that is similar to our results for the MT to UT and UT to LS (Fig. 2.4, ii, and Fig. 2.4 of *Lawrence and Rasch* [2005]). SPCAM is an explicit plume scheme, and we believe that the same arguments they used to described their results are valid for ours. Their hypothesis is that minimally-entraining plumes can carry higher tracer amounts to high altitudes. However, there are some appreciable differences. Our results show a stronger pattern and apply to Rn which, with its lifetime of about 5 days, should reveal a moderate difference between the models. Moreover, we find that the PBL is depleted and the LT is enriched for SPCAM (Fig. 2.4, ii). In a numerical experiment of tracer transport by mesoscale convective systems where a 2D CRM is forced with large-scale conditions derived from the observations, *Lu et al.* [2000] have shown that simulated deep convection can transport PBL air to the upper troposphere and overshoot through the tropopause on short timescales and with minimal dilutions. These processes could be present in our experiment and could be contributing to the difference in the UT to LS and, in addition, could explain the differences in the PBL tracer VMRs between SPCAM and CAM. In other words, by vertically advecting near-surface air, rich in tracer amount, directly to the UT, SPCAM could be making the PBL more depleted with respect to CAM, which convective mass flux starts higher, at the cloud-base. The last consideration could provide a possible explanation for the enriched LT for SPCAM. Because CAM's convective mass fluxes originate at the cloud base, which falls on average in the LT, it could more efficiently deplete the concentration at that level.

In Fig. 2.5, we show global distributions of the tracer VMRs and relative VMR differences between SPCAM and CAM for an atmospheric layer in the LT between 1.5 and 2.5 Km and one in the UT between 10 and 12 Km.

In general, SPCAM is depleted over dry regions and enriched over wet ones relative to CAM in the LT. For example, SPCAM is depleted in Rn over dry areas such as south-western U.S.A., northern Africa, and south-western Asia during July (Fig. 2.5, a, ii). SPCAM is enriched over very wet areas in the tropical and sub-tropical bands such as south-eastern U.S.A., central and northern south America, central Africa, and Indonesia, during July and November (Fig. 2.5, a, ii). In the UT over the dry regions, SPCAM is enriched (Fig. 2.5,c and d, ii). Also, over some wet regions, such as central Africa, the Amazon Forest, and portion of Indonesia, SPCAM is relatively enriched (Fig. 2.5, c and d, ii). Everywhere else, SPCAM is depleted and enriched relative to CAM just below and above the tropopause, respectively (Fig. 2.4, b and c, ii). We hypothesize that SPCAM is enriched in the LT because it could have stronger mixing in the PBL and because its convective mass fluxes are not concentrated at the cloud base in distinction to CAM. We also infer that SPCAM is depleted in the MT to UT because nearly non-entraining convective plumes could reach higher altitudes without mixing. For the dry regions, the GCM sub-grid vertical transport in CAM is due to the non-local PBL scheme and the shallow convection parameterization that can provide some non-local transport between non-adjacent vertical levels. However, in principle, the CRM in SPCAM could develop a more efficient vertical transport by generating dry thermals able to transport near-surface air directly to higher altitudes.

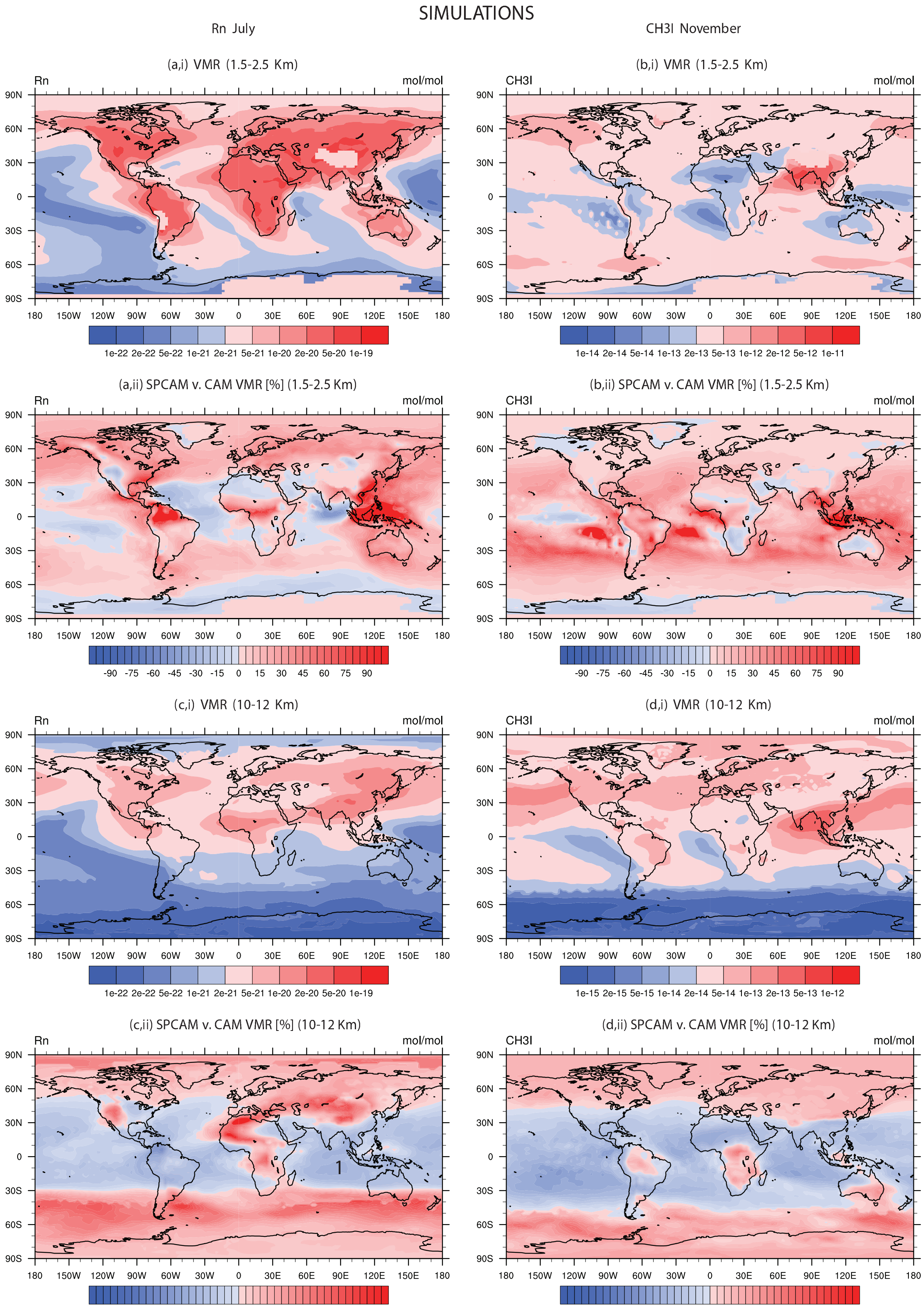

Figure 2.5: Simulated global climatologies for Rn for July (a, b) and for CH_3I for November (c, d), vertically averaged from 1.5 to 2.5 (a, b) and from 10 to 12 Km of altitude (c, d). The total VMR is plotted on a logarithmic color scheme in panels i and SPCAM versus CAM percentage differences in panels ii.

2.4 Summary

We have tested the effects of an explicit treatment for atmospheric convective processes on the fidelity of global simulations of two short-lived passive chemical tracers by comparing simulated profiles against an extensive array of aircraft observations. Contrary to the conventional highly parametric treatment in CAM and all other conventional GCMs, SPCAM introduces a CRM within each GCM grid box to simulate the physical and dynamical atmospheric processes at scales comparable to those of individual cloud systems. We operate CAM and SPCAM in chemical transport mode in order to isolate and differentiate the effects due only to the parameterized and explicit treatments of sub-grid vertical convective motion.

Comparing modeled results with observations for CH_3I, we find that the maximum differences between CAM and SPCAM are generally much smaller than the maximum biases between models and observations. The differences between models typically range from a few percent to tens of percent, while the differences between models and aircraft data range from one to two orders of magnitude. We have quantified modeled biases in simulating the relative changes of the observed tracer VMRs with height (the Local Convective Index, or LCI) for several atmospheric layers.

In general, despite the large statistical uncertainties, SPCAM generates smaller LCI biases for the PBLL, MTL, and UTL, but larger for the LTL. With respect to observations, both models simulate larger vertical gradients in concentrations of CH_3I . These enhanced gradients could arise from a weaker vertical transport, stronger horizontal tracer divergence, stronger photochemical sinks, or a combination of all of these mechanisms, but further analysis is necessary to isolate the causes.

For the majority of the CH_3I case studies, it is possible to contrast climatological and precise comparisons. The first is obtained using multiple simulated years and the latter is obtained using the meteorological reanalysis of the period matching the time the observations were collected. In general, for both models, precise comparisons do not appear to be definitively better or worse than climatological comparisons. This could be because the vertical transport by convective processes is not very sensitive to the meteorological variability or because of biases in the meteorological reanalysis product we used.

Contrasting only results from simulations, we find a quadrupole pattern for the differences between SPCAM and CAM. In the tropics and subtropics where most of the convective precipitation occurs, SPCAM depletes the PBL, enriches the LT, depletes the MT up to approximately 2 Km below the tropopause, and enriches the UT and above relative to CAM. The CRMs embedded in SPCAM allow air parcels to be advected vertically from the surface to any altitude in the model grids. This could result in a greater net vertical transport of tracer-enriched air from less diluted air parcels with respect to a treatment that does not explicitly resolve the physics of convection.

From contrasting models with observations, we have found some indications that SPCAM can simulate the transport of short-lived surface-emitted passive tracers more realistically than CAM. Comparing the simulated tracer distributions of CAM and SPCAM could help design field campaigns for areas where the differences between the models are the greatest.

This would help diagnose which model is generally closer to reality.

Our results, although preliminary and requiring further validation, invite speculation about their implications for atmospheric chemistry and climate. The explicit and the conventional treatment of cloud processes from SPCAM and CAM produce considerable percentage differences in the short-lived compounds evaluated in this study. Our results suggest that SPCAM vertical transport could produce different estimates of the radiative forcing from ozone and its precursors, or from reflecting aerosols as a function of their vertical location with respect to clouds. It could also imply novel dynamical interactions between clouds and their dissipating or promoting compounds. With respect to air quality, the explicit cloud treatment result in a PBL with lower concentrations of compounds emitted by the surface and more efficient high-level long-range transport of these compounds by mid-latitude jets. These implications will be examined in future studies with the Multi-scale Modeling Framework.

Name	**Tracer**	**Pts**	**Period**	**Lat×Lon [°N×°E]**	**Alt. [Km]**	**Mission**	**Reference**	**Figure**
199609_ITCZ_PMT	CH_3I	533	(1996-08-21, 1996-10-05)	(0,20)× (187,227)	(0,10)	PEM-Tropics A	[42]	(1,i)
199609_SPCZ_PMT	CH_3I	2242	(1996-08-31, 1996-10-05)	(-35,0)× (152,260)	(0,11)	PEM-Tropics A	[42]	(1,ii)
199904_TPC_PMB	CH_3I	1612	(1999-03-06, 1999-04-13)	(-34,20)× (194,225)	(0,12)	PEM-Tropics B	[98]	(1,iii)
199909_UTGM_ACC	CH_3I	135	(1999-09-03, 1999-09-20)	(25,39)× (262,281)	(10,19)	ACCENT	[91]	(1,iv)
200103_SCPC_TRP	CH_3I	1383	(2001-02-26, 2001-04-09)	(16,41)× (160,238)	(0,12)	TRACE-P	[52]	(1,v)
200103_SWPC_TRP	CH_3I	3721	(2001-02-27, 2001-04-03)	(7,46)× (112,160)	(0,12)	TRACE-P	[52]	(1,vi)
200401_UTPAN_PREAVE	CH_3I	133	(2004-01-16, 2004-02-02)	(-3,38)× (263,279)	(8,19)	Pre-AVE	N/A	(1,vii)
200407_EUS_INTEXA	CH_3I	2654	(2004-07-06, 2004-08-14)	(27,54)× (250,324)	(0,13)	INTEX-A	[115]	(1,viii)
200601_UTPAN_CRAVE	CH_3I	151	(2006-01-17, 2006-02-09)	(-2,11)× (269,283)	(12,19)	CR_AVE	N/A	(1,ix)
200603_GMEX_INTEXB	CH_3I	893	(2006-02-24, 2006-03-22)	(14,35)× (255,274)	(0,12)	INTEX-B	[114]	(2,x)
200604_STEPC_INTEXB	CH_3I	1058	(2006-04-17, 2006-05-15)	(19,50)× (184,235)	(0,12)	INTEX-B	[114]	(2,xi)
200605_GALA_INTEXB	CH_3I	369	(2006-05-01, 2006-05-15)	(50,63)× (190,225)	(0,12)	INTEX-B	[114]	(2,xii)
200806_SFO_ARCTAS	CH_3I	807	(2008-06-18, 2008-07-13)	(32,42)× (232,245)	(0,10)	ARCTAS	[51]	(2,xiii)
200807_CAN_ARCTAS	CH_3I	699	(2008-06-26, 2008-07-13)	(45,60)× (240,278)	(0,12)	ARCTAS	[51]	(2,xiv)
198705_AMAZ_A2B	Rn	54	(1987-04-20, 1987-05-08)	(-4,0)× (299,312)	(0,6)	ABLE-2B	[93]	(3,i)
199407_NEPC_KRITZ	Rn	127	(1994-06-03, 1994-08-16)	(34,41)× (234,246)	(0,13)	N/A	[63]	(3,ii)
ALLY07_NHCON_LIU	Rn	150	(1970-07-01, 1970-08-31)	(34,49)× (32,271)	(0,12)	N/A	[73]	(3,iii)
200605_ALAS	Rn	76	(2006-05-17, 2006-05-25)	(-34,-35)× (149,150)	(0,3)	N/A	[131]	(3,iv)
ALLY01_ALAS	Rn	71	(2007-01-19, 2007-01-25)	(-34,-35)× (149,150)	(0,3)	N/A	[131]	(3,v)
ALLY05_ALAS	Rn	336	(2006-05-17, 2008-05-14)	(-34,-35)× (149,150)	(0,3)	N/A	[131]	(3,vi)

Table 2.1: Case studies code names for Rn and CH_3I observations from field campaigns.

Chapter 3

Global dust simulations in the multiscale modeling framework

As in chapter 2, in this chapter we continue testing the fidelity of simulated atmospheric transport between a multiscale and a conventional climate model because of its importance for climate simulations. Here we compare dust concentrations and deposition fluxes between the models and between models and observations. Atmospheric transport is relevant for precipitation processes which is the subject of next chapter in which we present a comparison between observationally derived and simulated convective precipitation intensity distributions. The relation between transport and precipitation is recalled in chapters 1 and 6.

3.1 Introduction

Mineral dust affects climate directly by scattering an absorbing sunlight and terrestrial infrared radiation. These processes redistribute radiant energy throughout the climate system and alter the radiation budget of the atmosphere. Soil dust can therefore change local environment states and affect atmospheric processes such as energy fluxes, convection and cloud development [87]. The radiative effects caused by dust could also affect atmospheric circulations. A study from Jones, Mahowald, and Luo [54] presented indirect observational evidence that desert dust can modulate the intensity of easterly waves in the Atlantic Ocean. Dust particles can also affect climate indirectly by serving as cloud condensation/ice crystal nuclei [123, 56, 62, 22], thereby changing cloud microphysical properties and causing an acceleration in precipitation [68].

Aerosol, which can be related to dust, has also been shown to suppress precipitation [127, 1, 106, 27, 45, 39, 8, 38]. Moreover, deposition of mineral dust in the ocean or on the ground impacts biogeochemical cycles and thus could be important for modulating the global carbon cycle [11, 4, 85]. In order to make accurate assessments of these direct and indirect effects of mineral dust on the climate system , we need to understand the spatial and temporal distributions of dust. Mineral dust is strongly affected by sub-grid processes in global climate models (GCMs), particularly processes that are highly uncertain such as the vertical transport by convection. There have been many studies showing that differences among treatments of convection have large effects on the simulated vertical distributions of tracers and aerosols [49, 100, 50]. Thus a realistic representation of convective mixing is essential for correct simulations of all chemical species including dust. It is known that processes important for dust generation, transport and deposition occur on scales which are smaller than a GCM grid size. In current GCMs, typical grid resolutions are on the order of tens to hundreds of kilometers. These relative coarse grids cannot resolve the smaller scale cloud and convection processes. To address this scale separation, parameterizations have been developed to represent subgrid processes in climate models. It is a challenging task to parameterize cloud systems and organized convection since the governing processes cover a broad range of scale, from the microscopic scale of drops/ice crystals to synoptic scale of weather systems and planetary scale of organized meteorologic waves [118]. Moreover, assumptions are often made to derive parameterizations, and this generates a large degree of uncertainty in models. As a result, different GCMs yield quite different simulations in significant part due to disparity among and uncertainty from parameterization schemes [97]. The multiscale modeling framework (MMF) has been developed as an alternative to account for sub-grid cloud processes in GCMs [36, 58]. Under the MMF, a cloud-resolving model (CRM) is implemented inside each grid column of the GCM to explicitly compute small-scale processes and clouds in place of the traditional parameterizations of convection and boundary layer processes. For this reason, MMF is also known as superparameterization (SP) [60]. Khairoutdinov, Randall, and Demott [60] have implement ed the MMF in the NCAR Community Atmosphere Model (CAM), the atmospheric component of the NCAR Community Climate System Model (CCSM). The SuperParameterized CAM (SPCAM) has been used to study various atmospheric processes and has shown some encouraging improvements in reproducing interannual and the subseasonal variability relative to CAM, especially with respect to the Madden-Julian oscillation and equatorially trapped waves [57]. The explicit calculation of sub-grid scale processes in SPCAM includes the convective and turbulent transport of dust and other chemical species at cloud-system scale. SPCAM therefore provides a more physically realistic framework for studying the evolution of aerosols in the climate system. In this work, both CAM and SPCAM are used to characterize the sources, sinks, and distributions of dust with a focus on the different treatment of convection schemes. Following the treatment of water vapor in the SPCAM, we implement dust in the CRM that forms the basis of the MMF in SPCAM. Both models are configured in the chemical transport mode in which offline NCEP reanalysis data is used to supply the meteorological fields. This ensures that the large-scale meteorological states are nearly identical between the two models, and helps us isolate the differences in vertical transport due to the differing convection schemes without the confounding interactions of convection with the large-scale circulation. The analysis and discussion of the dust simulations is organized as follows. Section 3.2 provides an overview of the CAM and SPCAM models and the strategy for coupling cloud-resolving and large-scale dynamical fields via the MMF. Section 3.2 describes the parameterizations for mobilization and for wet and dry deposition of dust in CAM. The design of the experiments is given in section 3.3. The comparison with observations is presented in section 3.4, followed by results and discussions in section 3.5 and conclusions in section 3.6.

3.2 Model description

The SPCAM has been developed by Khairoutdinov, Randall, and Demott [60], and the version of SPCAM we have used is based on version 3.5.11 of CAM that serves as the host GCM for the MMF. The general formulation and simulation results of CAM version 3 (CAM3) are documented in Collins et al. [16]. The spatial grids in both models are configured to a horizontal resolution of 1.9° X 2.5° and a vertical discretization with 28 layers. The finite volume dynamical core is used for all simulations with a dynamical time step of 900 seconds. In our simulations, the MMF component of SPCAM is a 2D CRM configured using an east-west orientation with 26 levels collocated with the CAM vertical layers. There are 32 columns for the CRM domain introduced in each grid cell of CAM, and the eastern-most and western-most columns in each grid cell are connected via periodic boundary conditions. The width of the CRM columns is 4 km, and the time step for the CRM is 20 seconds. The CRM solves the nonhydrostatic dynamical equations simplified with the anelastic approximation and employs a finite-difference method to represent the prognostic equations in flux form. The model applies a second-order central-difference method to compute the advection of momentum subject to conservation of kinetic energy. A positively defined monotone algorithm is employed for advection of all prognostic scalars, including the liquid water/ice moist static energy, total nonprecipitating water (comprised of water vapor, cloud water, and cloud ice) and total precipitating water (which includes rain, snow, and graupel). The CRM uses bulk microphysics to calculate conversion rates and terminal velocities of hydrometeors. Depending on the partitioning between liquid and ice phases, the mixing ratios of cloud water, ice, rain, snow and graupel are diagnosed as functions of temperature. More details of the CRM are given in Khairoutdinov and Randall [59].

Coupling between CAM and CRM

The coupling of dust and other tracers between the outer grid in CAM and the internal domains in each CRM follows the method used to couple water vapor in SPCAM [60]. Two-way interactions between CAM and each embedded CRM are included, and coupling is computed in each CAM time step. The dust in each CRM is first initialized based upon the initial large-scale concentration fields obtained from CAM. The CRM is called in each time step of CAM and is integrated forward by multiple time steps, in effect acting as a type of sub-cycled parameterization. During the n^{th} time step of CAM, a large scale tendency is applied to the CRM prognostic tracers denoted by ψ at each time step of CRM. In order to conserve tracer mass, this tendency ensures that the mean tracer values $\bar{\psi}$ averaged over each CRM domain are consistent with the corresponding and collocated grid box mean values ψ_{LS} calculated by CAM resulting from all the large-scale processes. The large scale tendency has the form:

$$\left[\frac{\partial \psi}{\partial t}\right]_{LS} = \frac{\psi_{LS} - \bar{\psi}^n}{\Delta t_{LS}} \tag{3.1}$$

where $\bar{\psi}^n$ is the horizontally averaged CRM variable at timestep n and Δt_{LS} denotes the CAM time step. Basically the tendency on the righthand side of Equation (3.1) acts as a nudging term such that horizonal mean fields in each CRM follow the evolution of the large scale fields in CAM.

After each CRM completes its integration, the changes due to subgrid scale processes in the CRMs are calculated and returned to CAM [60]:

$$\left[\frac{\partial \psi}{\partial t}\right]_{CRM} = \frac{\bar{\psi}^{n+1} - \psi_{LS}}{\Delta t_{LS}} \tag{3.2}$$

where $\bar{\psi}^{n+1}$ denotes horizontal mean of the CRM fields at the end of timestep $n+1$ of the CRM integrations. Throughout the simulation, the feedback of the CRMs to CAM is continuously calculated based on Equation (3.2). In its original configuration, the CRM computes horizonal averaged fields including temperature, water vapor and cloud condensate. This study adds the calculations of dust, which is modeled as four tracers representing the four particle size ranges following the dust parameterization in CAM. More details of the dust component are described in the following section.

Dust description

The dust component in CAM is based upon the mineral Dust Entrainment and Deposition (DEAD) module developed by Zender, Bian, and Newman [139]. The details of dust implementation in CAM can be found in Mahowald et al. [77]. DEAD includes parameterizations for terrestrial and atmospheric processes governing the atmospheric concentrations of dust including mobilization, dry and wet deposition. In the current version of CAM, the size distribution of dust is represented using four size bins. These are denoted by DST01, DST02, DST03,and DST04 and correspond to diameter ranges of 0.1 - 1.0 μm, 1.0 - 2.5 μm, 2.5 - 5.0 μm and 5.0 - 10.0 μm, respectively. DEAD follows the microphysical and micrometeorological approach developed by Marticorena and Bergametti [82] for dust mobilization and predicts the size-resolved saltation mass flux and sandblasted dust emissions. Prior studies utilizing this approach can be found in Shao, Raupach, and Leys [113] and Shao [111]. Simulations based upon these parameterizations are encouraging at the regional scale, even though many input factors for the microphysical schemes may not be sufficiently well known or inadequately represented by spatially uniform values for application in a global model [112, 83]. The treatment of mobilization in DEAD is governed primarily by wind friction speed, vegetation cover, and the surface soil moisture.

The processes in the parameterization of dry deposition include gravitational settling and turbulent mix-out of particles. The dust particles are assumed to fall at their terminal Stokes velocity as given by Seinfeld and Pandis [110]. This is a good approximation for the settling velocities in the range of diameters between 0.1 to 10 μm in the version of DEAD used in this study. The treatment of wet deposition includes the effects of nucleation and subcloud scavenging by precipitation. Nucleation scavenging is represented by a simple formulation based on Rasch et al. [101] with modifications for dust. The modeled removal rate depends on grid cell aerosol mass path, horizonal fraction of the grid cell where scavenging occurs, local rate of conversion of water vapor to droplets, and mass mean, path normalized scavenging coefficients [139]. DEAD extends the method of Rasch et al. [101] for modeling interactions between aerosols and clouds by using different scavenging coefficients for convective and stratiform clouds. Because the main focus this study is to examine the effects of vertical transport scheme in SPCAM on the dust distributions and burden, the calculations of mobilization, wet and dry deposition of dust remain in the outer (CAM) grid scale. However, it is well known that for deep convection processes, resolved updrafts are much larger than resolved downdrafts. Therefore, since our approach of dust implementation does not include dust removal processes in the CRM grid scale, which may cause different dust vertical profiles as the difference of transported mass between two models is not accounted by the removal processes in the CRM grid scale.

Sub-grid scale processes for dust in the SPCAM include the CRM grid scale advection and turbulent fluxes. The diffusion process is represented by 1.5-order closure to prognose the turbulent kinetic energy. All advection processes for prognostic variables are based upon positive-definite monotone transport algorithms.

3.3 Experiment setup

For the current experiments, both CAM and SPCAM are configured and integrated as chemical transport models in which prescribed offline meteorological reanalyses are used to drive the large-scale dynamics and thermodynamics in CAM [99, 15, 79, 75]. Six hourly NCEP reanalysis data is used in both simulations. The fields used for driving simulations include the three-dimensional zonal and meridional wind fields, temperature profiles, surface latent heat fluxes, surface sensible heat fluxes, and the zonal and meridional components of the surface wind shear. Relative to fully interactive simulations, simulations performed in chemical transport mode minimize the differences in the dust fields due to differences in the large-scale dynamical and thermodynamical fields. The runs with chemical transport mode also have the advantage to avoid the differences in the surface fluxes that arise between interactive simulations from CAM and SPCAM. This simplifies our analysis as the changes between simulations as a result of difference in meteorology is eliminated. This module is also an ideal setup for this study as the treatment of sub-grid scale processes in the model is our main focus. All simulations are started at Dec, 1, 2000, and are run for 13 months. Data of daily output is saved and further processed for specific purposes. The monthly average results of year 2001 are used for most of our analysis.

3.4 Comparison with measurements

The dust module used in this study is the same with the implementation presented in Mahowald et al. [77], which showed the comparison between the model and observations is within reasonable ranges and is similar qualitatively to previous studies. The *in situ* dust observations collected by the University of Miami comprise a long-term data set for assessing the fidelity of the simulated surface dust concentrations (Joe Prospero, private communication). The station observations have been used to evaluate simulations of global dust in previous studies [121, 78, 75, 69, 137]. Figure 3.1 shows a comparison of simulated monthly mean dust concentrations against measurements from the sites at Barbados, Miami, and Iceland. The observations are daily averages for the year 2001.

Compared to measurements, CAM and SPCAM underestimate the dust concentrations for most of the year at these sites. For the Barbados and Miami sites, the concentrations in SPCAM are lower than the concentrations from CAM during most months with the exception of November (Miami) and December (Barbados and Miami). On average, CAM predicts higher dust concentrations than SPCAM by factors of $\sim$1.7 at Barbados and $\sim$1.6 at Miami. As the figure shows, CAM predicts less dust than observed, and therefore the disparity between the simulated dust concentrations and measurements is even larger for SPCAM than CAM at these sites. It is important to note that the emissions in CAM have been adjusted to agreement against observations in interactive mode rather than chemical-transport mode. The fact that SPCAM underpredicts concentrations relative to the measurements at these sites may therefore be due to systematic errors in the emissions, or to errors in the physics or transport in CAM compensated by the adjustment process, rather than a deficiency in the vertical transport predicted by SPCAM. For the site in Iceland, concentrations in SPCAM are larger than those in CAM by a factor of $\sim$1.8 during all months simulated in 2001 although the absolute differences are relatively small compared to the Miami and Barbados time series.

The comparison of dust concentration shows MMF does not always give better agreement with observations. For the Iceland site, the dust concentration predicted in MMF is closer to the observation for all 12 monthly averaged data. For the Miami site, 4 out of 11 months, MMF agrees better with observation than CAM. However, for the Barbados site, the errors from CAM are less than MMF for all 12 month data.

The deposition fluxes obtained from simulations and measurements are compared in Figure 3.2. The details of the measurements and collocated simulation values are given in Table 3.1. The observations are obtained from the compilation of data from 16 sites by Ginoux et al. [34]. Only measurements from eleven of the sites that report deposition fluxes in Ginoux et al. [34] are included in our analysis [139]. As the figure shows, the range of simulated and observed deposition fluxes can span up to four orders of magnitude. The comparison shows that the deposition fluxes are underestimated in the CAM and SPCAM simulations at 8 out 11 sites but that the GOCART model predicts lower deposition fluxes than measured at only 3 out of 11 sites [34]. The overestimation of the deposition at the French Alps, Taklimakan, and Tel Aviv is consistent with the study of Zender, Bian, and

Table 3.1: Yearly mean total dust deposition at 11 sites. Units are in g m^{-1} yr^{-1}. Observed data is obtained from Ginoux et al. [34]

Site	Location	Latitude	Longitude	Observation	SPCAM	CAM
1	French Alps	45.5 N	6.5 E	2.1	1.84	4.14
2	Spain	41.8 N	2.3 E	5.3 ± 2.6	1.06	2.88
3	Midway	28.2 N	177.35 W	0.6 (0.3-1.2)	0.85	1.11
4	Miami	25.75 N	80.25 W	1.62	0.5	0.7
5	Oahu	21.3 N	157.6 W	0.42 (0.4-0.5)	0.27	0.41
6	Enewetak	11.3 N	162.3 E	0.44	0.35	0.19
7	Fanning	3.9 N	159.3 W	0.09 (0.05-0.22)	0.04	0.02
8	Samoa	14.25 S	170.6 W	0.15 (0.02-0.22)	0.02	0.01
9	New Zealand	34.5 S	172.75 E	0.14 (0.1-1)	0.01	0.006
10	Taklimakan	40 N	85 E	450 (110-1900)	189.5	228.8
11	Tel Aviv	32 N	34.5 E	30 (20-40)	0.85	1.7

Newman [139] who also found that MATCH (a chemical transport based on earlier versions of CAM) predicts higher deposition fluxes at these sites. At Miami site, the prediction of deposition flux among simulations as compared to the measured value shows a mixed pattern. A good agreement is seen in DEAD MATCH simulation, an overestimation is observed in GOCART, and an underestimation in our study is found for both SPCAM and CAM simulations. For two South Hemisphere sites (Samoa and New Zealand), lower deposition fluxes are predicted in DEAD MATCH, CAM and SPCAM but higher fluxes are predicted in GOCART. The comparison of deposition fluxes shows 6 out of 11 sites, MMF prediction is closer to the observation than CAM. This includes French Alps, Midway, Enewetak, Fanning, Samoa, and New Zealand. We also compute the normalized root mean square (NRMS) error and mean normalized bias (MNB) introduced in Huneeus et al. [46] for deposition flux. The calculated MNB for SPCAM is -0.51, and -0.35 for CAM. The NRMS error of SPCAM is smaller than CAM, being 0.42 versus 0.54, respectively.

The comparison of wet fraction between models and observations is summarized in Table 3.2. Similar to previous studies, the model overestimate the importance of wet deposition. As compared to the observations, the predicted wet deposition fraction in all sites (except the one in Coastal Antarctica predicted by SPCAM) is higher. In stations of Amsterdam Island and Cape Ferrat, the overestimation exceeds 100%. Among these 11 stations, SPCAM predicts a closer wet deposition fraction to the observed data in seven stations including Amsterdam Island, Cape Ferrat, Samoa, New Zealand, North Pacific, Greenland, and Fanning.

3.5 Results and discussions

In this section, we compare and analyze the dust patterns in SPCAM and CAM simulations. Multiple features in spatial distributions, vertical profiles and monthly mean dust mixing

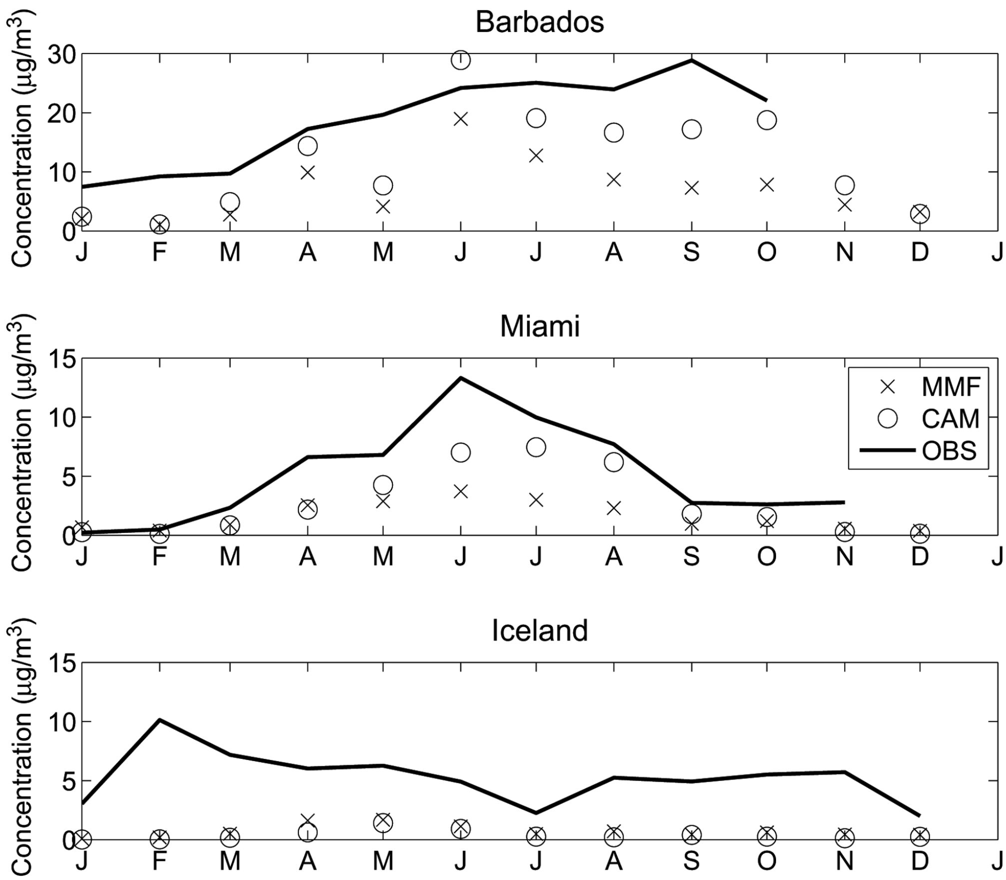

Figure 3.1: Comparison of monthly mean dust concentration for Barbados, Miami and Iceland.

Table 3.2: Wet deposition fraction (%). Observed data is obtained from Huneeus et al. [46], Mahowald et al. [80]

Station	Observation	SPCAM	CAM
Bermuda	17-70	87	80
Amsterdam Island	35-53	91	93
Cape Ferrat, Mediterranean	35	84	88
Enewetak Atoll	83	94	94
Samoa	83	95	97
New Zealand	53	91	95
North Pacific	75-85	85	86
Greenland	65-80	84	88
Coastal Antarctica	90	87	91
Midway	75-85	79	73
Fanning	75-85	94	96

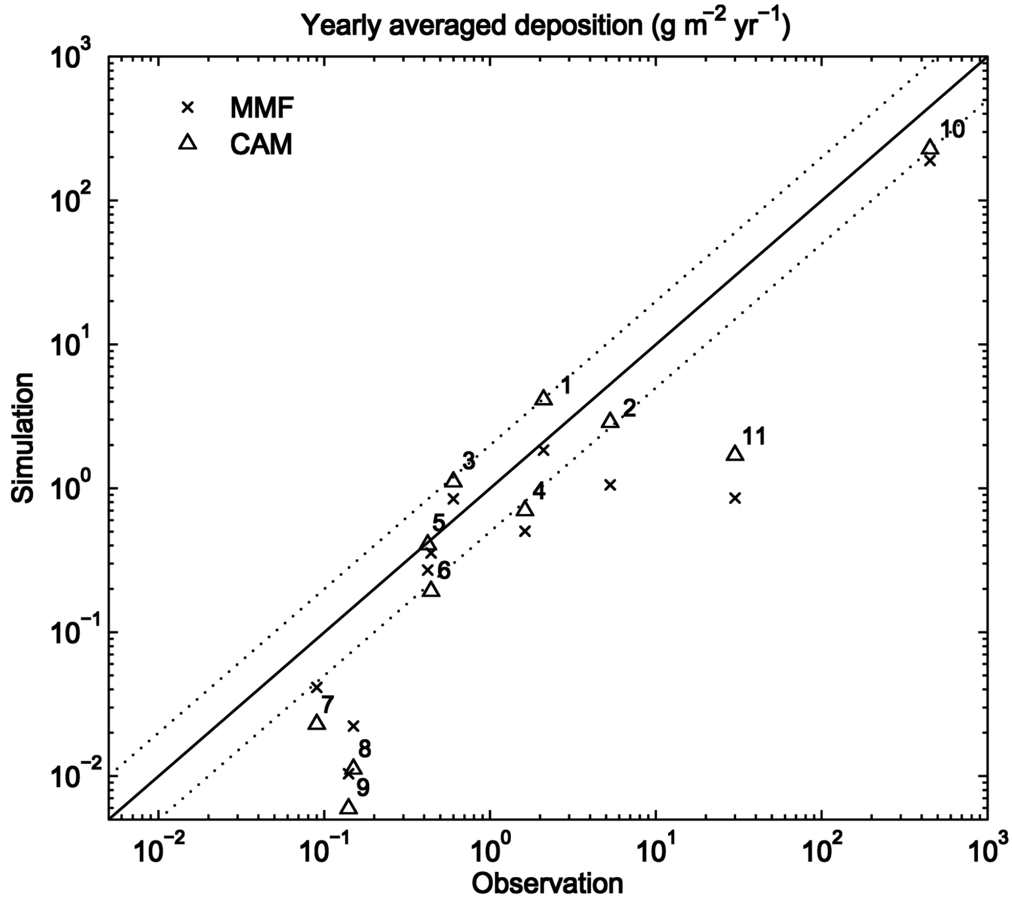

Figure 3.2: Comparison of total dust deposition between the yearly mean simulation and climatology observations. Observed data is obtained from Ginoux et al. [34]. Values are given in Table 3.1

ratio are discussed in order to relate the changes to differences in sub-grid vertical transport. Comparison of mobilization fluxes, wet and dry deposition rates, dust burdens and dust lifetimes are also analyzed. All figures depict averages for the year 2001 otherwise indicated.

Distribution of dust

The global distribution of dust predicted by CAM is shown in Figure 3.3 for four vertical layers including 994 mb (the lowest model layer), 915 mb, 750 mb, and 501 mb. The dust mixing ratio plotted is the sum of DST01 through DST04. The layers above 501 mb are not shown because dust concentrations are relatively low in the upper troposphere (See Figure 3.4 for vertical profile of dust). Only plots from CAM are shown because the spatial distributions of dust are visually similar for the two models. Dust concentrations are higher around source regions, in particular the Sahara and Gobi deserts from the lowest model layer through the lower troposphere up to 750 mb. In the vertical profile of zonal mean dust shown in Figure 3.4, the highest concentration is near 40°N where the emission is. The effects of long-range transport are evident in the figure from the elevated concentrations of dust in the lower atmosphere downwind of the primary emission regions. The relatively high values of dust mixing ratio in north America can be seen from the surface layer up to approximately 964 mb, the portion of the atmospheric column in which boundary layer parameterizations strongly affect the transport of dust.

The corresponding percentage differences in dust concentrations between SPCAM and CAM are shown in Figure 3.5. The difference plot shows that in the lowest layer, dust concentrations are higher in the SPCAM in areas neighboring source regions but lower in mid-latitudes between 20°N to 50°N. Most of the mid-latitude regions in the North Hemisphere show reductions in dust at the lowest model levels for SPCAM relative to CAM. In the upper boundary layer and lower free troposphere over Africa, dust decreases in SPCAM compared to CAM between 982 mb and 694 mb. However, in the middle and upper troposphere for pressures at and below 500 mb, SPCAM predicts a higher dust mixing ratio than CAM. In the vertical profile of zonal mean percentage difference shown in 3.4, it is seen as compared to CAM, the largest decreased dust of 30 % predicted by SPCAM is in the middle troposphere around 850 to 700 mb near source areas at 40°N. At 750 mb, horizontal distribution shows negative dust changes cover most of areas in NH which is also seen in the corresponding vertical profile.

Mobilization, dry and wet deposition

The distributions of dust are produced by the combined effects of sources, sinks and atmospheric transport. In this section we examine differences between the SPCAM and CAM due to the sources of dust from wind-generated mobilization and to the sinks associated with wet and dry deposition.

Figure 3.6 shows the mean mobilization flux for CAM, and the percentage difference between the two models. The yearly averaged mobilization flux for SPCAM and CAM is summarized in Table 3.4. As expected, dust sources are mainly located in north Africa (the Sahara) and in central China (Gobi desert) with some relatively lower emissions in the Middle East, west Asia, and north America. In general there are higher mobilization fluxes in SPCAM relative to CAM, and the increase in emissions can be up to 10 % in source regions around southern Mongolia, northern China, and north America. A slight decrease of mobilization is seen in northeast Africa, the southeastern sector of Saudi Arabia, and western Asia. Even though we use identical meteorology reanalysis data in both models, there are still some internal differences due to methodology of subgrid CRM calculation. Thus the two models have different precipitation which leads to difference in soil moisture content, which is an major variable for calculating dust mobilization. Because of soil moisture difference, the mobilization flux on average differs by $< 5\%$ between SPCAM and CAM.

The yearly-mean globally integrated mobilization for SPCAM of 1587 Tg/y is slightly larger than the 1516 Tg/y of dust mobilized in CAM. These estimates are within the range

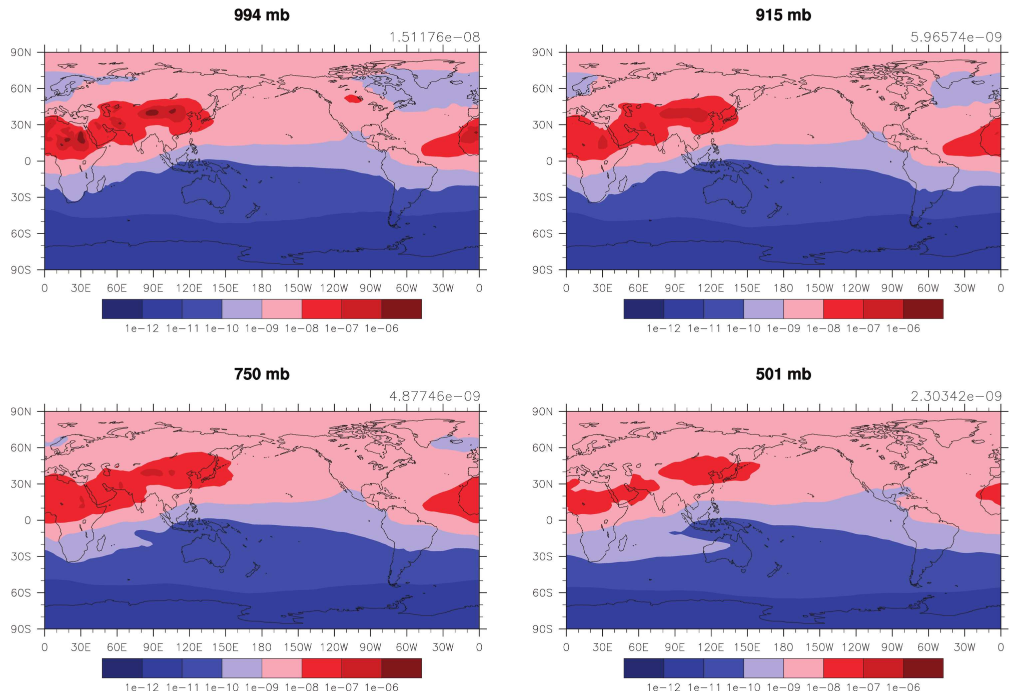

Figure 3.3: Global dust distribution for CAM simulation in four different model layers. Global mean value is shown in the upper right corner in each plot.

of estimates from previous studies, for example 1490 Tg/y for particles smaller than 10 μm [139], 1814 Tg/y for particles less than 12 μm [34], and 1250 Tg/y for particles smaller than 16 μm [120].

The yearly mean dry deposition flux is shown in Figure 3.7. The yearly averaged dry deposition flux for SPCAM and CAM is summarized in Table 3.4. The overall pattern of dry deposition is similar between SPCAM and CAM, but the deposition flux is higher in SPCAM than CAM especially in source regions including northern Africa, the Middle East, western Asia, central Asia, and North America. The amount of dry deposition depends on the removal rate which in turn is determined by the dust concentration and the deposition velocities. The dust removed by dry deposition is linearly proportional to the concentration of dust, and therefore higher rates of mobilization that cause increased dust concentrations in the boundary layer will result in higher rates of dry deposition. The yearly-averaged globally integrated rates of dry deposition for SPCAM and CAM are 1130 Tg/y and 916 Tg/y, respectively (Table 3.4). In these simulations, dry deposition accounts for a large fraction of the total deposition (Table 3.4). The yearly-averaged percentages of total deposition represented by dry deposition are 71% for SPCAM and 60% for CAM.

The yearly averaged wet deposition flux is shown in Figure3.8. Although the globally-integrated wet deposition flux is larger in CAM, SPCAM simulates a higher wet deposition

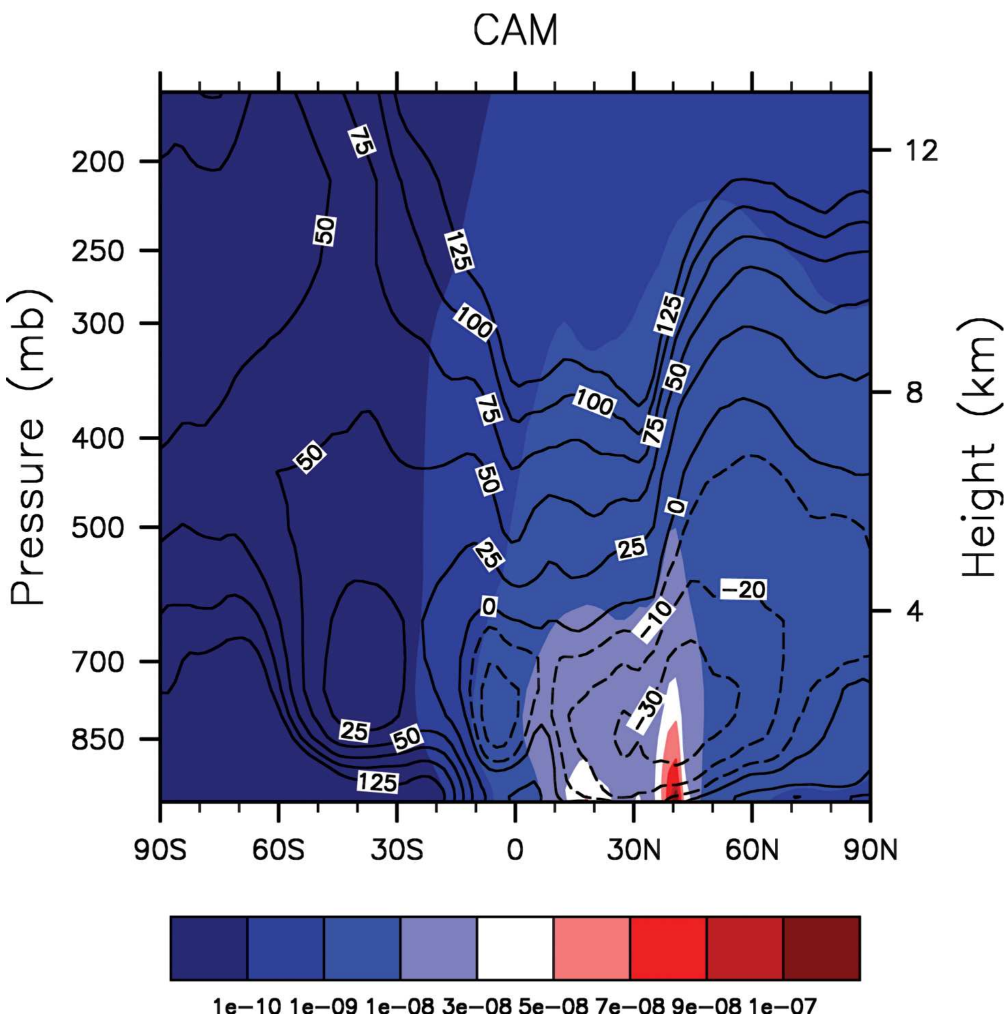

Figure 3.4: Color contours: vertical profile of zonal mean total dust mixing ratio from CAM. The dust field is the sum of DST01 through DST04. Line contours: percentage difference in the unit of %, negative values are shown in dash lines.

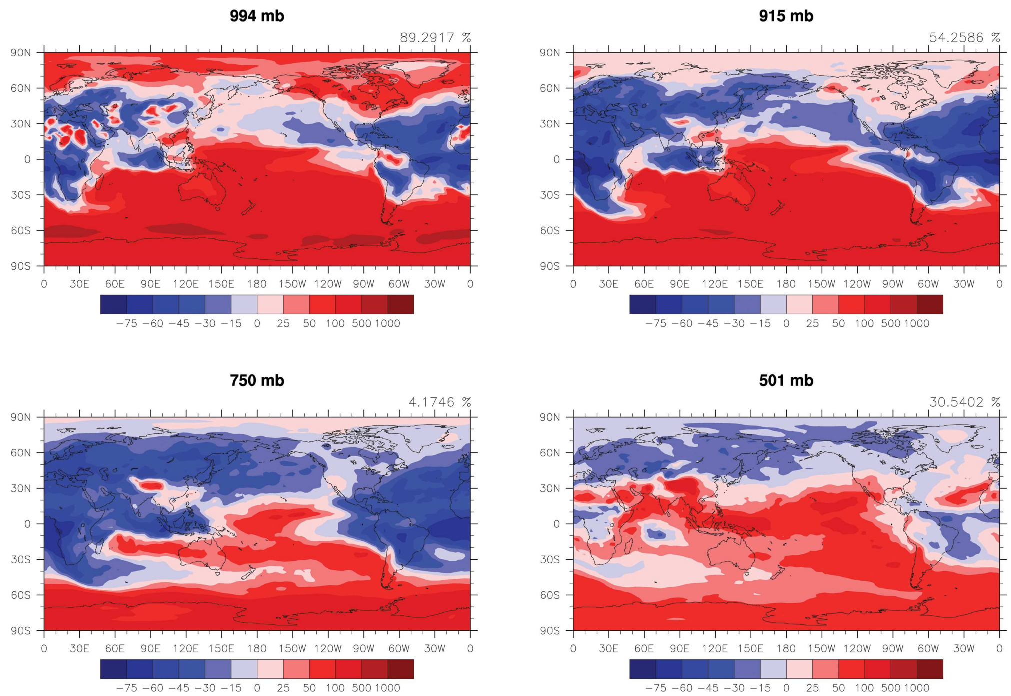

Figure 3.5: Percentage difference of global dust distribution in four different model layers. Percentage difference is calculated as (SPCAM - CAM)/CAM*100. Global mean value is shown in the upper right corner in each plot.

around dust sources including northern Africa, the Middle East, western and central Asia, and most of North America. This difference between the two models follows the same pattern of differences that we find for dry deposition (Figure3.7). Comparing Figure 3.7 with Figure 3.8, the areas which have higher wet deposition in SPCAM are broader than the areas which have higher dry deposition in SPCAM. The yearly-averaged and globally-integration wet deposition fluxes are 460 Tg/y for SPCAM and 603 Tg/y for CAM.

Figure 3.9 shows the averaged precipitation from CAM (upper figure) and the percentage change in precipitation between SPCAM and CAM (lower figure). Compare to the change in wet deposition shown in Figure 3.8, the change in wet deposition does not necessarily show the same trend for the change of precipitation. Part of the reason may be evaporation of rain is included in the wet deposition calculation. It was also pointed out by Mahowald et al. [2011] the precipitation rate plot is less correlated with the fraction of wet deposition than the distribution of fraction of time with precipitation, which showed similar patterns to the wet deposition fraction. We also compute the globally averaged change of wet deposition and precipitation with respect to the mean value from two models. In other words, the percentage change is calculated as difference (SPCAM-CAM) and divide by the mean value based on SPCAM and CAM results. The percentage change for precipitation is $\sim$ -10.3 %

and for wet deposition is ~ 3.8 %.

Vertical profiles of dust

In this section, the size-segregated and total dust concentrations are analyzed to better understand the mass budgets for dust both in each size range and in the aggregate. Recall that the size categories are denoted by DST01, DST02, DST03,and DST04 and correspond to diameter ranges of 0.1 - 1.0 μm, 1.0 - 2.5 μm, 2.5 - 5.0 μm and 5.0 - 10.0 μm, respectively (section 3.2). The zonal mean vertical profiles of mass mixing ratios for each of the size-segregated dust tracers from the CAM simulation and the corresponding percentage differences are shown in Figure 3.10. It can be seen that dust mixing ratios are orders of magnitude higher in Northern Hemisphere and that the largest values are associated with strong emission regions. In general, the mixing ratios increase for larger sizes of dust. In Figure 3.10, the meridional extent of mixing ratios in the range of 10^{-8} to 10^{-7} is the largest for DST04, and the latitudinal range with elevated concentrations extends to higher altitudes for this size category. There are two local maxima in the dust concentrations for both DST03 and DST04 near the surface in latitudes between 15°N and 40°N. The horizontal and vertical extents of the maxima in DST04 are greater in DST04 than those for DST03.

The line contours in Figure 3.10 show the percentage differences between the two simulations calculated as (SPCAM - CAM)/CAM $*100$. Comparison between SPCAM and CAM of the zonally average concentration profiles shows that for the smaller sizes of dust represented by DST01 and DST02, there is an increase in the dust mixing ratio near the surface from 10°N to 90°N. This feature becomes less evident for DST03 and is reversed for DST04, which decreases in SPCAM compared to CAM between the surface through the mid troposphere. Across all the dust size bins, DST04 exhibits the largest area in which concentrations decrease in SPCAM relative to CAM. Comparing SPCAM to CAM from 30°S to 40°N, there is less dust in the mid troposphere and more dust in the upper troposphere for all dust sizes. From the equator to 40°N, the altitudes where the concentrations in SPCAM exceed those in CAM increase slightly with increasing dust sizes.

The vertical profiles of globally integrated dust mass for each dust size bin are shown in Figure 3.11. In the lowest layer, the total mass of dust in SPCAM is larger than that in CAM for DST01, DST02, DST03 but lower for DST04. For all the dust variables, there is less dust mass in the lower and middle troposphere and higher mass in upper troposphere in SPCAM as compared to CAM. This feature, and the dependence of the transition altitude on dust size, are both consistent with the zonal mean profiles shown in Figure 3.10. The pressure below which SPCAM predicts higher mass than CAM decreases with increasing dust size from around 600 mb for DST01 to 400 mb for DST04. Despite the nearly identical mobilization flux dust in the two models, the dust mass in the layers closest to the surface increases with altitude for CAM but decreases in altitude for SPCAM. This dipole pattern suggests that vertical transport of dust within the boundary layer is more efficient in CAM than in SPCAM. The difference between CAM and SPCAM in the total concentration of

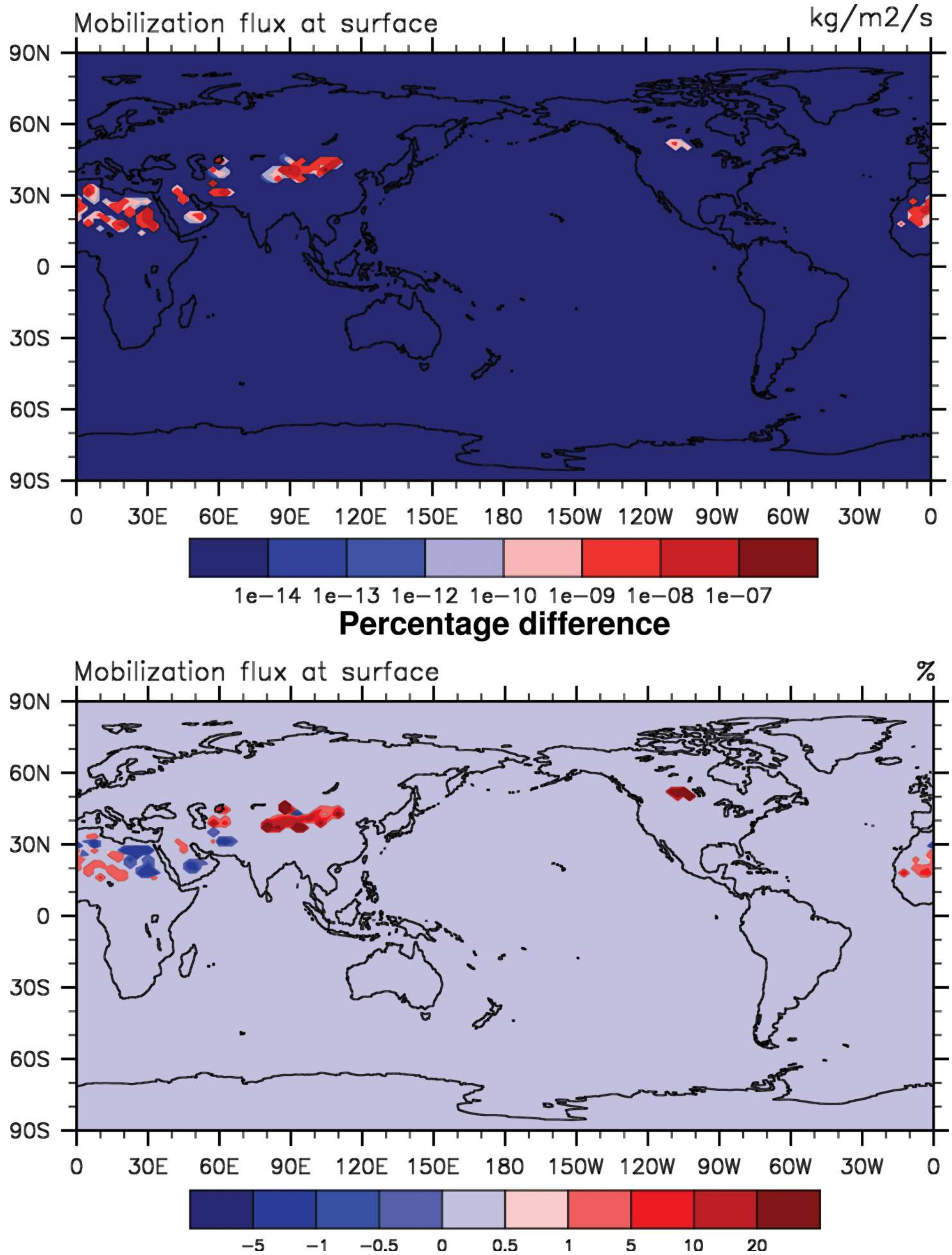

Figure 3.6: Upper plot: Global dust mobilization distribution for CAM simulation. Lower plot: percentage difference of dust mobilization calculated as (SPCAM-CAM)/CAM*100

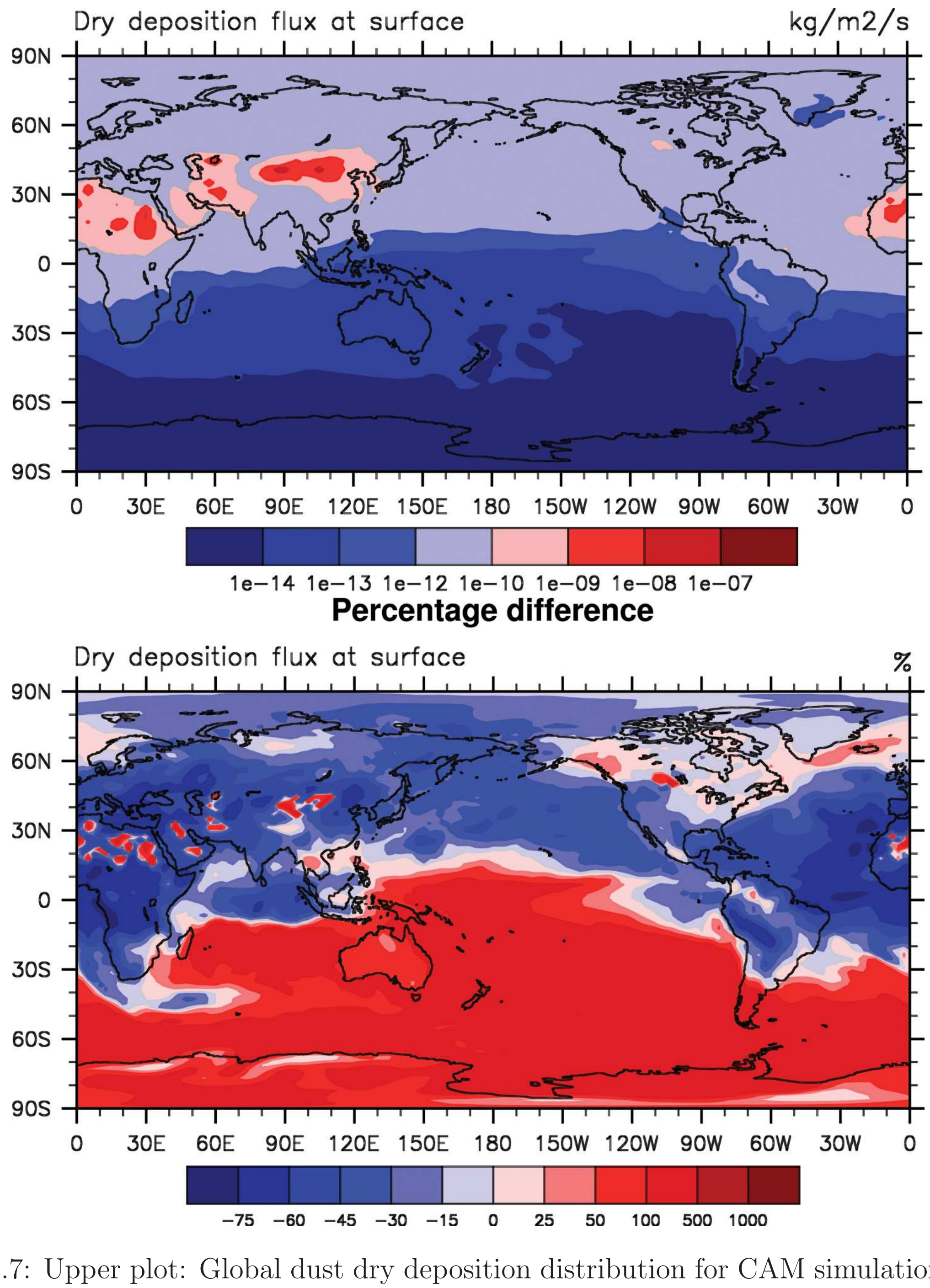

Figure 3.7: Upper plot: Global dust dry deposition distribution for CAM simulation. Lower plot: percentage difference of dry deposition calculated as (SPCAM-CAM)/CAM*100

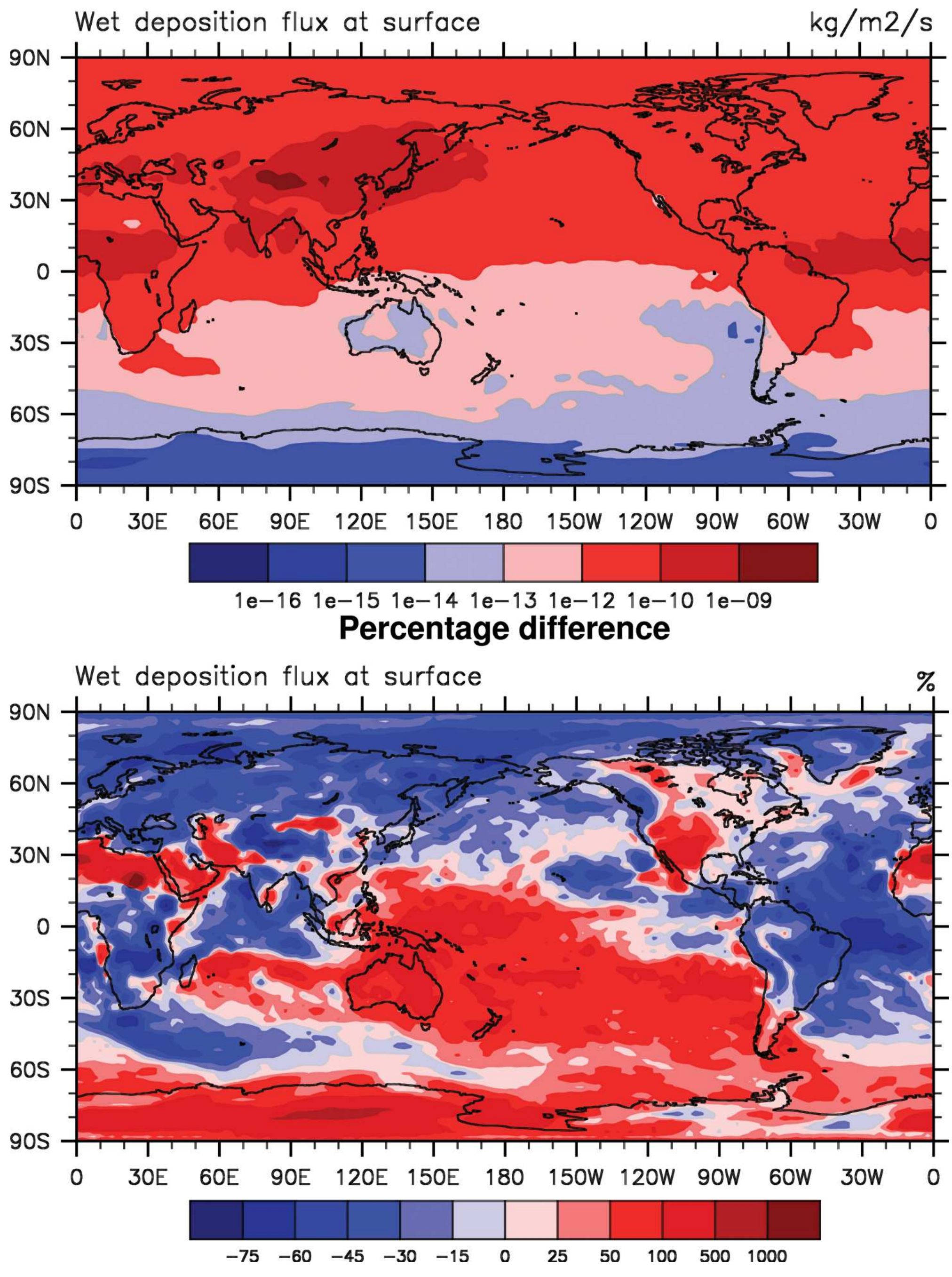

Figure 3.8: Upper plot: Global dust wet deposition distribution for CAM simulation. Lower plot: percentage difference of wet deposition calculated as (SPCAM-CAM)/CAM*100

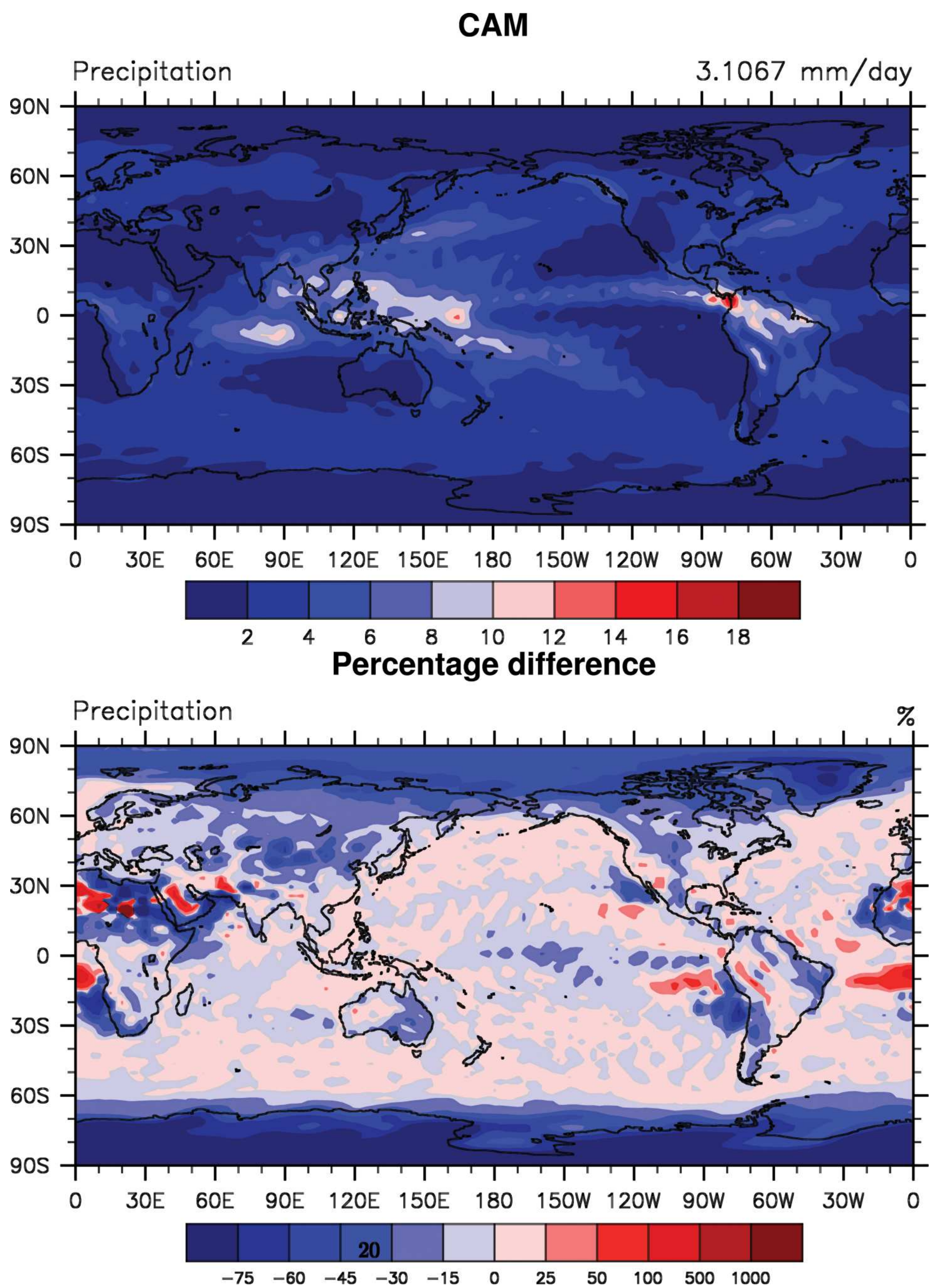

Figure 3.9: Upper plot: Global precipitation distribution for CAM simulation. Lower plot: percentage difference of precipitation calculated as (SPCAM-CAM)/CAM*100

dust, i.e., the sum of DST01 through DST04, can be large as 1 Tg around 750 mb (Figure 3.11).

The larger dust mass in upper troposphere in SPCAM may be related to the dust implementation approach used in this study. Since the removal processes of dust are not calculated in CRM grid scale, the larger resolved updrafts by CRM for deep convection transport more dust aloft. Therefore, higher concentrations in SPCAM at upper layers are simulated. Part of reason for the difference in vertical distribution of dust between two models is due to the different convective transport schemes, which cause changes in dust mass with respect to height. The different vertical distribution of dust will in turn affect dry deposition calculation, which is dominant dust removal process especially for large particles. As a result, the predicted dust burden is different between two models. To sum up, differences in dust distributions will cause changes in dust removal processes. The evolution of dust is a dynamical process, the mass of dust determines the amount of dust being removed, at the same time, the removal amount affects the dust mass.

Figure 3.12 shows the vertical profiles of dust lifetimes calculated based on dry deposition for each size range of dust simulated by SPCAM and CAM. Figure 3.13 is the corresponding lifetimes calculated based on wet deposition. From Figure 3.12, it is evident that the amount of mass removed by dry deposition is very sensitive to the particle size. To estimate the characteristic time scales for the dry deposition process, a calculation of the times required for particles falling at speeds given by the Stokes law to reach the surface is summarized in Table 3.3. Thus, for particles starting at 150 m above the surface, it takes less than 30 minutes (2 time steps) for the largest dust particles to reach the ground. In contrast, the characteristic lifetime for the smallest particles represented by DST01 is approximately 17 days due to the low fall speeds of order 0.01 cm/s.

The vertical profiles in Figure 3.12 show the lowest model layer has shortest dust lifetimes based on dry deposition. SPCAM predicts shorter dust lifetimes than CAM mainly due to larger deposition in SPCAM. The dust lifetime based on dry deposition at the lowest model layer decreases with increase of particle size. For SPCAM DST01, DST02, DST03, and DST04, the value is 17.65, 8.03, 0.94, and 0.1 days, respectively. The corresponding lifetime for CAM DST01, DST02, DST03, DST04 is 26, 17.86, 1.56, 0.21 days, respectively. The largest amount of dry deposition is in the lowest layer in both models, and SPCAM predicts a greater mass of dust removed by dry deposition than CAM. The increase in dry deposition mass from CAM to SPCAM is 50 Tg for DST03 and is as large as 300 Tg for DST04. The large rates of dry deposition for DST03 and DST04 in SPCAM cause the global dust masses represented by these tracers to be much lower in SPCAM than CAM.

The vertical profiles in Figure 3.13 show differences of dust lifetimes based on wet deposition between two models are larger in lower model layers from the surface to around 800 mb. The largest difference can be 10 days for all four size range of size bins. The dust lifetime based on wet deposition at the lowest model layer for SPCAM DST01, DST02, DST03, DST04 is 15.24, 15.54, 19.18, 20.45 days, respectively. The corresponding lifetimes for CAM DST01, DST02, DST03, DST04 is 11.02, 11.11, 14.13, 19.36 days, respectively. For most of layers, CAM shows shorter wet lifetimes than SPCAM because higher wet deposition

Table 3.3: Time for dust particles to fall on the ground from 150 m above the surface. One time step of large scale model is 15 mins.

	DST01	DST02	DST03	DST04
Size range (μ m)	0.1 - 1.0	1.0 - 2.5	2.5 - 5.0	5.0 - 10.0
Deposition velocity (cm/s)	0.01	0.1	4	10
Steps	1667	167	4.2	1.7
Days	17	1.7	0.04	0.02

fluxes are predicted in CAM. Comparing smaller particles such as DST01, DST02 with larger particles of DST03 and DST04, it is seen the wet lifetimes for smaller particles are shorter. Therefore wet deposition is the dominant removal mechanism to remove smaller dust particles such as DST01 and DST02. However, for the larger dust sizes represented by DST03 and DST04, dry deposition is the primary mechanism.

Dust burden

Figure 3.14 shows the comparison of monthly mean burden in the four size-segregated dust tracers. The burdens of DST01 and DST02 in SPCAM are higher than those in CAM for every month except April (DST02 only), May, and June. However, for the larger dust sizes represented by DST03 and DST04, SPCAM predicts lower dust burdens than CAM throughout the annual cycle. The most likely reason for these lower burdens in SPCAM is that SPCAM predicts a significantly higher dry deposition flux for the larger dust particles with the result that a much large amount of dust is removed in SPCAM relative to CAM. The larger dry deposition in SPCAM is because SPCAM transports dust less efficiently than CAM in lower layers, so the dust mass at the lowest model layer is higher which causes larger deposition. The dry deposition rate is calculated as the difference of deposition fluxes between the lowest two model layers. It is known the dry deposition depends largely upon the amount of dust at the lowest model layer, which is affected by the vertical transport scheme. The sum over all sizes bins shows that the mass of dust is lower in SPCAM relative to that in CAM. In our one-year simulation period, the mean dust loadings for SPCAM and CAM are 14.8 Tg and 19.7 Tg, respectively.

In CAM, the dust loading reaches its peak values during May and its lowest values during the Boreal winter months (Figure 3.14) . The monthly mean burden in SPCAM from the sum of all dust bins follows a bimodal annual cycle with the highest dust loadings during May and July (plot is similar to DST03 shown in Figure 3.14). In general, the annual dust cycle in SPCAM follows CAM but with reduced mass due to higher removal rates in SPCAM. Thus the dust peak in May in CAM is also seen in SPCAM. The combined differences from source and sink processes result in a bimodal like dust annual cycle in SPCAM.

A summary of mass fluxes for mobilization and for dry and wet deposition in each dust size category is presented in Table 4. For larger particle sizes, the magnitude of dry deposition is roughly comparable to the magnitude of mobilization. For the smaller particle sizes, wet

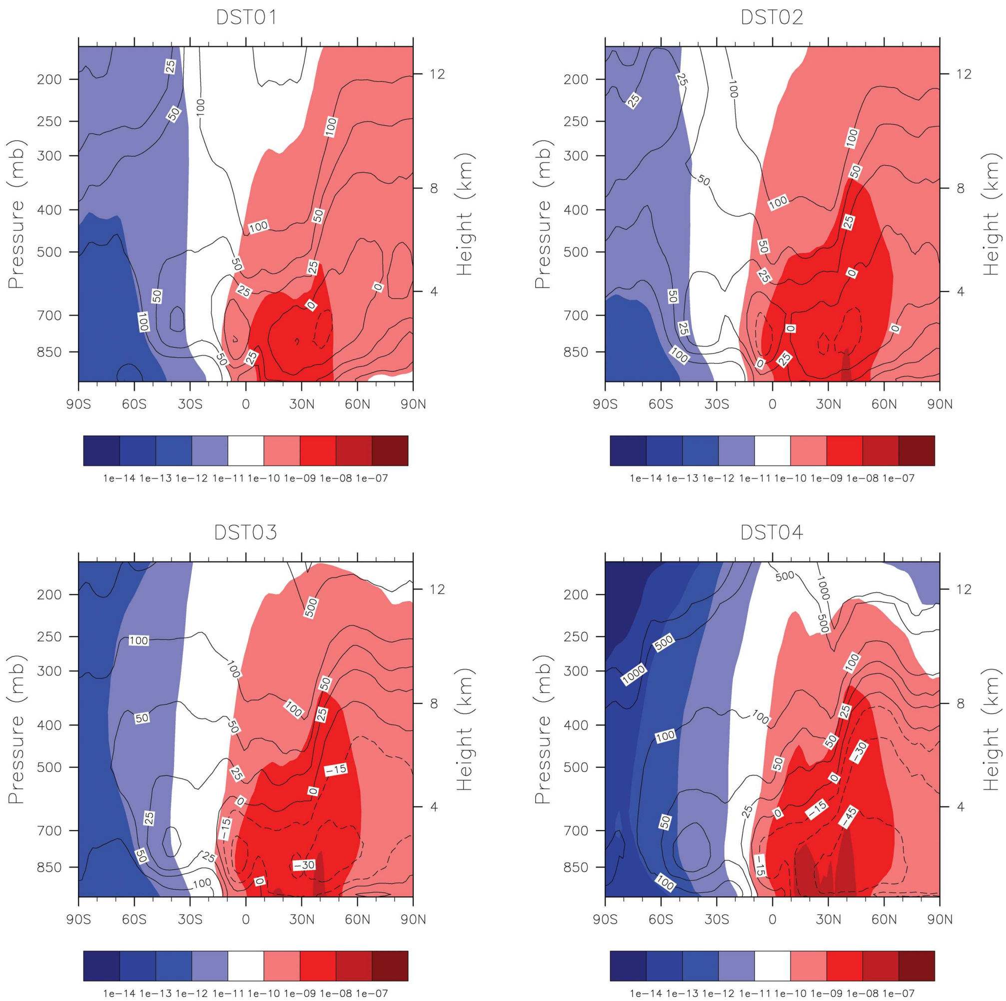

Figure 3.10: Vertical profiles of zonal mean dust mixing ratio for DST01, DST02, DST03 and DST04 shown in colors. The percentage differences are shown in contour lines. Contour level is -45, -30, -15, 0, 25, 50, 100, 500, 1000 %

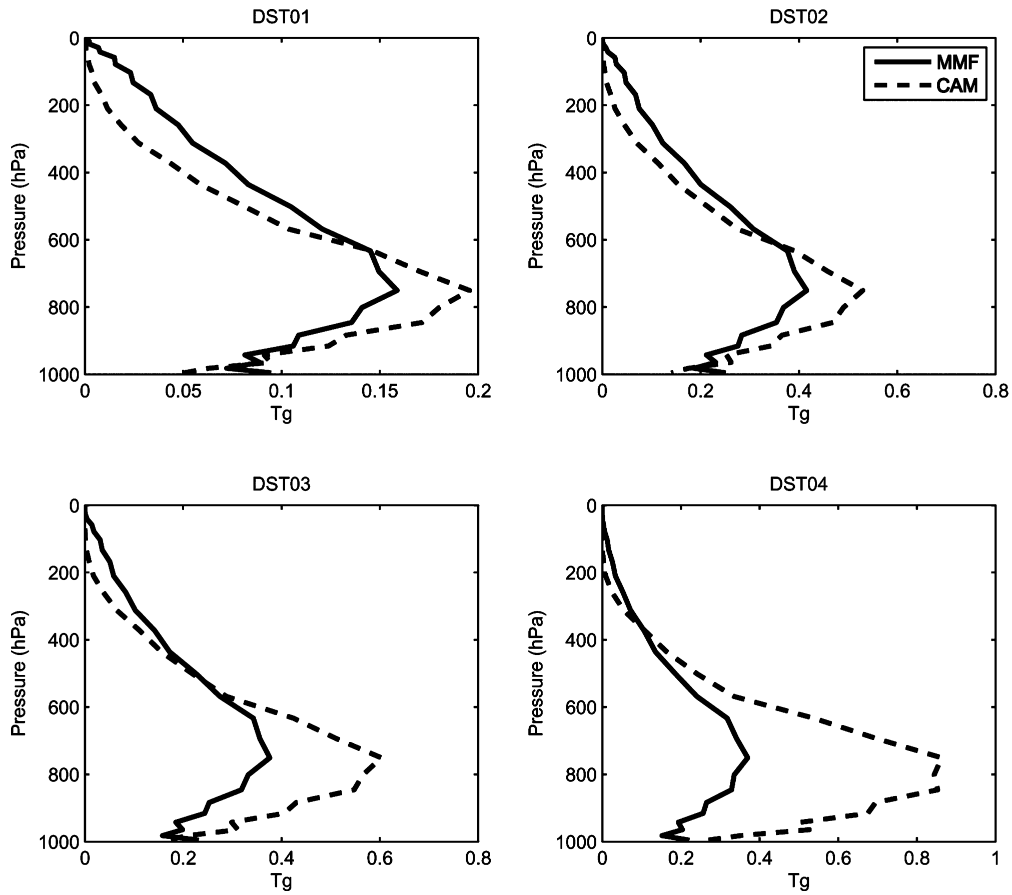

Figure 3.11: Vertical profile of global dust mass for DST01, DST02, DST03 and DST04.

deposition is the dominant mechanism for dust removal. The mobilization rates for individual dust bins are approximately 60 Tg/y (DST01), 175 Tg/y (DST02), 270 Tg/y (DST03), and 1075 Tg/y (DST04). Comparison of the sources and sinks in the table suggests that dust mass increases in SPCAM for small dust particles because of the elevated mobilization fluxes in that model. For large dust particles, the increase of deposition flux in SPCAM is much higher than the increase of mobilization flux and therefore the dust masses in the DST03 and DST04 size categories are much lower in SPCAM.

Time scale and ratio analysis

The characteristic lifetimes of dust are readily estimated by dividing the atmospheric dust burdens by the mass fluxes for the sources and sinks [121, 46, 66]. Figure 3.15 shows the monthly mean lifetime of dust calculated from the ratio of the dust burden to the mobilization, dry and wet deposition fluxes. The lifetimes calculated based on the total removal rates (sum of dry and wet deposition) are also included. The time scale analysis

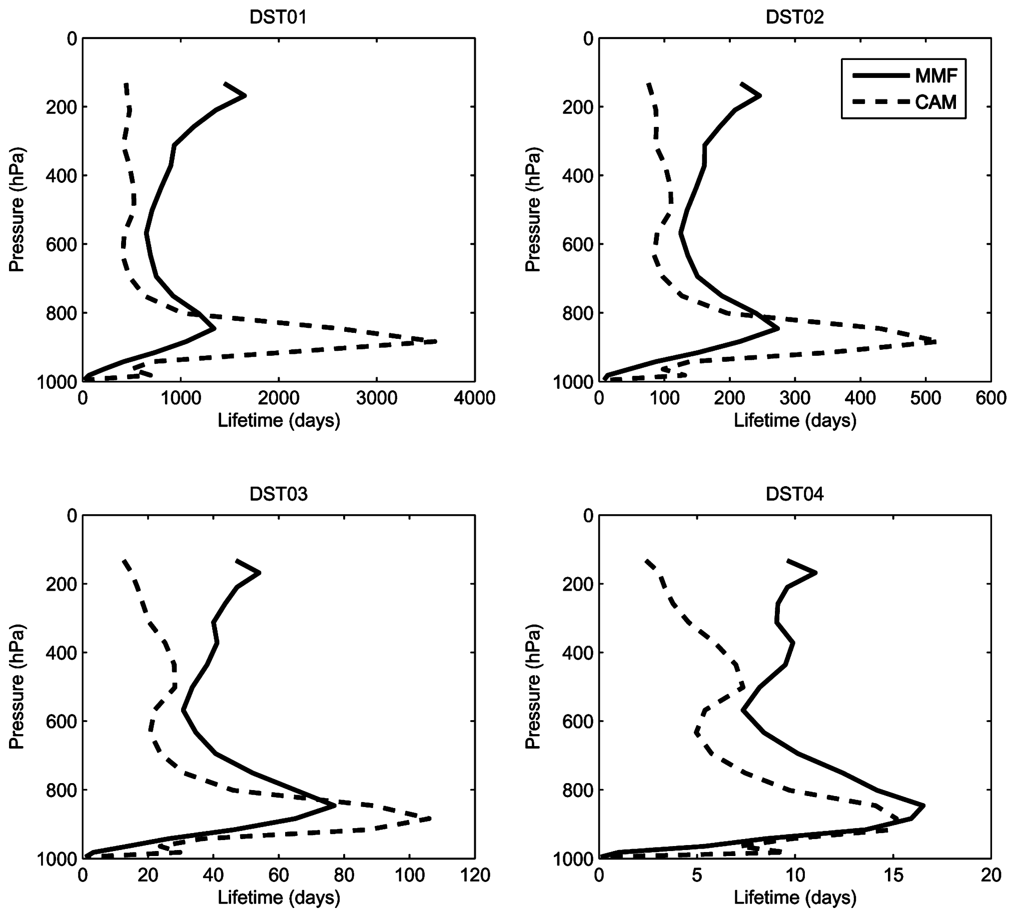

Figure 3.12: Vertical profile of particle lifetime calculated based on dry deposition for DST01, DST02, DST03 and DST04.

Table 3.4: Yearly averaged dry deposition, wet deposition, sum of dry and wet deposition, mobilization flux and the corresponding lifetime in SPCAM and CAM simulations. The unit of flux is in Tg y^{-1}. Lifetime is in days.

	DST01	DST02	DST03	DST04	Lifetime
SPCAM(dry)	3.3	27.9	144.0	954.7	4.78
CAM(dry)	1.7	15.4	95.9	802.8	7.85
SPCAM(wet)	57.8	149.1	129.3	124.1	11.32
CAM(wet)	56.7	153.5	164.9	228.2	11.93
SPCAM(dry+wet)	61.1	177.0	273.2	1078.8	3.36
CAM(dry+wet)	58.3	168.9	260.9	1030.9	4.73
SPCAM(mob)	61.0	176.7	273.0	1076.0	3.41
CAM(mob)	58.3	168.8	260.9	1028.3	4.75

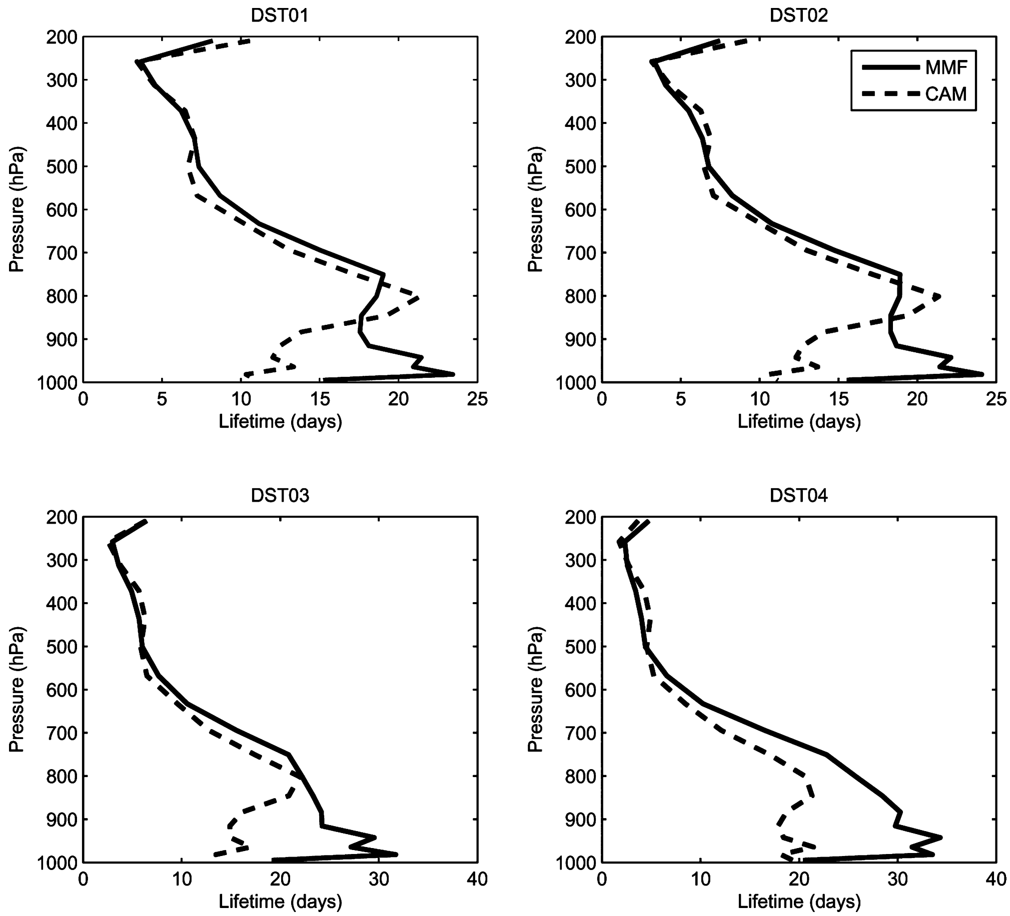

Figure 3.13: Vertical profile of particle lifetime calculated based on wet deposition for DST01, DST02, DST03 and DST04.

provides the information of how long it will take for dust to reach the level of the mean dust burden by mobilization and the days to completely remove dust by either dry, wet deposition or both. The rate at which dust is replenished by mobilization in SPCAM is faster than the corresponding rate in CAM since the time scale in SPCAM is shorter than that in CAM for all months. This is also observed for the dry deposition process for which lifetimes in SPCAM range from 2.4 to 8.8 days and lifetimes in CAM range from 4.1 to 13.1 days. The largest difference in lifetimes based on dry deposition between SPCAM and CAM is 4.7 days and occurs during July. The months during which the lifetime difference is greater than 4 days include May, June, July, August and September. The calculated dust lifetimes based on wet deposition are much longer than those for dry deposition because wet removal rates are smaller than dry removal rates. The lifetimes range from 8.6 to 16 days for SPCAM and from 9.7 to 14.5 days for CAM. Comparison of the lifetimes by wet deposition between the two models shows that the lifetimes simulated by CAM are shorter than those

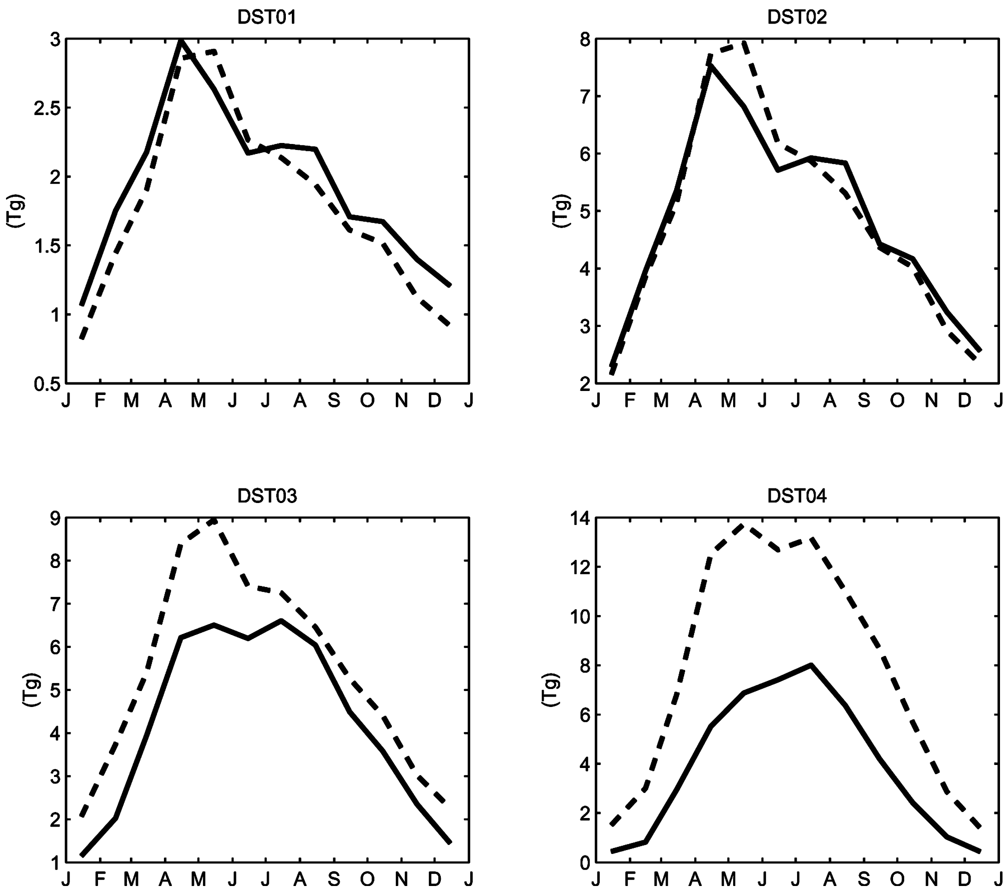

Figure 3.14: Monthly mean dust burden for DST01, DST02, DST03 and DST04. Solid line is SPCAM, dash line is CAM.

simulated by SPCAM for January, February, August, October, November, and December. For all monthly average data, the differences in the lifetimes due to wet deposition between the two simulations are less than the corresponding differences due to dry deposition. The lifetimes calculated based on the total removal rates, i.e., the sum of dry and wet deposition, are shorter by approximately one day in SPCAM as compared to CAM.

If the simulations have reached steady state, the amount of dust emitted is equal to the amount removed by all its sink processes. Figure 3.16 shows the monthly mean ratio of dry and wet deposition to the mobilization flux for SPCAM and CAM. For SPCAM, the dry deposition ratio is greater than the wet deposition ratio for all months. For CAM, the dry deposition ratio is greater than the wet deposition ratio for the most of the months except July and August. The dry deposition ratios plotted in Figure 3.16 reveal that the ratios from SPCAM are higher than those produced by CAM in every month. The maximum values of the ratio are 0.86 in January for SPCAM and 0.78 for CAM. The dry deposition reaches its largest values in the winter season and its minimum values during the summer, whereas wet deposition peaks in the summer season and is minimized in winter. The yearly mean ratio of dry deposition to mobilization is 0.71 (SPCAM) and 0.61 (CAM). For the corresponding ratio of wet deposition to mobilization, the average value is 0.3 (SPCAM) and 0.4 (CAM).

It is shown in Mahowald et al.[2009], the model overestimates dust concentrations in some places but predicts too low in deposition at the same locations. To understand the role of vertical mixing for dust distributions, we examine the relationship between dust vertical profiles and changes of deposition. Figure 3.17 shows the dust lifetime calculation based on total column amount(a) and surface concentration(c) for CAM run. (b) and (d) show the corresponding percentage change for (a) and (c) as calculated as (SPCAM-CAM)/CAM*100. It is seen in general, the magnitude of percentage change is relatively higher for lifetime calculation based on surface concentration, especially in high latitudes for both hemispheres. Most of regions, the percentage change between two lifetime calculation show the difference has the same sign. The opposite sign of percentage change is seen in south India Ocean and south Pacific near the east of Australia. These figures are consistent with horizonal dust difference distributions shown in Figure 3.4 as large difference values are seen in the local spots where the large differences are in the global dust plot. The vertical profiles of dust is determined by the vertical transport schemes, different vertical distributions will lead to different dust dry removal rates. The amount of dust is also affected by wet deposition which is associated with raining frequency Mahowald et al.[2011]. The evolution of dust is a dynamical process, the difference shown in Figure 3.4 suggests vertical profiles changes between SPCAM and CAM are important to change of total deposition. Finally we also examine the relationship between total deposition and column amount and the relationship between total deposition and surface concentration (not shown). We found at least in the model, both column amount and surface concentration are highly correlated with the total deposition. The conclusion from the correlation analysis is both both column amount and surface concentration explain nearly equal amount of variance for the total deposition.

3.6 Conclusion

In this study, we have used a superparameterized version of the CAM model to simulate the global distribution of dust. It is based upon a multiscale modeling framework in which small scale processes are explicitly calculated by cloud resolving models in contrast to the parameterized representations in conventional global climate models. Following the treatment of water vapor in SPCAM, we add the processes of advection, vertical transport, and diffusion for dust in the CRM. The treatment of dust source and sink terms is the same as in the host model, thus our focus is the differences between CAM and SPCAM simulations due to the cloud-system-scale convective, advective and diffusive tendencies resolved by the SPCAM. Comparing SPCAM scheme to the referenced CAM model where vertical transport is based on parameterizations, we find SPCAM simulates less dust in low to mid troposphere but relatively higher concentration in upper troposphere. This dipole difference is partially attributed to the fact that dust is transported more efficiently from the surface to the low

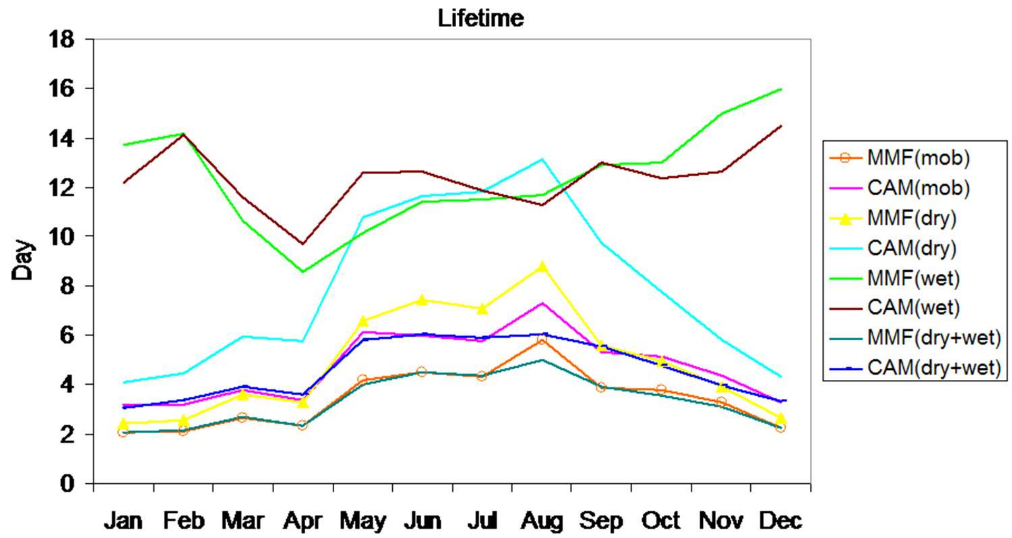

Figure 3.15: Time scale analysis based on mobilization, dry and wet deposition flux

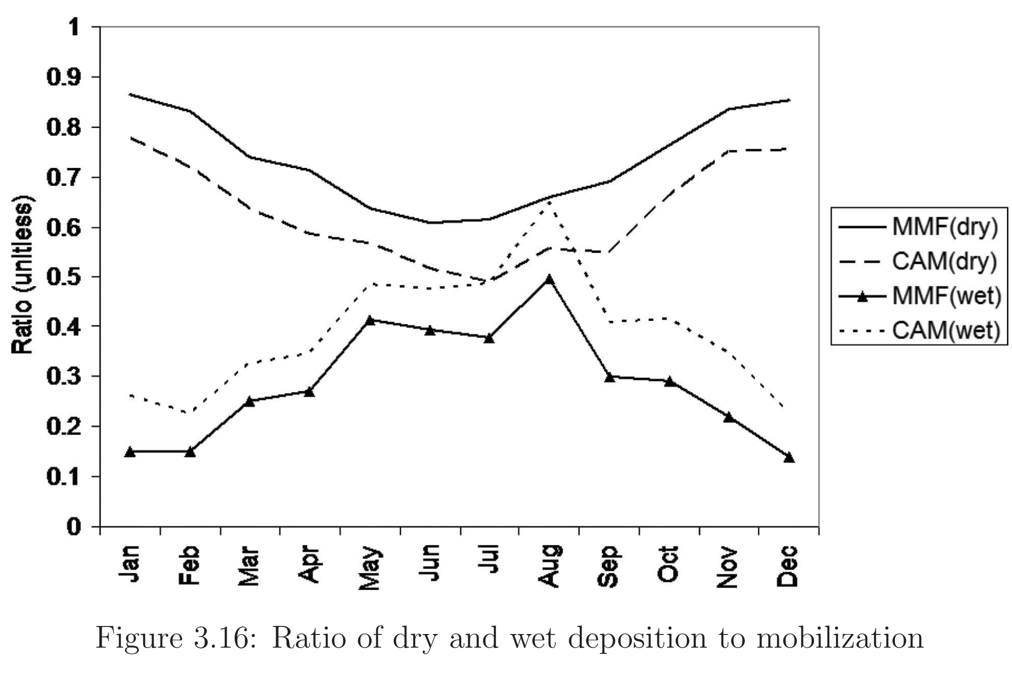

Figure 3.16: Ratio of dry and wet deposition to mobilization

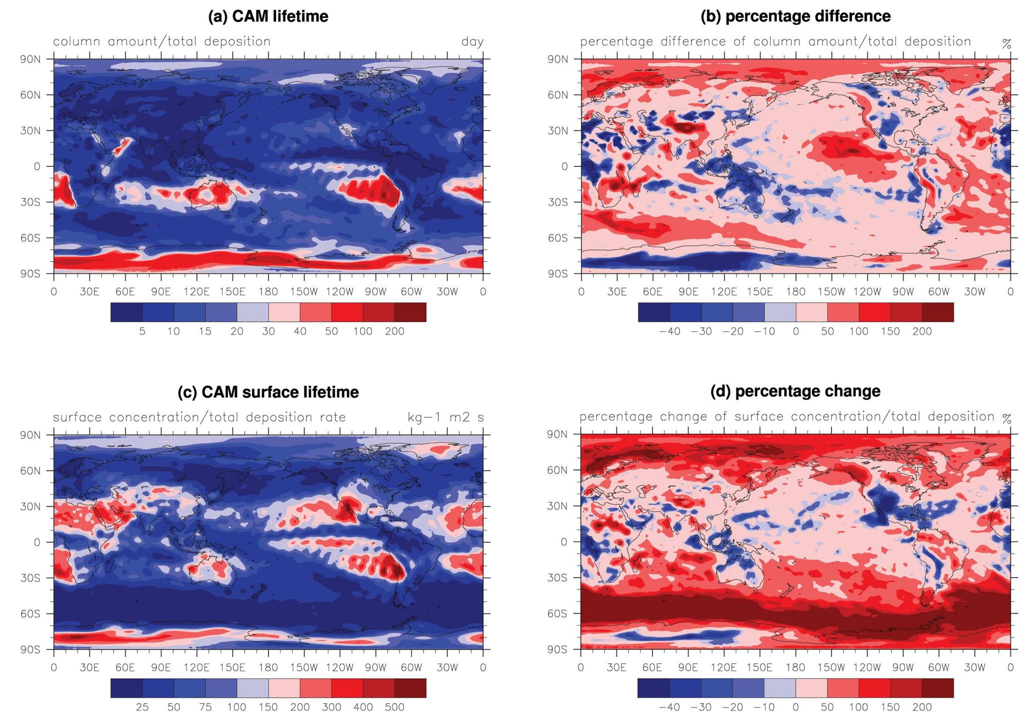

Figure 3.17: (a) Lifetime for CAM as calculated as total column dust amount/total deposition. (b) percentage change of (a), calculated as (SPCAM-CAM)/CAM*100. (c) Lifetime for CAM based on surface concentration calculated as total dust mixing ratio/total deposition. (d) percentage change of (c), calculated as (SPCAM-CAM)/CAM*100.

atmosphere in CAM than SPCAM and because the dry deposition fluxes are substantially higher in SPCAM in the lowest layers of the atmosphere. Another reason for higher dust concentrations in upper troposphere in SPCAM is related to the dust implementation method. The calculations of dust removal processes remain in the larger CAM grid scale, however, it is well known that resolved updrafts are much larger than resolved downdrafts for deep convection. Thus the larger dust mass in upper layers resulting from transport by much larger resolved upward motions in CRM is not removed in the CRM grid scale. This causes a higher concentration of dust in upper troposphere due to deep convection processes. The amount of dry deposition dominates the cumulative mass of dust for the two largest particle size ranges. We found the differences in the annual-mean amounts of dust removed by dry deposition fluxes for the largest two dust bins range from $\sim$ 50 Tg to $\sim$ 300 Tg. While dry deposition is higher in SPCAM , wet deposition is lower in SPCAM relative to CAM. As a direct consequence, the time scale analysis shows the lifetime of dust based on dry deposition is shorter in SPCAM for all months but longer for wet deposition on average. The average burden of dust in the simulated year for SPCAM and CAM is 14.8 Tg and 19.7 Tg, respectively. Our study shows that the introduction of the SPCAM causes substantial changes to the vertical distributions of dust. This demonstrates that the effects of more process-oriented convective-scale vertical transport are manifested in the chemical state of the atmosphere on synoptic to global scales.

Chapter 4

Super-parameterization: A better way to simulate regional extreme precipitation?

In this chapter we present how the distributions of continental convective sub-daily precipitation differ between the conventional and multiscale climate models and how they compare to observationally derived data. Analyzing the precipitation efficiency between models we show that the possible cause for the difference is the higher production of cloud water from vertical convective transport rather than the rate of conversion of cloud water to precipitation from microphysical processes. In the next chapter we compare the multiscale climate model with a group of state of the art climate models.

4.1 Introduction

Extreme precipitation events often have dramatic ecological, economic, and sociological impacts. The simulation and projection of precipitation extremes are of great importance as significant upward trends in the frequency of these events have been detected in recent decades with the warming of the climate [89, 88], and further increases could affect less resilient sectors of society and the environment [107]. Despite the need for robust projections, it has been repeatedly demonstrated that current climate models generally underestimate the occurrence of intense precipitation as reported in several recent studies [25, 10, 71].

The relatively coarse horizontal resolution typical of previous generations of climate models has been proposed as the main reason for the underestimation of extreme precipitation. Recent studies [13, 129] have suggested that low-resolution climate models, particularly those with grid spacings of 1u or more, cannot reproduce the statistics of extreme rainfall events in the historical climate record with sufficient fidelity. Although increases in resolution yield more realistic spatial patterns and probability distributions of precipitation over most continental regions [10], the systematic errors in these properties persist during convective-precipitation dominated seasons, e.g., June-July-August (JJA) and March-April-May (MAM), in the southeast USA [47]. This result is consistent with the finding that convective precipitation appears to decrease while total precipitation appears to increase with greater horizontal resolution [132, 70]. Therefore, while the scale separation between convective and large-scale precipitation is a reasonable approximation in low resolution models, increasing the resolution does not necessarily ensure an accurate simulation of convective precipitation. The reason is that the scale-separation approximation introduced in most parameterizations becomes less accurate as the model resolution approaches the scales of individual convective systems.

A promising approach to improve the representation of subgrid-scale physical processes in climate models is to replace the conventional cloud parameterizations with a high-resolution cloud-resolving model (CRM) embedded into each model grid column. This technique is often designated by super-parameterization (SP) [58, 60] In comparison to conventional parameterizations, SP is conjectured to improve the representation of sub-grid processes since the embedded CRMs can explicitly resolve the interactions among cloud dynamics, cloud and aerosol microphysics, radiation, and turbulence down to cloud-system scales. SP can dramatically improve the diurnal cycle of precipitation over summertime continents [60] while it simultaneously produces reasonable simulations of time-mean precipitation. Iorio et al. [47] further showed that a climate model (CCM3) enhanced using the SP methodology can produce longer tails of the precipitation distribution over the continental United States (CONUS), and [20] indicated that a similar approach can simulate intense rainfall events more correctly.

This study will specifically investigate how the SP approach can be used to simulate the extreme precipitation over the CONUS compared with precipitation produced using a climate model with conventional parameterizations. We focus on the CONUS because of the extensive rain gauge data, which, when appropriately gridded, can be readily used in the comparison. Section 2 presents the description of model framework and the observational precipitation data used to evaluate the conventional and SP-based climate-model simulations. The results are presented in section 3 and conclusions are discussed in section 4.

4.2 Model and Data Description

Model Description

We use the National Center for Atmospheric Research (NCAR) Community Atmosphere Model (CAM) version 3.5.36 as the main modeling framework [16]. For our simulations, we have selected CAM with a finite-volume dynamical core configured with a horizontal resolution of 1.875u latitude 62.5u longitude and 28 vertical levels. At this lateral resolution the model is integrated forward in time using time steps of 30 minutes, and the state of the model is output every 3 hours to capture short-lived hydrometeorological events. Two simulations are performed to investigate the performance of SP in simulating extreme precipitation relative to conventional approaches: (1) CAM with standard parameterizations of cloud and convection processes [17]; and (2) super-parameterized CAM (SP-CAM), with a CRM embedded in each grid cell in place of these standard parameterizations [58].

Details of the configurations of the two simulations have been described by D. Rosa et al. (Global transport of passive tracers in conventional and superparameterized climate models: Evaluation of multiscale methods, submitted to Journal of Advances in Modeling Earth Systems, 2012). The most important aspect is that both simulations have been performed in chemical transport mode, in which CAM fields are replaced by equivalent fields from the NCEP Re-analysis including horizontal winds, temperature, surface pressure, wind stress, sensible heat flux and water vapor flux. This mode of operation insures that the large-scale fields in CAM are fully consistent with a reanalysis for the actual meteorological conditions pertaining to our time series of rain gauge data. These dynamic and thermodynamic fields are linearly interpolated in time to the CAM time step and interpolated in space onto the CAM grid. The CRM embedded in each atmospheric column of CAM is nudged to CAM large-scale fields using relaxation terms [60]. The difference in CAM-grid scale precipitation simulations is from the difference of sub-grid cloud and dynamical processes in the two simulations. Therefore to leading order, we hypothesize that differences between the modeled and observed extreme precipitation are due to systematic errors in the sub-grid physics rather than the large-scale meteorological fields.

The CRM in SP-CAM is a configured as a 2D system with 2 km horizontal resolution. Each CRM domain consisting of 64 columns is aligned in the west-east direction and exchanges information with itself via periodic lateral boundary conditions. Its vertical grid levels are located at the same heights as the 28 levels of CAM. The CRM solves the non-hydrostatic momentum equations with an anelastic approximation (detailed by Khairoutdinov and Randall [58]). A bulk microphysics parameterization is used to compute the hydrometeor conversion rates and terminal velocities. The prognostic thermodynamic variables including the water moist static energy and precipitating water are used to calculate the cloud water, cloud ice, rain, snow and graupel mixing ratios.

The 2-km CRM horizontal resolution is chosen to optimally balance the computational cost and realistic simulation of the formation of the cloud and extreme precipitation. Ooyama [92] showed that 2-km resolution is needed for realistic simulations of precipitating clouds using a 2D non-hydrostatic model, which is in many ways similar to the embedded CRM used in this framework. His tests on the growth of single cell clouds showed that, at 2-km resolution, the rain has more realistic and clearer episodes with the peak rain intensity doubling that in the coarser 4-km experiment, which only produces very gentle and continuous precipitation. Although more complex cloud structure and greater precipitation intensity are seen in 1-km experiment, the 2-km resolution captures the rain episodes and peak intensities reasonably well. These results provide a solid proof of using the 2-km CRM in the SP-CAM framework when taking into account the computation cost. Meanwhile, Ooyama [92] also indicates that increasing the CRMs resolution in the SP-CAM could slightly increase the intensity of extreme precipitation. It may be worth future investigation but the impact of the horizontal resolution of the CRM is not the focus of this framework.

In CAM, the precipitation is parameterized through large-scale and convective precipitation schemes. The mass vertical fluxes are calculated based on the assumption that the cumulus ensemble depletes the convectively available potential energy on a fixed characteristic timescale. However in SP-CAM, each CRM is forced by the grid-scale tendencies from CAM and it then computes the convective tendencies in each column in its domain. The SP-CAM framework thus includes both the large-scale atmospheric vertical motion on the climate model grid and the cloud-scale circulations represented on the CRMs grid [57]. Both scales of the vertical motions are involved in the formation of precipitation, but the conventional climate model parameterizes the distributions of cloud-scale velocities. Khairoutdinov, DeMott, and Randall [57] have shown that, despite the relatively coarse grid spacing of the CRM, the clouds simulated by the CRMs in SP-CAM behave in a manner consistent with our understanding of the stratocumulus dynamics, and that the bulk of vertical transport of water is carried out by the circulations explicitly represented on the CRM grid.

Precipitation Data

We assess the performance of CAM and SP-CAM in simulating extreme precipitation using a rain gauge-based observational precipitation dataset from the NOAA Climate Prediction Center (CPC). The specific product we use is the daily U.S. Unified Precipitation product [41]. The dataset is derived from ,13000 rain gauge station reports collated each day since 1992 using three different data sources: NOAAs National Climate Data Center (NCDC) daily co-op stations, a CPC collation containing River Forecast Centers data first order stations, and daily accumulations from hourly precipitation measurements. The station daily-accumulated precipitation rates are mapped onto a regular 0.25u60.25u grid for the U.S. continent using a Cressman Scheme [18, 12]. after application of quality controls to eliminate duplicative and overlapping stations [41]. The values are accumulated from noon of the day before to noon of each reported day. A ten year period of the gridded dataset spanning 1996 2005 that coincides with the simulation period is used to ensure internal consistency between the models and observations.

Since extreme precipitation normally occurs on sub-daily time scales, we also analyze the simulations at 3-hourly intervals using the gridded hourly CPC precipitation [41]. The hourly precipitation is mapped onto a coarser 262.5 grid covering the contiguous United States using the same Cressman Scheme [18, 12] that is applied to the daily data. The main difference between the daily and hourly gridded precipitation data is that most stations used for the daily product do not record hourly precipitation rates. One-third of the stations used for the hourly precipitation product are first order National Weather Service (NWS) stations, and the remaining stations consist of point measurements from cooperative observers. Since the set of hourly stations is a relatively small subset of the stations used in the daily precipitation product, some differences are expected in the gridded spatial distributions of time-mean precipitation rates. In addition, the hourly precipitation product is less up-to-date and covers only part of the simulation period from 19962001.

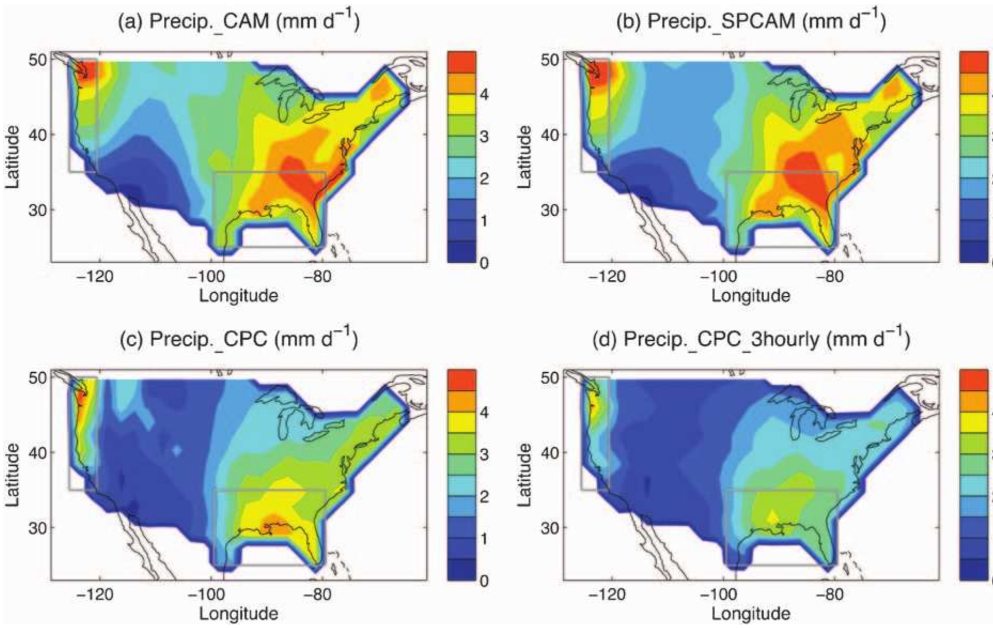

Figure 4.1: Mean precipitation for (a) CAM (19962005), (b) SP-CAM (19962005), (c) daily CPC (19962005), and (d) hourly CPC (19962001) on the same 1.875u latitude x 2.5u longitude model grid. Boxes denote the southeastern and western regions of the U.S. analyzed in section 3.

To facilitate direct comparisons with the simulations, the daily and hourly gridded rain gauge precipitation rates have been re-gridded onto the CAM grid and outer (large-scale) SP-CAM grid using an area weighted interpolation scheme designed to conserve total precipitation. The 3-hourly model outputs are also averaged to daily values when compared to daily observations. Note that the intensities of some extreme precipitation events in the re-gridded data and/or daily data constructed from the 3-hourly data may be significantly reduced by the spatial interpolation and temporal averaging.

4.3 Results

The time-mean distributions of precipitation over the CONUS region for CAM and SP-CAM are shown in Figures 4.1a and 4.1b, respectively. Since both CAM and SP-CAM are strongly constrained by NCEP reanalysis fields including surface moisture flux fields, the spatial patterns of CAM and SP-CAM are very similar as expected. Both simulations show high precipitation rates in the northwestern, eastern, and southeastern US. Relative to CAM, the precipitation is slightly higher in SP-CAM in these wet regions but a little lower in dry middle-west US. This difference implies some fundamental differences in the precipitation statistics between the two models that will be discussed in more detail below.

Table 4.1: The Mean, R95, and R995 Precipitation (mm d^{-1}) From CAM, SPCAM and CPC, Averaged Over Three Regions: a Continental U.S. (CONUS), Southeastern U.S. (SE) and Western U.S. (W). The SE U.S. and W U.S. are defined in section 3 and are the two gray boxes in Figure 4.1.

	Mean			R95			R995		
	CONUS	SE	W	CONUS	SE	W	CONUS	SE	W
CAM	2.9	3.8	3.4	18.5	24.2	22.7	45.8	61.7	50.3
SPCAM	2.8	3.7	3.7	22.7	30.1	26.7	60.8	81.4	54.2
CPC	2.2	3.3	3.0	20.1	32.2	25.2	61.7	89.0	56.7

CAM and SP-CAM generally have higher mean precipitation rates than CPC rain gauge precipitation over the CONUS region (Figure 4.1): ,30% higher for the region averaged mean daily precipitation (Table 4.1). The excess precipitation is primarily related to the differences between NCEP precipitation [55] and CPC precipitation fields at large scales (Figures 4.1c, 1d, and 2) and to the underestimation of topographic effects from the Rocky Mountains due to the coarse spatial resolutions of the models. Over the eastern US, the maximum precipitation in CPC occurs in the states adjacent to the Gulf of Mexico, while the precipitation in CAM and SP-CAM peaks in the central and Mid-Atlantic States. In addition, due to the sparser sampling rain gauge stations, the CPC 3-hourly precipitation (Figure 4.1d) is generally lower than the CPC daily precipitation although the two datasets share similar spatial patterns.

The similarity in the mean precipitation between CAM and SP-CAM is expected since we constrain both models with large-scale dynamic and thermodynamic fields from the NCEP reanalysis (Figure 4.2). However at the level of corresponding grid points from each model, the two representations of subgrid cloud and convective processes are free to operate very differently subject to the nearly identical boundary conditions imposed on both grid points. Our experiments are designed to assess if the embedded CRM can better resolve extreme precipitation within the CAM model grid compared to the conventional precipitation parameterizations when forced by the same realistic meteorological fields. We show the simulated and observed extreme precipitation in Figure 4.3 and their region averaged values in Table 4.1.

The definitions of extreme precipitation used in this study are determined by high percentile thresholds applied to the daily and 3-hourly precipitation derived from the Frich indices with slight modifications [31, 2]. To facilitate our analysis, the units of the extreme precipitation indices have been converted from the yearly total extreme precipitation (mm yr^{-1}) to the daily-mean intensity of the extreme events (mm d^{-1}). We first find the value for the nth percentile precipitation during all the wet events (.1 mm d^{-1}) at the same location for a whole year. The extreme precipitation index Rn is defined as the mean precipitation intensity for all the extreme events larger than the nth percentile value. We choose R95 (rates exceeding the 95th percentile value) for daily precipitation and R995 (rates exceeding

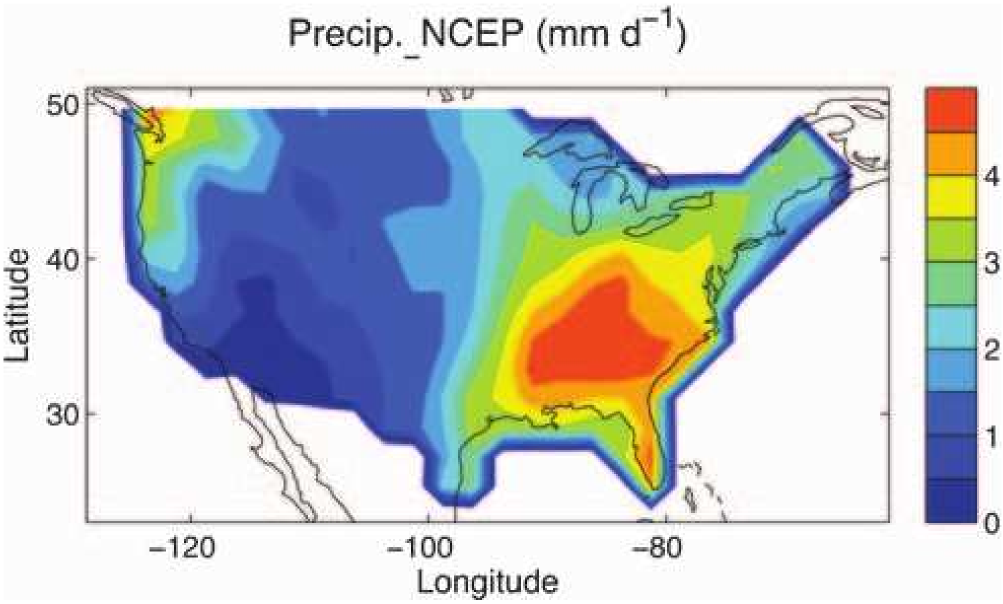

Figure 4.2: Mean precipitation from NCEP Re-analysis 6-hourly precipitation (19962005).

the 99.5th percentile value) for 3-hourly precipitation to have enough samples (,1020 events per year) for robust statistics.

The R95 daily extreme precipitation is shown in Figure 4.3a for CAM, Figure 4.3c for SP-CAM, and Figure 4.3e for CPC observations. The extreme precipitation simulated by SP-CAM is significantly higher than that in CAM although the spatial distributions of mean precipitation appear to be very similar (Figures 4.1a and 1b). SP-CAM simulates more extreme precipitation over almost the entire CONUS region, particularly in southeastern and western coastal US. While CAM exhibits a characteristic underestimation of extreme precipitation (Figures 4.3a and 4.3c) as noted in many previous studies [10, 71], the spatial distribution and intensity of the extreme precipitation in SP-CAM much better matches the extreme precipitation derived from CPC rain gauge observations. For instance, the region averaged R95 precipitation over southeastern (SE) U.S. in CAM is ,25% lower than that in CPC, while the R95 from SP-CAM is only ,7% lower (Table 4.1). While the changes in precipitation from CAM to SP-CAM represent an improvement over much of the CONUS region, SP-CAM does not capture some of the very extreme values along the southeastern and eastern coasts and it overestimates extreme precipitation over dry western mountainous regions.

Although the CPC daily precipitation is deemed more reliable because of the larger number of rain gauge stations used to construct it and the longer duration of the data record, the 3-hourly data may yield additional information at the sub-diurnal time scales most relevant to extreme precipitation. Figures 4.3b, 4.3d, and 3f show the spatial distributions of the

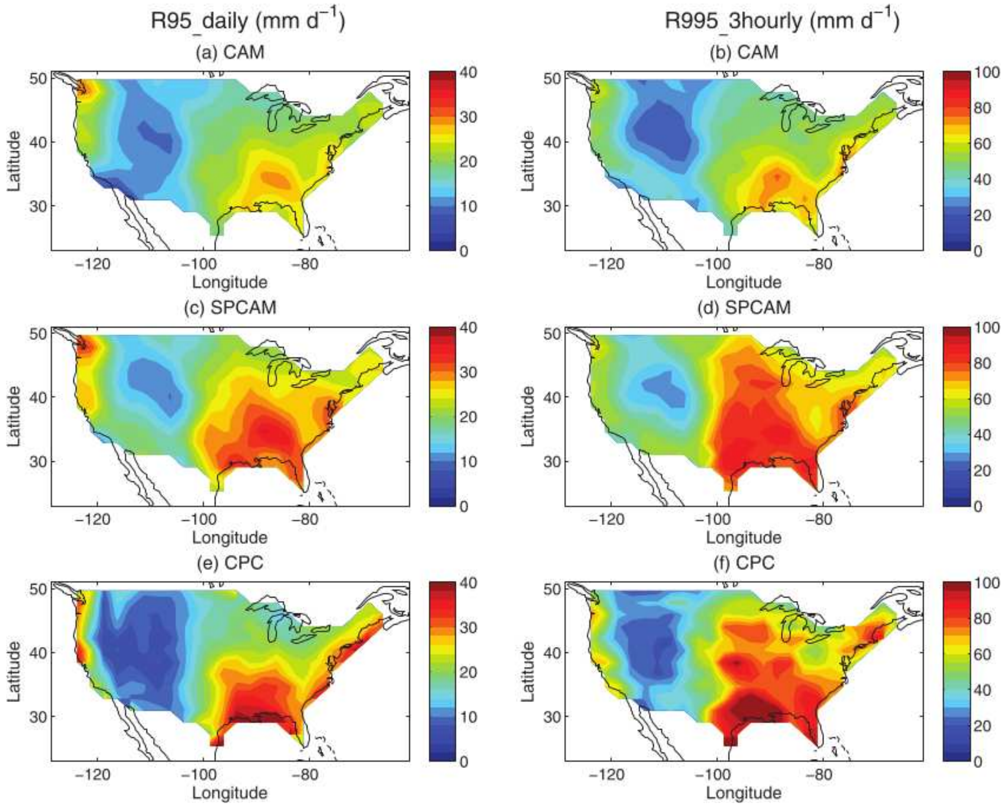

Figure 4.3: Simulated and observed U.S. extreme precipitation: 95th percentile daily precipitation for (a) CAM, (c) SP-CAM, (e) CPC; and 99.5th percentile 3-hourly precipitation for (b) CAM, (d) SP-CAM, (f) CPC.

R995 (. 99.5th percentile) extreme precipitation estimated using the 3-hourly CAM and SP-CAM output and CPC data set, respectively. Similarly to the daily extreme precipitation, the conventionally parameterized CAM greatly underestimates this measure of extreme precipitation while SPCAM agrees much better with the CPC observations (also see Table 4.1), particularly in the eastern CONUS. SP-CAM still misses some very extreme precipitation events such as those in Texas, but its general spatial patterns agree quite well with the CPC data. In general, the differences between CAM and SP-CAM (and between CAM and CPC) at 3-hourly time scales are much larger than those for daily extreme precipitation. This larger bias of CAM in 3-hourly extreme precipitation is expected due to the higher percentile threshold used which decreases the sample size and due to the shorter time scale which will be discussed in the next section.

Probability Distribution

The results above show that SAM and SP-CAM produce similar spatial patterns of mean precipitation but produce quite different patterns and intensities of extreme precipitation. The difference indicates a shift of precipitation probability distributions towards higher extremes in SP-CAM relative to CAM. Figure 4.4 thus shows the probability density distribution of precipitation for CAM, SP-CAM and CPC. In addition to the whole CONUS region, we also analyze two sub-regions with high extreme precipitation: the southeastern U.S. between 25-35° N and 80-100° E and the western U.S. between 35-50° N and 55-60° E, defined as the two gray boxes in Figure 4.1. The precipitation is aggregated in 2 mm d^{-1} bins from 0 to 120 mm d^{-1}. Any precipitation rates larger than 120 mm d^{-1} are assigned to the last bin.

Figure 4.4a shows the probability distribution for the daily precipitation over the CONUS region. CAM exhibits its characteristic underestimation of precipitation for heavy precipitation larger than 30 mm d^{-1}. The precipitation distributions from SP-CAM are generally in better agreement with the CPC observations particularly since SP-CAM simulates more light precipitation (<10 mm d^{-1}) and more heavy precipitation (>30 mm d^{-1} 21) than CAM. However, the frequency of the daily extreme precipitation from SP-CAM degrades at rates exceeding 60 mm d^{-1} and is comparable to that in CAM. The precipitation distribution over the southeastern U.S. (Figure 4.4c) is generally similar to that over the CONUS region (Figure 4.4a). The probability distributions from SP-CAM and CPC are in better agreement over the southeastern US, while CAM underestimates the probability of precipitation for rates exceeding ,15 mm d^{-1}. Over the western coastal US, the probability distributions from both CAM and SP-CAM are in much better agreement with the CPC distribution (Figure 4.4e). However, the much larger area of the southeastern region relative to the western coastal zone implies that the distributions of extreme rainfall exceeding 30 mm d^{-1} are determined primarily by the southeastern region.

In order to evaluate the simulation of sub-diurnal extreme events, the probability distributions of 3-hourly precipitation have been constructed as shown in Figures 4.4b, 4.4d, and 4.4f for the CONUS, southeastern US, and western US, respectively. Note that daily-mean precipitation rates calculated from diurnally averages of the 3-hourly dataset are not the same as the published CPC daily precipitation dataset. The reason is that the CPC 3-hourly precipitation dataset is derived from a subset of the daily rain gauge stations for just the first half of the daily dataset record, For consistency with the 3-hourly observations, the CAM and SP-CAM precipitation statistics shown here correspond to just 1996 2001 rather than the whole 10 year period for daily precipitation.

The 3-hourly distributions show more extreme high and low precipitation rates compared to the daily distribution, as the daily temporal averaging eliminates the most extreme values. Over the entire CONUS region and southeastern US, the similarities and differences among the distributions of precipitation from CAM, SPCAM, and CPC resemble those obtained in the comparisons of the daily data. For both the CONUS region and southeastern US, CAM overestimates the probability of moderate precipitation and underestimates the probability the heavy precipitation relative to CPC (Figures 4.4b and 4d). The SP-CAM distribution is

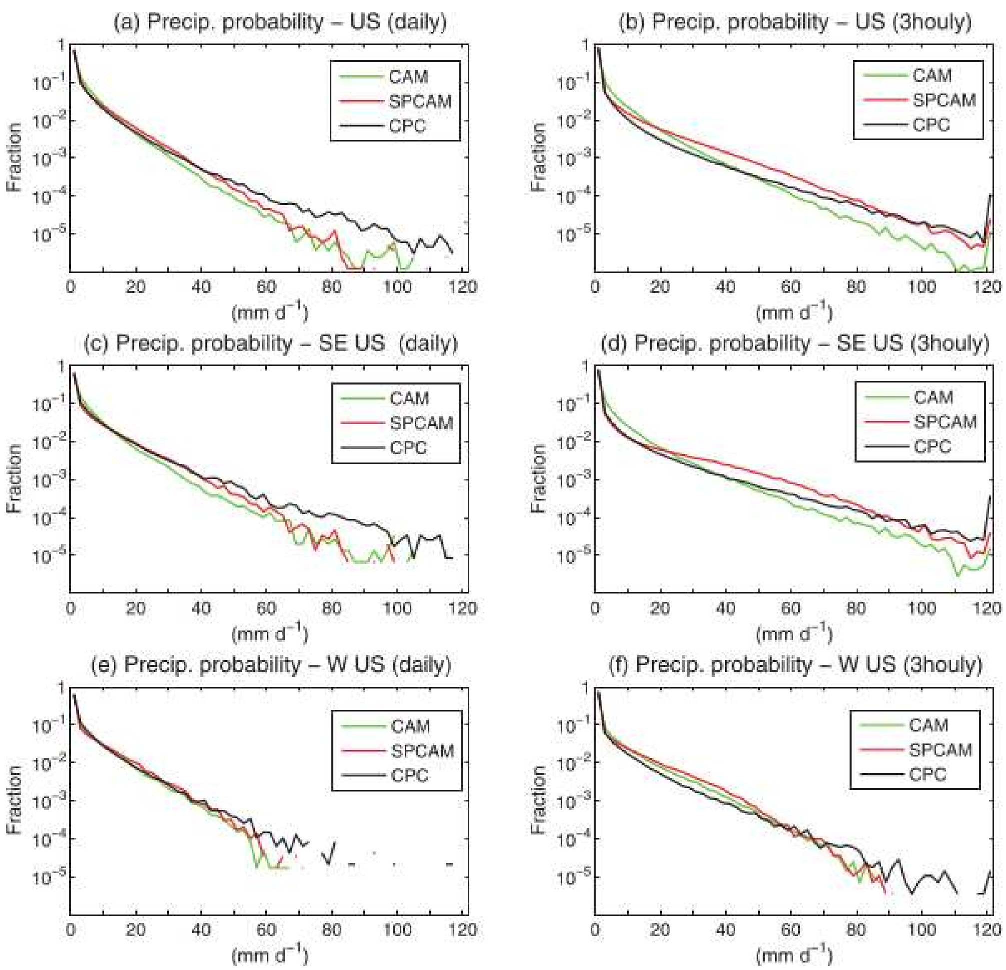

Figure 4.4: Probability density distributions of (a) U.S. daily precipitation; (b) U.S. 3-hourly precipitation; (c) southeastern (SE) U.S. daily precipitation; (d) southeastern (SE) U.S. 3-hourly precipitation; (e) western (W) U.S. daily precipitation; and (f) western (W) U.S. 3-hourly precipitation. Green, red, and black lines respectively represent the CAM, SP-CAM, and CPC.

in good agreement with that of CPC in conditions of light and heavy precipitation, although SP-CAM does overestimate the likelihood of moderate precipitation. The difference between CAM and SP-CAM is small over western U.S. apparently due to the relative frequency of various types of precipitation characteristic of this region. This feature is discussed in the next section.

Seasonal Variation of Probability Distribution

The precipitation in CAM is parameterized as two separate processes representing convective and large-scale precipitation. In the real world, convective processes are more important in the southeastern U.S. than in the western coastal region where large-scale air motions (e.g., synoptic-scale frontal systems) are the principal driving mechanism for precipitation. The notable improvement in the simulation of the extreme precipitation distribution by SP-CAM in the southeastern U.S. is therefore likely due to the improved representation of subgrid convective processes in the CRMs embedded in SP-CAM. Similarly, the resemblance between CAM and SP-CAM over the western U.S. (Figure 4.4) should be expected because large scale air motions are prescribed when running in Chemical Transport Mode and therefore both models provide identical conditions for the formation of large-scale precipitation. Consequently, the seasonal variation of precipitation should also be improved as convective processes dominate summer precipitation over much of the CONUS.

Figure 4.5 shows probability distribution of U.S. precipitation in JJA (Figures 4.4a and 4.4b) and in DJF (Figures 4.4c and 4.4d). For the convectively dominated summertime daily precipitation (Figure 4.5a), SP-CAM clearly simulates a much better distribution than CAM although it is still unable to capture the most extreme precipitation observed by CPC. CAMs underestimation of the high rain-rate tail of the precipitation distribution is more obvious in summer (JJA) than in the annual total (Figure 4.4a). The wintertime (DJF) difference between CAM and SP-CAM is much smaller than that in summer, reflecting the diminished importance of convective processes during this season. At the 3-hourly time scales, these differences are even more robust and the CAM simulated summertime precipitation probability distribution differs appreciably from the CPC distribution. Again, SP-CAM offers significant improvements over CAM. Although it overestimates the moderate precipitation, it captures the higher end of the distribution very well (Figure 4.5b). These results suggest SP-CAM appears to have better fidelity to the observational record for both light and extreme precipitation during the convective precipitation dominated season. As for the daily precipitation distribution, the differences between CAM and SP-CAM 3-hourly distributions are small for the winter season when large-scale precipitation predominates. Both models simulate the observed distribution with comparable levels of accuracy (Figure 4.5d).

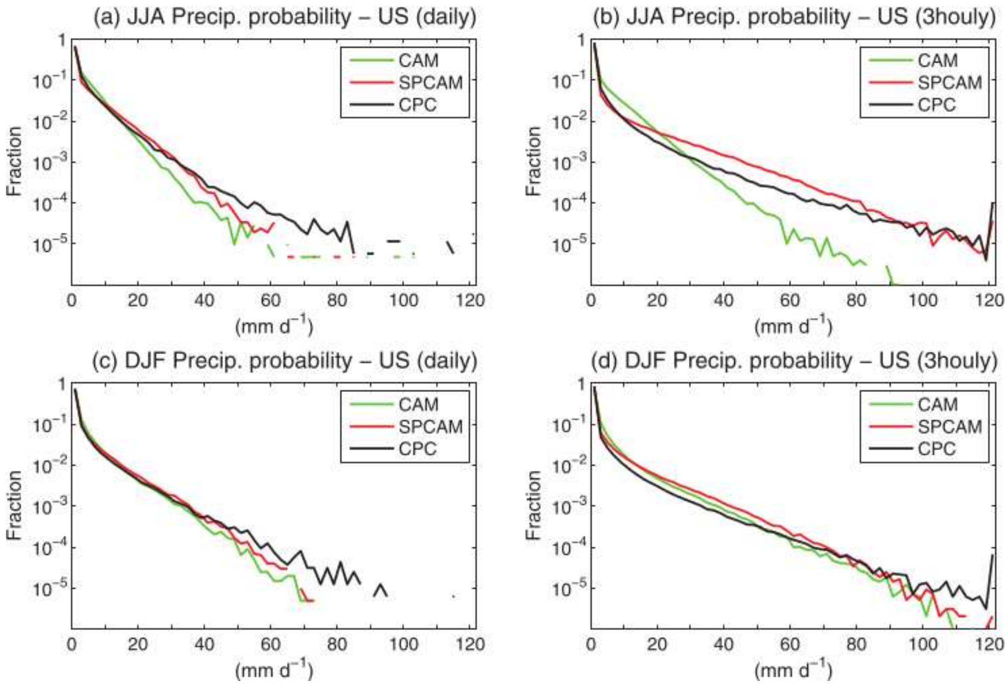

Figure 4.5: Probability density distributions of (a) JJA U.S. daily precipitation; (b) JJA U.S. 3-hourly precipitation; (c) DJF daily precipitation; and (d) DJF 3-hourly precipitation.

The Roles of Cloud Physics and Dynamics in Intermodel Differences

Differences in large-scale dynamic and thermodynamic fields cannot cause the differences in extreme precipitation simulated by CAM and SPCAM since these fields are constrained by the same NCEP-reanalysis data at each model time step and are therefore almost identical in our two simulations. Instead, the differences can be attributed to some combination of three main subgrid-scale processes: (1) the advection of water vapor to altitudes above its lifted condensation level (LCL) in convective updrafts; (2) the condensation of the resulting supersaturated vapor to form cloud water and ice; and (3) the conversion of this cloud condensate to precipitation. The first process is governed primarily by rates of subgrid vertical advection and the latter two are determined by cloud microphysical processes for condensation and collisional coalescence. An assessment of which of the three subgrid processes explains the different statistics of extreme precipitation in CAM and SP-CAM would provide insights into how best to improve the simulation of cloud and precipitation in climate models.

Due to the challenges posed by retrospective analysis of the sub-grid physics and parameterizations and due to the absence of suitable run-time diagnostics, we do not have sufficient information to individually quantify the differences in the first two processes associated with moisture lifting or cloud condensation. Their combined effects, however, are reflected in the total cloud water produced by CAM and SP-CAM. The third process, e.g., conversion from cloud water to precipitation, can be quantified using a precipitation efficiency f defined as the ratio of precipitation rate to the total grid box cloud water path. The parameter f has units of 1/ days and represents the inverse timescale for the conversion of cloud condensate to precipitation. Hence larger values of f correspond to shorter timescales for the conversion process.

The total cloud condensate path and total precipitation amount for all the summer precipitation events are shown in Figures 4.6a and 4.6b, respectively. The 80 mm d^{-1} upper boundary is chosen since there is almost no precipitation larger than 80 mm d^{-1} in CAM. We accumulate all the precipitation events falling into a given precipitation bin to obtain the total amounts of cloud condensate and precipitation. The efficiency f for each bin is estimated by dividing the total precipitation amount by the corresponding total cloud condensate path.

The total cloud condensate in SP-CAM is much higher than the condensate in CAM for heavy precipitation events. The condensate paths in SP-CAM are almost two orders of magnitude higher than those in CAM at precipitation rates approaching 80 mm d^{-1} (Figure 4.6a). The magnitude of this difference corresponds well with the magnitude of differences in the precipitation amount (Figure 4.6b) and probability distribution (Figure 4.5b). In addition, the precipitation efficiency of SP-CAM exceeds that in CAM by approximately 20% for all precipitation intensities higher than 30 mm d^{-1} (Figure 4.6c). This shows that the microphysics for the conversion of cloud condensate to hydrometeors in SP-CAM produces precipitation 20% faster than the corresponding parameterizations in CAM given identical amounts of cloud water in the two models. However, the magnitude of this difference in conversion rates is one to two orders of magnitude smaller than the total differences in extreme precipitation. These results suggest that improvements in extreme precipitation simulated by SP-CAM are caused primarily by differences in the representation of moisture advection and cloud condensation, the two remaining subgrid processes. In particular, the moisture-advection process is fundamentally different in CAM and SPCAM since the bulk of vertical water transport is due to small-scale circulations explicitly represented on each CRMs grid.

4.4 Conclusion and Discussion

This study has evaluated a new approach for simulating extreme precipitation over large spatial scales based upon replacing conventional parameterizations with CRMs in a global GCM. We perform two experiments to evaluate this approach contrasting the standard Community Atmosphere Model (CAM) and a super-parameterized CAM (SP-CAM) with the grid-scale tendencies in both experiments constrained by identical NCEP reanalysis fields. Under this framework, the differences between the two experiments are solely due to differences in subgrid process representations between CAM and SP-CAM. While cloud microphysical processes are parameterized in both models, convective updrafts and downdrafts are explicitly

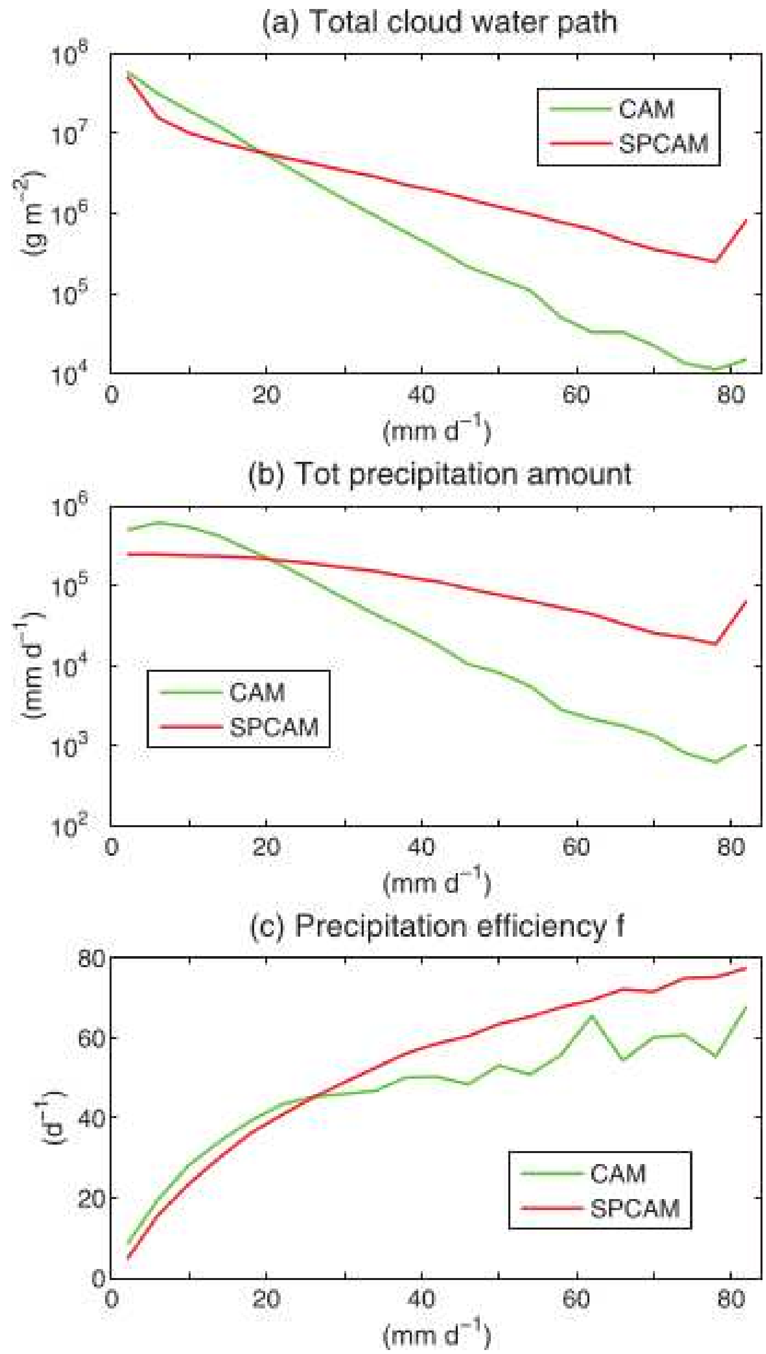

Figure 4.6: (a) Total could water path and (b) total precipitation amount, accumulated in 4 mm d^{-1} precipitation intensity bins, for all the 3-hourly precipitation events during JJA from 1996 to 2001 over CONUS. (c) Precipitation efficiency f 5 precipitation rate / total grid box cloud water path.

resolved in SP-CAM at the resolution of the embedded CRMs. Gridded estimates of U.S. precipitation derived by the CPC from rain gauge data are used to evaluate the simulated statistics of extreme precipitation.

Our results show that more extreme precipitation is simulated by SP-CAM than by CAM over almost all the CONUS region despite the fact that both models simulate very similar distributions of mean precipitation. Compared to the CPC estimates, SP-CAM is much better agreement than CAM in both the spatial distribution and intensity of extreme precipitation, especially at very high rain rates (99.5% percentile) and short (3-hourly) time scales. While the underestimation of extreme precipitation by CAM, as well as other GCMs, has been previously reported [10, 70], it is encouraging to see the improvement with the implementation of CRM.

A closer look at the probability distribution of the precipitation shows that the distribution produced by SP-CAM generally agrees with the CPC observations better than that produced by CAM. SP-CAM simulates more light precipitation and more heavy precipitation and this improvement is especially pronounced at 3-hourly time scales, although the ability of SP-CAM to simulate very extreme precipitation (e.g., daily rates in excess 60 mm d^{-1}) remains limited.

Distinct differences in the CAM and SP-CAM simulations are found in the two regions with the most extreme precipitation: the southeastern U.S. and the western coastal US. Over the southeastern US, SPCAM agrees considerably better with the CPC in the distribution of precipitation than CAM at both the daily and 3-hourly time scales. However, the difference between CAM, SP-CAM, and CPC is much smaller at both of these time scales in the western coastal US. Since convective processes are a more important source of extreme precipitation in the southeastern U.S. while the extreme rainfall in the western coastal U.S. is largely due to large scale air motions, these regional differences imply that improvements obtained with SP-CAM are due primarily to the enhanced treatment of subgrid-scale convective processes. The seasonal variation of the precipitation distribution confirms that convective processes are the key in improvement of SP-CAM over CAM. During the convective dominated summer season, SP-CAM clearly outperforms CAM, particularly at 3-hourly time scales. The summertime precipitation distribution simulated by CAM is clearly less realistic than that simulated by SPCAM. This validates the expectation that the subgrid convective processes, not the large-scale air motions, are better represented by the SP-CAM.

The subgrid dynamics and physics are purported to be better resolved at the cloud scale and hence potentially more realistic in SP-CAM, Several subgrid processes could potentially result in the more extreme precipitation produced by SP-CAM, including moisture advection, cloud condensation, and the conversion from cloud water to precipitation. We show that SP-CAM has somewhat higher cloud-water-to-precipitation conversion efficiency than CAM for moderate to high precipitation and that the greater efficiency contributes to some of the improvement of SP-CAM in simulating extreme precipitation. However, the major difference between CAM and SP-CAM is due to SP-CAMs ability to produce much more cloud water during the heavy precipitation events, although we are not able to quantify the relative importance of moisture advection and cloud condensation in the cloud condensate production in the current experiments.

Bridging between conventional GCMs and global scale CRMs, SP-CAM appears to be a new promising approach of simulating and projecting the changes and trends of extreme precipitation in regions of the world where convective processes are significant. With the increased availability of computation resources, more tests and assessments of SP GCMs or ultimately global-scale CRMs should be carried out and the results would provide key information to improve the physical representations of extreme precipitation in the models for robust simulations and projections.

Chapter 5

A case study of sub-daily simulated and observed continental convective precipitation: CMIP5 and multiscale global climate models comparison.

In this chapter we compare the multiscale climate model with a group of state of the art climate models and with observationally derived precipitation data on sub-daily continental convective precipitation. We discuss model biases in relation to the assumptions made in the convective precipitation schemes of each model. In the next chapter we present work in progress on simulating the Indian monsoon rainfall using the multiscale climate model and accounting for the contribution of anthropogenic aerosols.

5.1 Introduction

It is difficult to quantify the cost of extreme climatic event impacts on human population [28, sect. 4.5.4] but it is certain that extreme events result in severe damage to property, destruction of environment, and loss of life. We have studied the characteristics of extreme rainfall that causes floods and landslides. Its occurrence is underestimated in Global Climate Models (GCM) [116] and this bias can affect decisions at both the individual and the community level.

Rainfall estimates in GCMs depend on the theoretical treatment of several atmospheric and surface physical processes. Though many processes contribute to rainfall, heavy rainfall is mainly due to cloud cumulus convection (CC). This physical process has been approached in different ways to make it operationally affordable [3]. Our goal is to investigate which approaches best estimate the observed frequency distribution of heavy rainfall by analyzing data from conventional GCMs that have different CC parameterizations, and from a multiscale GCM which resolves cloud processes explicitly and has been shown to compare better

Name	Grid	Description
CPC	2°x2.5°	Climate Prediction Center of National Oceanic and Atmospheric Administration (USA). Gridded rain gauge data. [41]
SPC_CTM	2°x2.5°	Center for Multiscale Modeling of Atmospheric Processes (USA). Explicit simulation of cloud processes on a 2 dimensional Cloud Resolving Model. Mass flux from buoyancy. [105]
CAM3.5_CTM	2°x2.5°	National Center for Atmospheric Research (USA). CAPE from undiluted plume. Mass flux from *Quasi-equilibrium* assumption and fixed time-scale for CAPE consumption. No inhibition/suppression. [105]
ACCESS1-3_A	1.2°x1.9°	Commonwealth Scientific and Industrial Research Organization and Bureau of Meteorology (Australia). Described as "CAPE closure scheme based on relative humidity" from a personal communication with Hirst, T. (CSIRO, Australia).
BNU-ESM_A	2.8°x2.8°	Beijing Normal University. CAPE from undiluted plume. Mass flux from *Quasi-equilibrium* assumption and fixed time-scale for CAPE consumption. No inhibition/suppression. (http://esg.bnu.edu.cn/BNU_ESM_webs/htmls/)
CCSM4_A	0.9°x1.2°	CAM4 National Center for Atmospheric Research (USA). CAPE from entraining plume. Mass flux from *Quasi-equilibrium* assumption and fixed time-scale for CAPE consumption. No inhibition/suppression. [33]
CMCC-CM_A	0.7°x0.8°	Centro Euro-Mediterraneo per I Cambiamenti Climatici (Italy). CAPE from undiluted plume. Mass flux from resolution dependent time-scale for CAPE consumption. Positive sub-cloud layer moisture convergence requirement. [109]
CNRM-CM5_A	1.4°x1.4°	Centre National de Recherches Meteorologiques (France). Mass flux from in-cloud minus environment moist static energy and positive sub-cloud layer moisture convergence requirement. [125]
GFDL-CM3_H	2°x2.5°	Geophysical Fluid Dynamics Laboratory (USA). CAPE from undiluted plume. Mass flux from fixed time-scale CAPE consumption. CAPE relaxed to positive value. [24]
HadGEM2-A_A	1.2°x1.9°	Met Office Hadley Centre (UK). Mass flux empirical formulation proportional to initial parcel buoyancy in excess of a threshold. [84]
MIROC-ESM_H	2.8°x2.8°	Japan Agency for Marine-Earth Science and Technology (Japan). CAPE from undiluted plume. Mass flux from *Quasi-equilibrium* assumption and fixed time-scale for CAPE consumption. Suppression if less than RH threshold. [128]
bcc-csm1-1-m_A	1.1°x1.1°	Beijing Climate Center (China). Free troposphere CAPE from undiluted plume. Mass flux from *Quasi-equilibrium* assumption and fixed time-scale for CAPE consumption. Suppression if less than RH threshold. [133]

Table 5.1: Observational and simulated data sources and descriptions. The suffixes CTM, A, and H for the simulation Name stand for Chemical Transport Mode (forced with NCEP), AMIP (forced sea ice and surface temperature), and Historical (prescribed realistic atmospheric composition), respectively. CAPE and RH stand for Convective Available Potential Energy and Relative Humidity, respectively. *Mass flux* refers to the vertical component. As we have not been able to find the details of the mass flux closure for ACCESS1-3_A, we will include this GCM in the analysis without discussing its behavior.

to observations [72].

Our case study is the well-populated and highly convective [40] Southeastern US between the latitudes 30 and 40 $°N$ and longitudes 265 and 280 $°E$. We analyze the months from May to August for the years 1996-2001 of the Climate Prediction Center spatially gridded hourly rainfall rate estimates from rain gauges (CPC) [41]; of CMIP5 simulations [119]; and of a conventional and a multiscale GCMs [105] forced with meteorological NCEP reanalysis [55]. Nomenclature and descriptions are in Table 5.1.

Simulated data is 3-hourly or it is linearly interpolated in time from lower frequency values, then it is linearly interpolated in space to the 2°x2.5° CPC grid. CPC is averaged to 3-hourly.

Although CPC has biases deriving from instrumental errors and analytical methods for gridding unevenly spaced point-source measurements [40], we believe it is the best available observational data for the analysis we present here.

5.2 Results

We test the sensitivity of rainfall to atmospheric instability estimated here with $\Delta\theta_v = \theta_{v\mathrm{Sfc}} - \theta_{v850}$, where $\theta_{v<\cdot>} = T_{<\cdot>}(1+0.61q_{<\cdot>})(p_{Sfc}/p_{<\cdot>})^{R_a/c_p}$, T is temperature, q is specific humidity, p is pressure, R_a and c_p are gas constant and specific heat of air. Subscripts Sfc and 850 stand for surface and 850 hPa.

CPC reports only rainfall greater than $\sim$ 1 mm/day, hence we set to zero all rainfall below 1 mm/day in simulations. This produces a deficiency between 1 and 4 % in total rainfall.

For each dataset we use $\Delta\theta_v^{All}$ for all the precipitation events (about 370K points) and $\Delta\theta_v^{90}$ for the events in the upper 90^{th} percentile of $\Delta\theta_v$ which we consider the subset with high atmospheric instability to CC.

Rainfall diurnal cycle

CPC diurnal partitioning of average rainfall differs between the northern and southern regions of our case study area (Fig. 5.1). For the entire area, the diurnal cycle is similar to the cycle in the southern region but weaker. In the southern region (30 to 34 $^\circ N$) rainfall peaks around 18:00 and reaches its minimum, half of its maximum, at 3:00. In the northern region (36 to 40 $^\circ N$), the diurnal cycle is very weak with a maximum at 6:00 being about 10% more than its minimum at noon. Simulations have a stronger diurnal cycle which is similar between the regions, and they have a lead on CPC of 3 to 6 hours. Simulations are more synchronous to the development of convective instability and continue to produce an early onset bias [19]. SPC_CTM is overall more similar to CPC but does not differ qualitatively between the regions. bcc-csm1-1-m_A fails to reproduce the diurnal cycle of rainfall in the southern region but is the model that does best for the northern region. CAM3.5_CTM and BNU-ESM_A differ even though they share the same parameterization for CC. The reanalysis data forced CAM3.5_CTM estimates a weaker diurnal cycle. In this simulation, local surface evaporation and the profiles of temperature and horizontal winds are prescribed, whereas in BNU-ESM_A CC is free to interact with the large scale environment.

Rainfall intensity

Simulations estimate higher average rainfall in comparison to CPC (Fig. 5.2, top). In relative terms, the bias is greater for $\Delta\theta_v^{90}$, hence it increases with atmospheric instability (Fig. 5.2, middle). For $\Delta\theta_v^{90}$, simulated rainfall is primarily from CC rather than stratiform rainfall (Fig. 5.2, bottom). The fraction of convective rainfall decreases for $\Delta\theta_v^{All}$ but remains large, between 50 to 80%. Such partitioning is not available for SPC_CTM and CPC but Yang

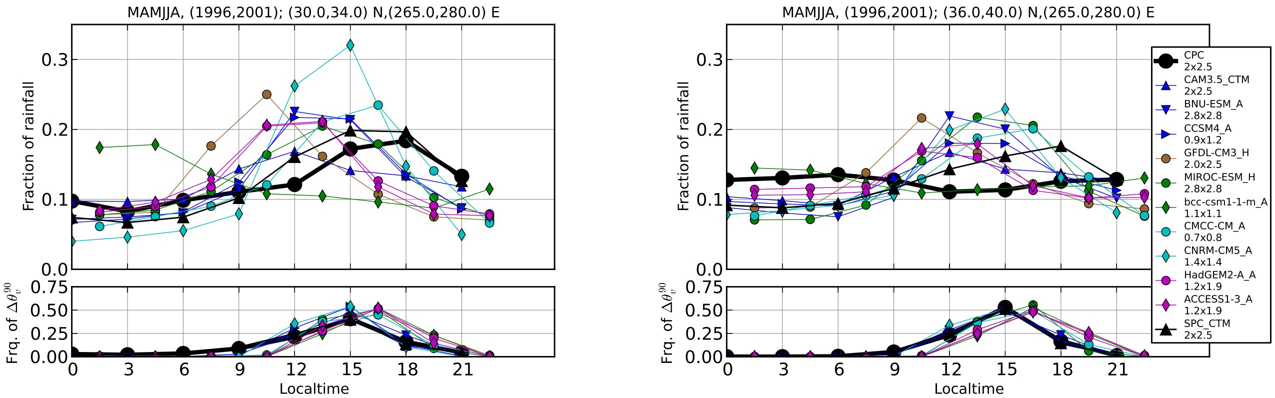

Figure 5.1: Observationally derived and simulated fraction of total rainfall (top) and $\Delta\theta_v^{90}$ (bottom) in relation to local time, calculated from data for latitudes 30 to 34 $^\circ N$ (left) and 36 to 40 $^\circ N$ (right), and longitudes 265 to 280 $^\circ E$, from May to August, 1996 to 2001.

and Smith [136, Fig. 5] estimate a zonal continental value from satellite measurements. The simulations analyzed here capture the increase of the convective component between spring and summer (not shown) but overestimate absolute amounts and differ greatly among each other, especially for $\Delta\theta_v^{All}$.

For CPC, all rainfall intensities larger(smaller) than 1 mm/day occur more frequently for $\Delta\theta_v^{All}$ ($\Delta\theta_v^{90}$) than for $\Delta\theta_v^{90}$ ($\Delta\theta_v^{All}$) (Fig. 5.3). Only a few simulations show this feature. In general, the sensitivity of rainfall intensities to atmospheric instability is higher for simulations than for CPC. There are appreciable biases for $\Delta\theta_v^{All}$ to the extent that the frequency of rainfall is overestimated for middle intensity, between 1 and 10 mm/day, and underestimated below(above) 1(50) mm/day of intensity (Fig. 5.3, right). These biases become larger for $\Delta\theta_v^{90}$: the higher the convective instability the greater the biases from simulations.

Our findings are consistent with the results for a larger region from Dai [19]. However, the difference is the following: for our case study, it is the frequency of rainfall between 1 and 10 mm/day that is overestimated whereas the frequency of lighter rainfall is underestimated.

Rainfall persistence

For each atmospheric column, we calculate the ratio between the number of times a 3-hourly rainfall rate greater than or equal to 75 mm/day is repeated multiple times within 1 following day, to the total number of 75 mm/day events. We do similar calculations for the persistence of light rainfall for events smaller than or equal to 1 mm/day repeated multiple times within 5 following days. The threshold values are discretional, hence these results need be evaluated in relation to the frequencies of rainfall intensities (Fig. 5.3). We have chosen 1 and 75 mm/day because the former is the lower limit reported by CPC and the latter is the highest value that allows a non-zero persistence measure for all models. In general,

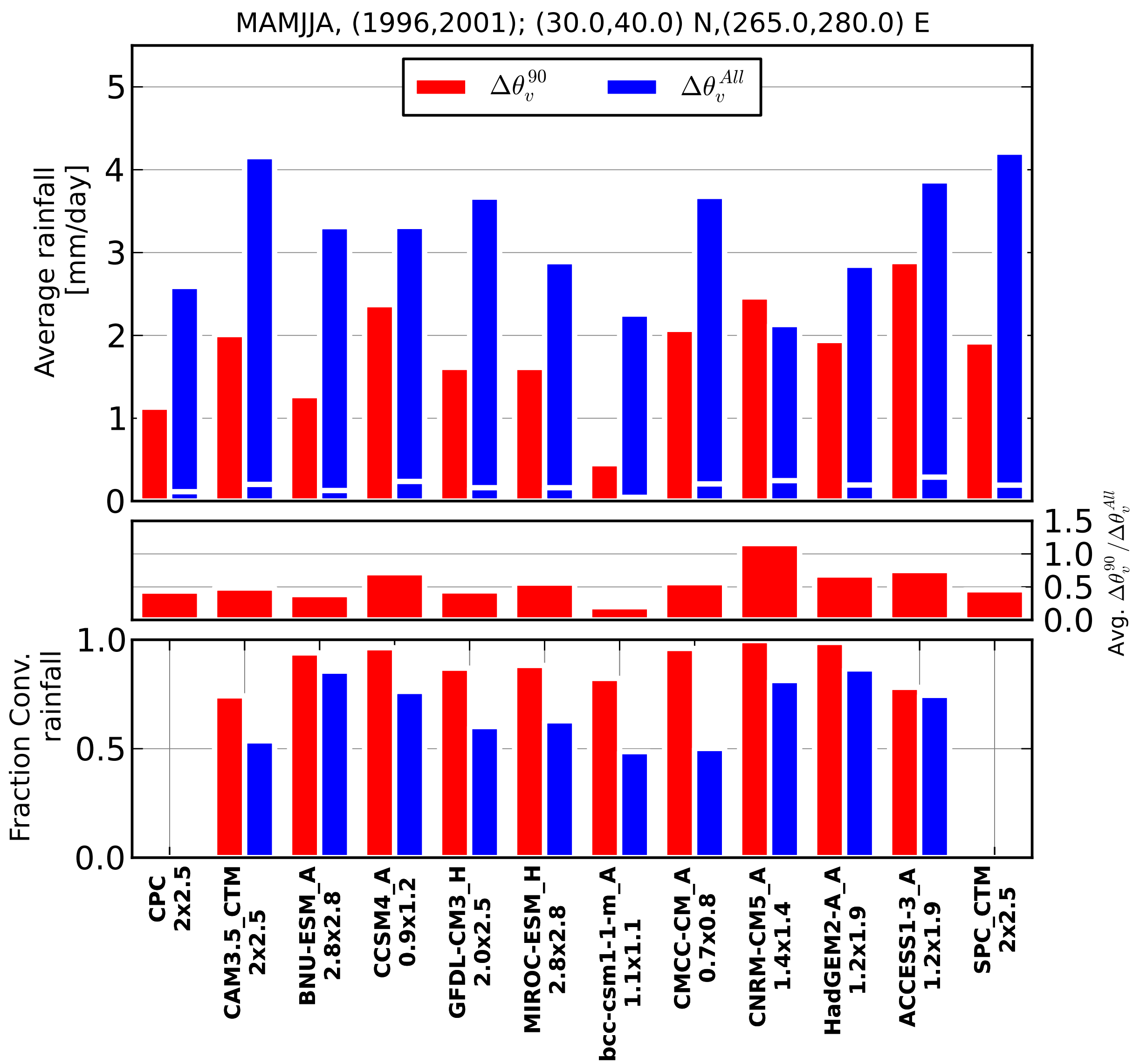

Figure 5.2: Observationally derived and simulated average rainfall for $\Delta\theta_v^{90}$ and $\Delta\theta_v^{All}$ (top); ratio between average rainfall for $\Delta\theta_v^{90}$ and $\Delta\theta_v^{All}$ (middle); and fraction of convective precipitation (not available for CPC and SPC_CTM) for $\Delta\theta_v^{90}$ and $\Delta\theta_v^{All}$ (bottom). Data for latitudes 30 to 40 $^\circ N$ and longitudes 265 to 280 $^\circ E$, from May to August, 1996 to 2001. The nick in the top panel for $\Delta\theta_v^{All}$ shows the contribution from $\Delta\theta_v^{90}$.

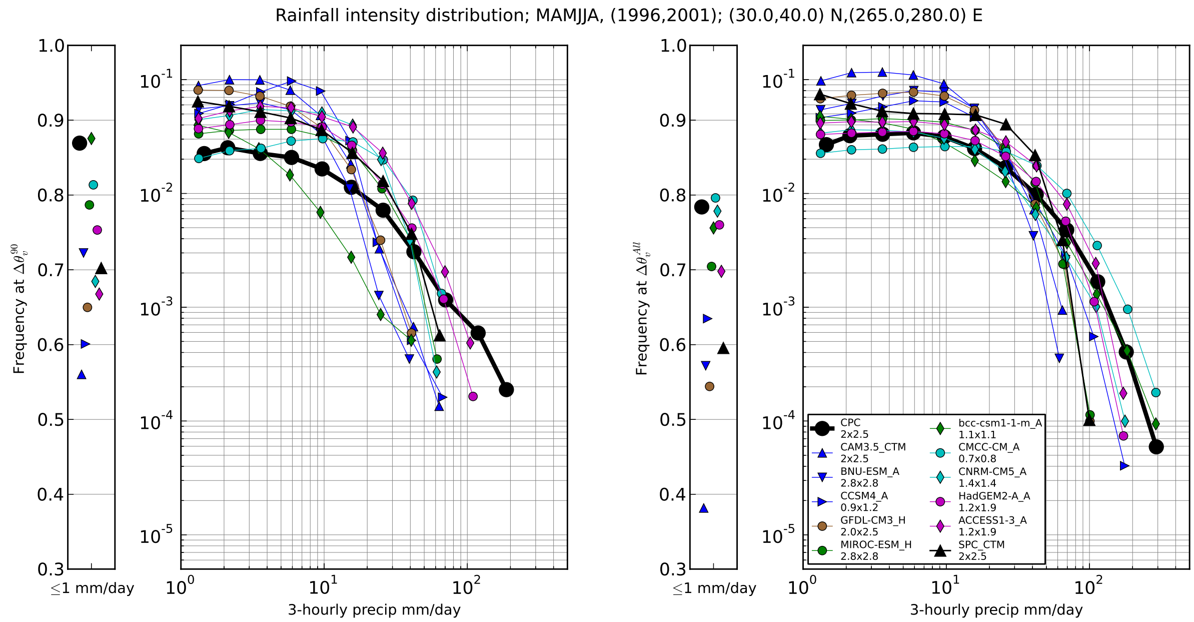

Figure 5.3: Observationally derived and simulated 3-hourly rainfall intensity frequency for $\Delta\theta_v^{90}$ (left) and $\Delta\theta_v^{All}$ (right). This values are calculated from data for latitudes 30 to 40 $^\circ N$ and longitudes 265 to 280 $^\circ E$, from May to August, 1996 to 2001.

the persistence of heavy(light) rainfall is over(under)-estimated by simulations (Fig. 5.4). SPC_CTM heavy rainfall persistence compares better than the other simulations to CPC, whereas light rainfall persistence is estimated accurately in several simulations – bcc-csm1-1-m_A, CMCC-CM_A, CNRM-CM5_A, and HadGEM2-A_A. The greatest differences among GCMs occur for a persistence of little rainfall of 3.5 days.

5.3 Discussion

Different surface energy balances and moisture convergences for the case study region could partly explain the differences in average rainfall among datasets. However, this will not be discussed and assumed not to have implications for the discussion of the diurnal cycle, intensity distribution, and persistence of rainfall.

We have shown that the frequency of GCMs sub-daily rainfall estimates are not conservative with respect to potentially harmful extreme events. Moreover, these estimates become less reliable in conditions that are, in principle, more conducive to CC. Therefore, despite the fact that many processes contribute to rainfall estimates in GCMs, we discuss our findings in relation to the key assumptions present in the CC parameterizations vertical mass flux closures of the GCMs we surveyed, as rainfall rates ultimately depend on the amount of humidity exceeding saturation in the vertical flux of atmospheric air.

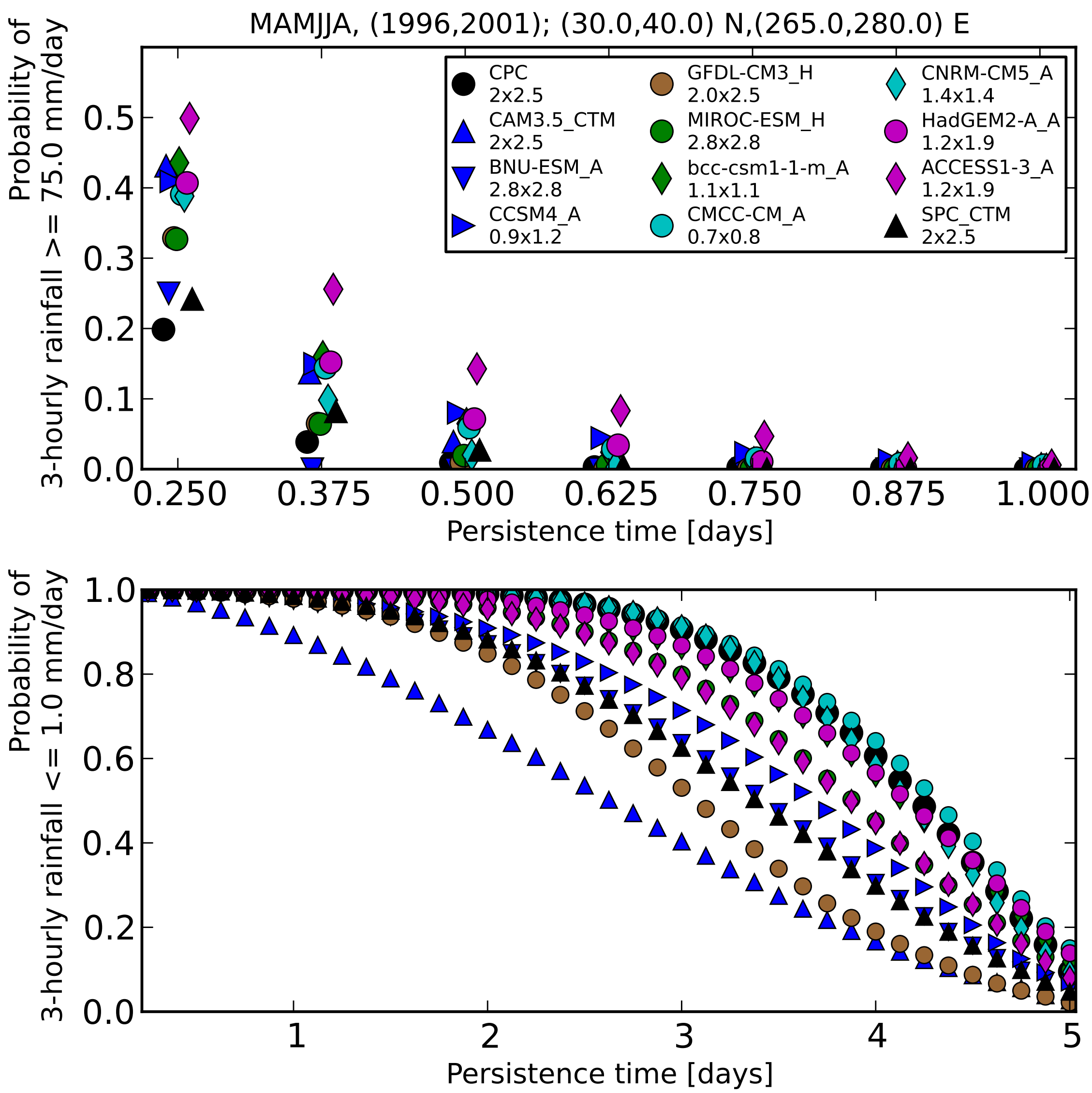

Figure 5.4: Observationally derived and simulated rainfall persistence calculated from data data for latitudes 30 to 40 $^{\circ}N$ and longitudes 265 to 280 $^{\circ}E$, from May to August, 1996 to 2001. Persistence of heavy(light) rainfall is estimated here as the ratio between cases with multiple recurrences of 3-hourly rainfall $\geq$ 75 ($\leq$ 1) mm/day within 1(5) day and total cases of 3-hourly rainfall $\geq$ 75 ($\leq$ 1) mm/day per atmospheric column.

GCMs with mass flux closures based on CAPE consumption at fixed time scales with no suppression mechanisms – CAM3.5_CTM, BNU-ESM_A, CCSM4_A, GFDL-CM3_H (Table 5.1) – have the largest bias in that they greatly overestimate middle intensity rainfall and underestimate light and heavy rainfall (Fig. 5.3). Among these GCMs, CCSM4_A and GFDL-CM3_H have smaller biases. This may be due to using an *entraining plume* formulation for CAPE for CCSM4_A and to setting a CAPE relaxation target of 1000 j/Kg (10 to 20% of the severe to most severe weather events) for GFDL-CM3_H. Both approaches should, on average, favor accumulation of convective instability, hence reducing the incidence of middle rainfall events and increasing the incidence of no, little, and heavy rainfall events. GCMs with mass flux closures based on CAPE consumption at fixed time scales and suppression mechanisms based on relative humidity (RH) thresholds – MIROC-ESM_H and bcc-csm1-1-m_A – or with a resolution dependent CAPE consumption time scale and a suppression mechanism allowing CC only in case of positive low level moisture convergence – CMCC-CM_A – have overall smaller biases. Similarly, CNRM-CM5_A which utilizes a mass flux closure based on the difference between in-cloud and environmental moist static energy, and requires positive environmental low level moisture convergence, has a smaller bias compared to GCMs with no suppression mechanism. HadGEM2-A_A's mass flux closure is calculated from an empirical formula for the excess buoyancy of the cloud against the environment and includes a threshold value. This model also has a smaller bias than CAPE based GCMs with no suppression mechanisms. Our general conclusion is that sub-daily rainfall frequency intensity is better estimated by GCMs with suppression mechanisms or threshold values that prevent CC from responding too rapidly to atmospheric instability.

The GCM with explicit cloud treatment – SPC_CTM – can simulate the diurnal cycle of average rainfall better that the other GCMs (Fig. 5.1, top). This has already been shown in a similar case study and attributed to its ability to simulate the energy transfer from the surface to CC at a slower, more realistic, rate [20]. Nonetheless, SPC_CTM does not capture the weakening of the diurnal cycle observed for CPC from moving from the southern to the northern region of our case study. Instead, SPC_CTM is qualitatively similar to the other GCMs, though to a smaller degree, that is, SPC_CTM is too responsive to local instability (Fig. 5.1, bottom). This is also supported by the fact that SPC_CTM overestimates middle intensity rainfall and underestimates little and heavy rainfall (Fig. 5.3). From the reanalysis data we estimate a difference of about 1 m/s for the 850 hPa horizontal wind, from 7 m/s for the southern region to 8 m/s for the northern region. Surface level and 850 hPa relative humidities look similar between regions. Vertical wind shear is thought to have an effect on the organization of CC, hence the difference we estimate could be a reason for the different diurnal cycles. Nonetheless, SPC_CTM , which in principle should allow a more realistic simulation of cloud organization, fails to replicate a flatter diurnal cycle in the northern region. One possible cause of this bias may be related to the two dimensional character of the cloud resolving model (CRM) embedded in SPC_CTM. Two dimensional CMRs entrain less environmental air than three dimensional CRMs and they are more likely to develop convective updrafts [94], which might override possible inhibiting factors including vertical wind shear.

From the analysis of the heavy rainfall persistence we have not found a particular clustering of model behaviors that can be attributed to their CC closures. In general, the GCMs analyzed here overestimate the persistence of heavy rainfall (Fig. 5.4, top). Recalling that rainfall heavier than the heavy rainfall persistence threshold (75 mm/day) occurs less frequently in GCMs (Fig. 5.3) suggests the following speculation: locally, GCM CC does not consume atmospheric instability as fast as the real atmosphere does and GCMs create the conditions for heavy but not extreme rainfall too often. The implications for regional landslide and flood risk estimates may be important because in some locations the surge in rainfall water that impinges on the ground may be underestimated and in others the total amount of rainfall water within, for instance, a day may be overestimated.

The persistence of little rainfall is best estimated by GCMs with suppression mechanisms, however, in general, GCMs underestimate the persistence of light rainfall (Fig. 5.4, bottom). For some regions, this could mean underestimating the risk of drought for farming and natural ecosystems and should be a reason for concern.

From satellite remote sensing data it is possible to estimate instantaneous values of rainfall and some related atmospheric field including the partitioning between convective and stratiform rainfall. We hope that public GCMs archives will provide corresponding simulated data and diagnostics emulating satellite retrievals at high time resolution.

Chapter 6

Monsoon precipitation and anthropogenic aerosols

In this chapter we present a research plan for the study of the interaction between monsoon precipitation and anthropogenic aerosols.

6.1 Introduction

Monsoon precipitation has a seasonal character and occurs within the tropics. It is of critical importance for a very large portion of the world's population. Monsoon precipitation displays trends which vary between the northern and the southern hemispheres: although global ocean and land monsoon precipitation has increased, northern hemisphere monsoon land precipitation has decreased [126]. Observed and projected global warming should increase monsoon precipitation because of higher moisture content in the lower atmospheric levels converging on virtually unchanged monsoon area [61], but, at the regional scale, observed trends are more uncertain because of the effect of anthropogenic aerosols on precipitation processes [48].

Here we design and experiment for the Indian monsoon precipitation using the multiscale modeling framework because the full characterization of this process is important for societal reasons and because it offers novel scientific challenges in the field of climate. This monsoon occurs on a large and densely populated area where most of the world's rice is grown following to the timing of monsoon rainfall. As expected, the economy of rice is sensitive to changes on monsoon rainfall [5].

Rainfall trends for the Indian monsoon seem to be caused by anthropogenic aerosols [14, 7]. Different mechanisms have been proposed for the overall trends [95, 65] and for the asymmetry of the trends [32] but our understanding is still in a beginning stage. Moreover, projected changes in extreme rainfall for the monsoon precipitation are larger than projected average rainfall changes and this feature is stronger for the Indian monsoon than for other monsoons [61].

We believe that the multiscale modeling framework is the appropriate tool to further understanding of the Indian monsoon because of the its ability to simulate better than other models the intraseasonal atmospheric variability of the region [53], because it can resolve global climate model sub-grid processes thought to be relevant for monsoon dynamics [48], and because it improves the fidelity of extreme precipitation (Chapters 4 and 5).

Prior investigations using the multiscale modeling framework for the Indian monsoon discussed the possibility that biases in the variability of the monsoon precipitation could derive from unrealistic vertical heating from the cloud resolving model which produces more baroclinicity than what is observed in the reanalysis [35, 21]. However, the effects of black carbon and sulfate anthropogenic aerosols on the dynamics of the cloud resolving model embedded in the multiscale modeling framework has never been analyzed.

6.2 Experimental design

We will run numerical experiments with the multiscale climate model (SPC) and the conventional climate model (CAM) coupled to slab ocean model, and with prescribed 2003 to 2012 MERRA assimilated aerosol concentrations by NASA[1]. In two simulations (SPC-MERRA-PD and CAM-MERRA-PD) we will use assimilated black carbon and sulfate aerosols to emulated present time condition, whereas in two simulations (SPC-MERRA-PI and CAM-MERRA-PI) we will set black carbon and sulfate aerosols to negligible values to emulated pre-industrial conditions. The main differences between our simulations and prior work from Goswami et al. [35], DeMott, Stan, and Randall [21] with the multiscale modeling framework are the use of assimilated present day aerosol concentration instead of aerosol emissions and the use of a slab ocean model instead of a full ocean model. The different prescribed aerosol forcings optical depths for the pre-monsoonal stage are shown in figures 6.1, 6.2, and 6.3. Because there are considerable differences among the aerosol forcing we will prescribe and the forcing used in prior studies we are confident that our experiments are original. On the one hand, we expect effects on the pre-monsoon rainfall from fast atmospheric physical processes related to changes in convective stability which is typically increased by the presence of absorbing and scattering aerosols. This occurs because these compounds absorb and reflect sunlight in the lower atmospheric levels which causes surface cooling and atmospheric heating. On the other hand, we also expect effects on monsoon rainfall from slow physical processes. Pre-monsoon sea surface cooling by absorbing and scattering aerosols can last into the monsoon period and reduce monsoon moisture convergence.

Contrasting our results from SPC-MERRA-PD to Goswami et al. [35], DeMott, Stan, and Randall [21] will show the effects of realistic anthropogenic aerosols in the multiscale modeling framework for the Indian monsoon. Contrasting SPC-MERRA-PD and SPC-MERRA-PI to observationally derived data for the Indian monsoon will show the possible biases in

[1]Modern-Era Retrospective Analysis For Research And Applications. Data provided by Dr. Arlindo M. da Silva, Jr., NASA/Goddard Space Flight Center, Global Modeling and Assimilation Office, Greenbelt, MD 20771

Indian monsoon precipitation trends from these simulations. Contrasting SPC and CAM simulations will highlight the differences between model responses to realistic aerosol forcing from the different treatments of cloud processes.

Interestingly, during the wet monsoon season which occurs in boreal summer the greater aerosol forcing is to the west of India and the difference between the prescribed aerosol forcing is less than for the pre-monsoonal season (not shown). Nonetheless, the meridional near surface wind which is important for moisture transport toward the Indian region is larger for smaller aerosol loadings (Figure 6.4). These results are from very short simulations for a few years of climate with prescribed sea surface temperature, hence they only provide hints on the possible causes of reduced monsoon strength.

Next, we will run numerical experiments using prescribed aerosol emission and explicit transport for black carbon and sulfate aerosols with the multiscale modeling framework (SPC-TRAERO-PD) and with the conventional model (CAM-TRAERO-PD). For the region of the Indian monsoon, the transport of a short-lived surface-emitted tracer differs between the conventional and the multiscale models. In figure 6.5 and 6.6 we show the percentage differences between radon concentration (Chapter 2) for the month of January and July, respectively. For the winter(summer) month, the multiscale model estimates higher(lower) concentrations in the layer between 1500 and 2500 m on the Indian ocean. These experiments will highlight the role of the discrepancies between assimilated and explicitly transported aerosols and their implications for precipitation processes.

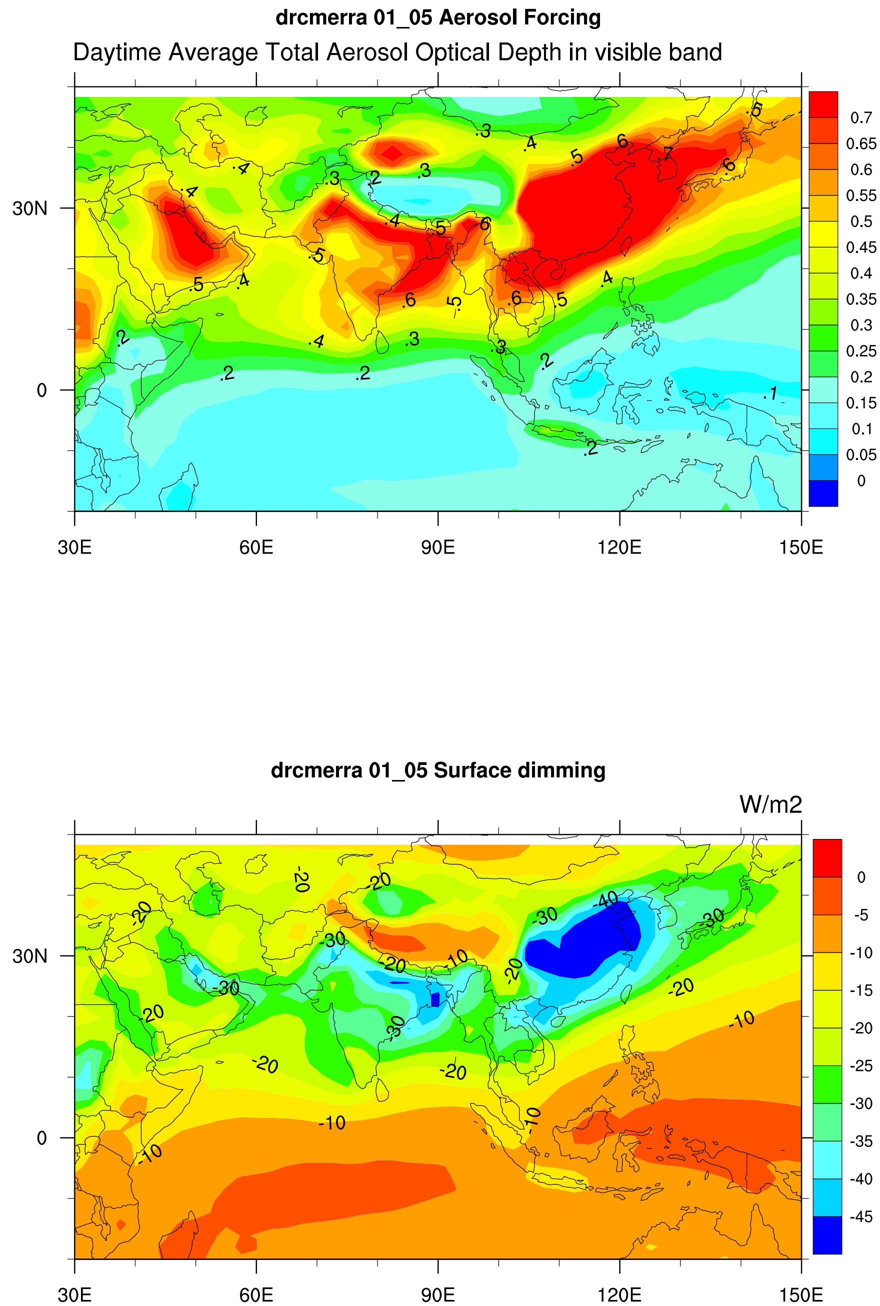

Figure 6.1: January to May MERRA's aerosol optical depth (top) and surface dimming (bottom).

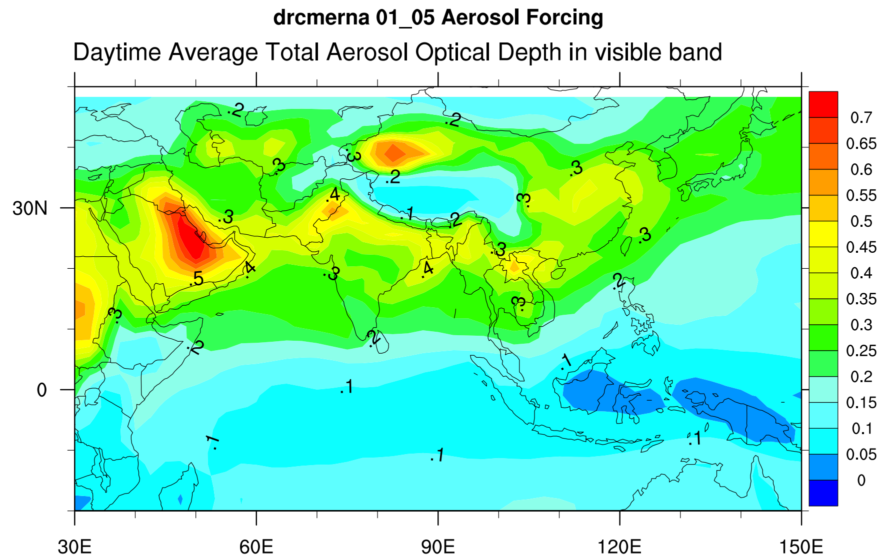

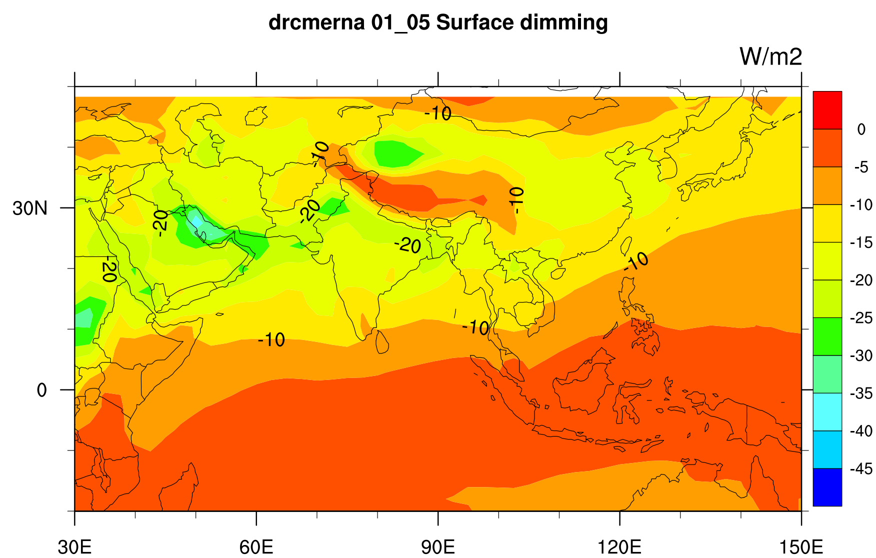

Figure 6.2: January to May MERNA's aerosol optical depth (top) and surface dimming (bottom) when black carbon and sulfate aerosols are set to zero.

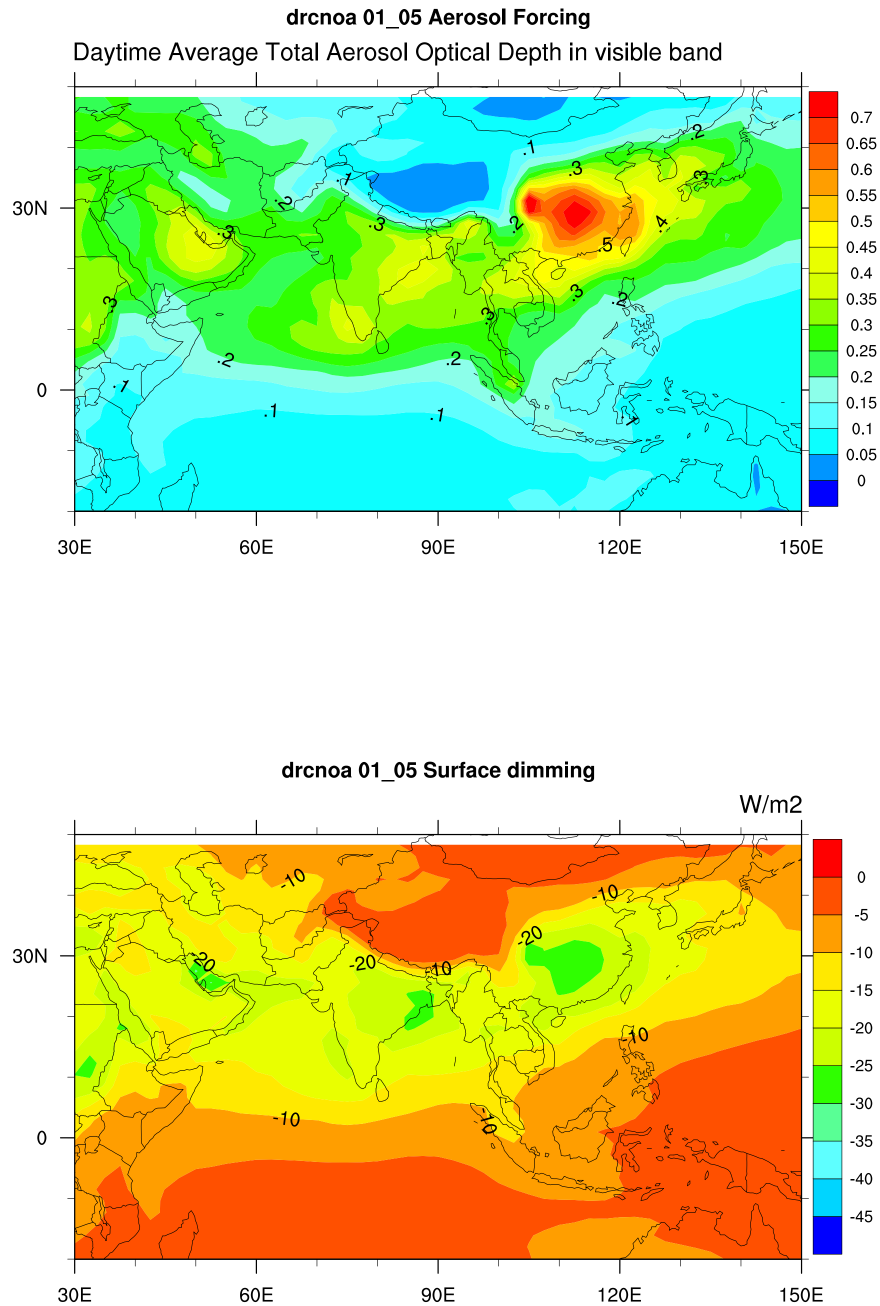

Figure 6.3: January to May aerosol optical depth (top) and surface dimming (bottom) as in Goswami et al. [35], DeMott, Stan, and Randall [21].

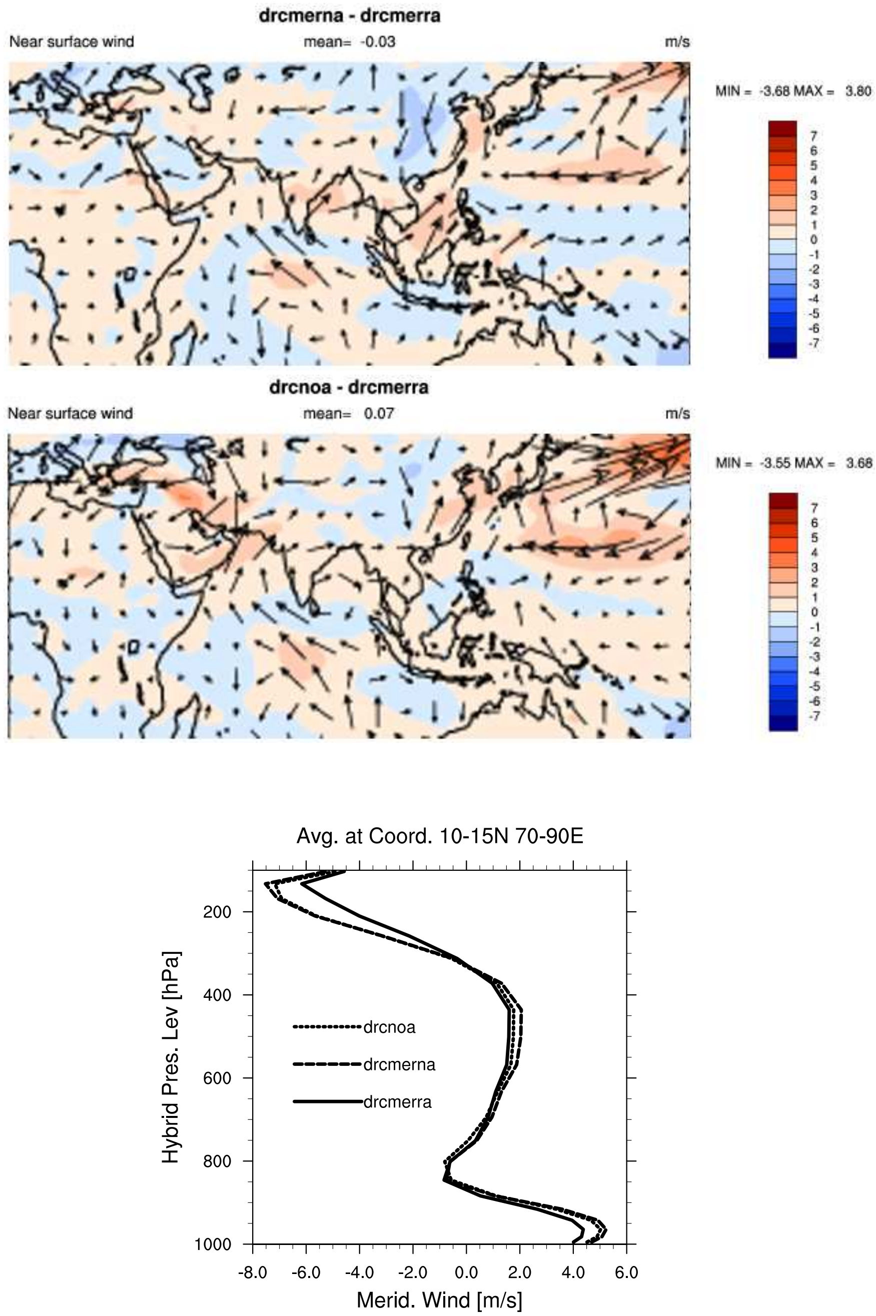

Figure 6.4: June to August near surface wind anomaly from simulations with MERRA aerosols excluding black carbon and sulfate (drcmerna) and MERRA total aerosols (drcmerra) on the top panel, and from simulations with aerosol loading as in Goswami et al. [35], DeMott, Stan, and Randall [21] (drcnoa) and MERRA total aerosols on the middle panel. Average meridional winds over central India from drcmerra, drcmerna, and drcnoa. These results are from very short simulations for a few years of climate with prescribed sea surface temperature.

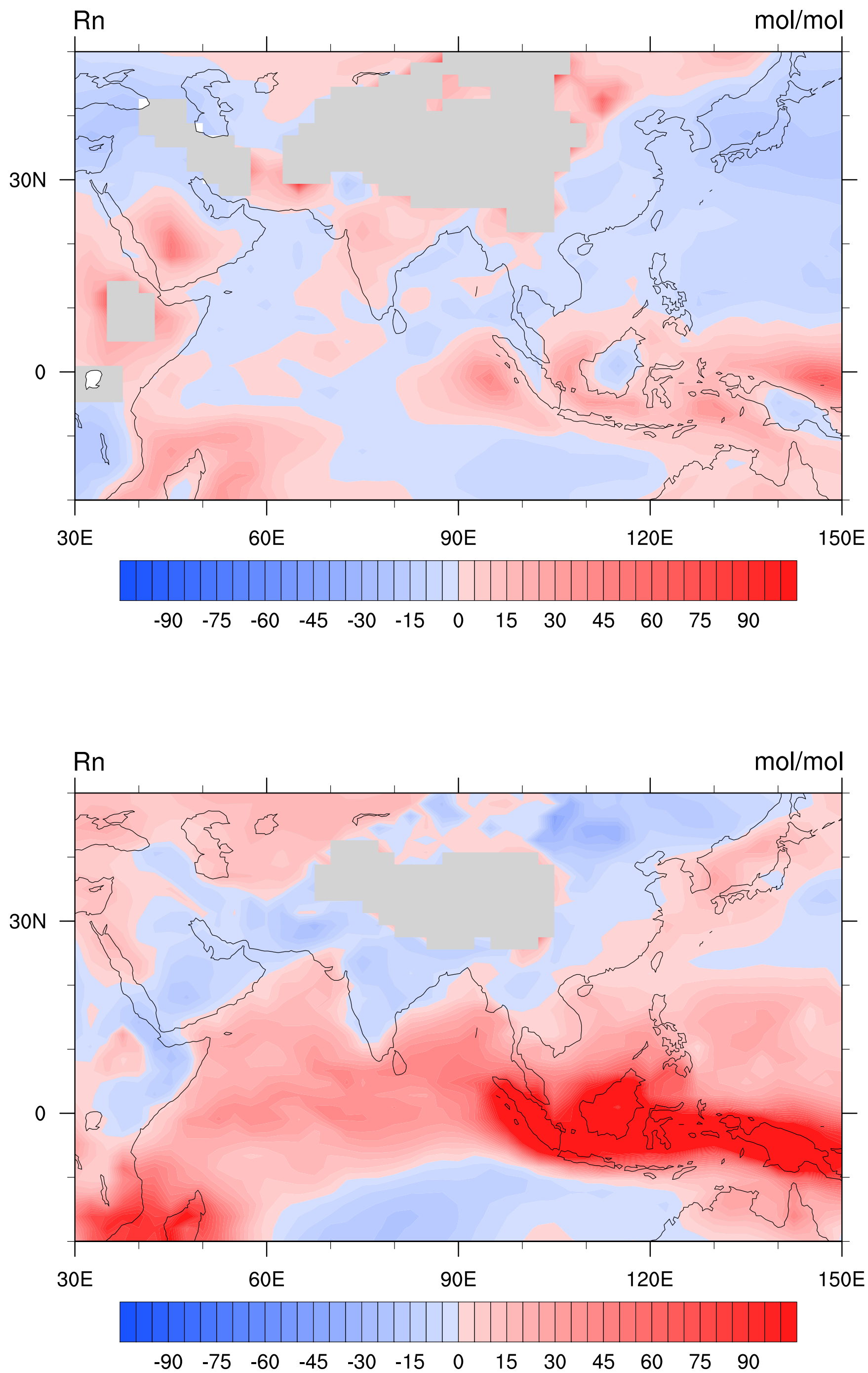

Figure 6.5: Radon volume mixing ratio % differences for 0 to 1500 m (top) and for 1500 to 2500 m (bottom) between the multiscale and the conventional climate model for the month of January (Chapter 2).

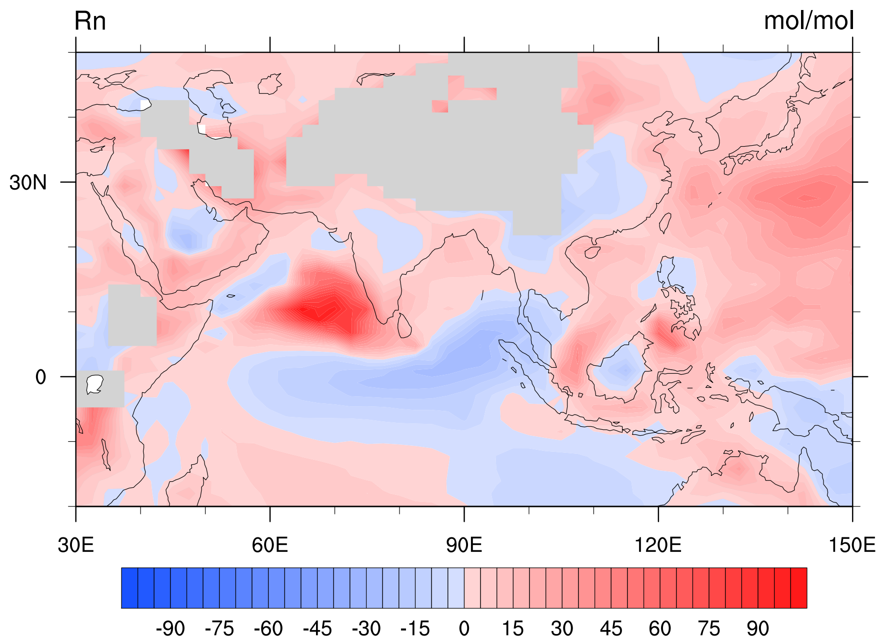

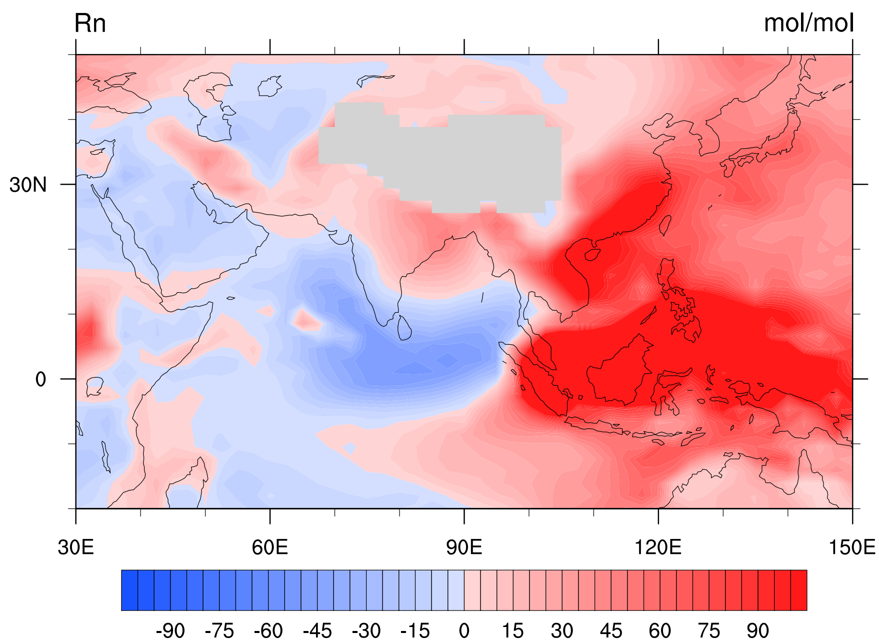

Figure 6.6: Radon volume mixing ratio % differences for 0 to 1500 m (top) and for 1500 to 2500 m (button) between the multiscale and the conventional climate model for the month of July (Chapter 2).

Bibliography

[1] B. A. Albrecht. "Aerosols, cloud microphysics, and fractional cloudiness". In: *Science* 245 (1989), pp. 1227–1230.

[2] L. V. Alexander et al. "Global observed changes in daily climate extremes of temperature and precipitation". In: *Journal Of Geophysical Research-Atmospheres* 111.D5 (2006). DOI: 10.1029/2005JD006290.

[3] A. Arakawa. "The Cumulus Parameterization Problem: Past, Present, and Future". In: *Journal Of Climate* 17.13 (2004), pp. 2493–2525.

[4] D. Archer et al. "What caused the glacial/interglacial atmospheric pCO2 cycles?" In: *Rev. Geophys.* 38 (2000), 159189.

[5] M. Auffhammer, V. Ramanathan, and J. R. Vincent. "Integrated model shows that atmospheric brown clouds and greenhouse gases have reduced rice harvests in India". In: *Proceedings Of The National Academy Of Sciences Of The United States Of America* 103.52 (2006), pp. 19668–19672. DOI: 10.1073/pnas.0609584104.

[6] N. Bell et al. "Methyl Iodide: Atmospheric Budget and Use As A Tracer Of Marine Convection In Global Models". In: *Journal Of Geophysical Research-Atmospheres* 107.D17 (2002).

[7] Massimo A. Bollasina, Yi Ming, and V. Ramaswamy. "Anthropogenic Aerosols and the Weakening of the South Asian Summer Monsoon". In: *Science* 334.6055 (2011), pp. 502–505. ISSN: 0036-8075. DOI: 10.1126/science.1204994.

[8] R. D. Borys et al. "Mountaintop and radar measurements of anthropogenic aerosol effects on snow growth and snowfall rate". In: *Geophys. Res. Lett.* 30, NO. 10, 1538 (2003), doi:10.1029/2002GL016855.

[9] B. A. Boville and C. S. Bretherton. "Heating and kinetic energy dissipation in the NCAR Community Atmosphere Model". In: *Journal Of Climate* 16.23 (2003), pp. 3877–3887. ISSN: 0894-8755.

[10] J. Boyle and S. A. Klein. "Impact of horizontal resolution on climate model forecasts of tropical precipitation and diabatic heating for the TWP-ICE period". In: *Journal Of Geophysical Research-Atmospheres* 115 (2010). DOI: 10.1029/2010JD014262.

[11] O. A. Chadwick et al. "Changing sources of nutrients during four million years of ecosystem development". In: *Nature* 397 (2000), 491497.

[12] J. P. Charba, A. W. Harrell III, and A. C. Lackner III. *A monthly precipitation amount climatology derived from published atlas maps: Development of a digital data base.* Tech. rep. Washington, D. C, 1992.

[13] C. T. Chen and T. Knutson. "On the verification and comparison of extreme rainfall indices from climate models". In: *Journal Of Climate* 21.7 (2008), pp. 1605–1621. DOI: `10.1175/2007JCLI1494.1`.

[14] CE Chung and V Ramanathan. "Weakening of North Indian SST gradients and the monsoon rainfall in India and the Sahel". In: *Journal Of Climate* 19.10 (2006), pp. 2036–2045. ISSN: 0894-8755. DOI: `10.1175/JCLI3820.1`.

[15] W. D. Collins et al. "Simulating aerosols using a chemical transport model with assimilation of satellite aerosol retrievals: Methodology for INDOEX". In: *J. Geophys. Res.* 106, No. D7 (2001), 73137336.

[16] W. D. Collins et al. "The formulation and atmospheric simulation of the Community Atmosphere Model version 3 (CAM3)". English. In: *Journal Of Climate* 19.11 (2006), pp. 2144–2161. ISSN: 0894-8755.

[17] W.D. Collins et al. *Description of the NCAR Community Atmosphere Model (CAM 3.0), NCAR/TN464+STR, NCAR TECHNICAL NOTE*. Tech. rep. National Center For Atmospheric Research, Boulder, CO, USA: NCAR, 2004. URL: `http://www.cesm.ucar.edu/models/atm-cam/docs/description/description.pdf`.

[18] G. P. Cressman. "An Operational Objective Analysis System". In: *Monthly Weather Review* (1959), pp. 367–374.

[19] Aiguo Dai. "Precipitation characteristics in eighteen coupled climate models". English. In: *Journal Of Climate* 19.18 (2006), pp. 4605–4630. ISSN: 0894-8755. DOI: `10.1175/JCLI3884.1`.

[20] Charlotte A. Demott, D. A. Randall, and M. Khairoutdinov. "Convective precipitation variability as a tool for general circulation model analysis". English. In: *Journal Of Climate* 20.1 (2007), pp. 91–112. ISSN: 0894-8755. DOI: `10.1175/JCLI3991.1`.

[21] Charlotte A. DeMott, Cristiana Stan, and David A. Randall. "Northward Propagation Mechanisms of the Boreal Summer Intraseasonal Oscillation in the ERA-Interim and SP-CCSM". In: *Journal Of Climate* 26.6 (2013), pp. 1973–1992. ISSN: 0894-8755. DOI: `10.1175/JCLI-D-12-00191.1`.

[22] P. J. DeMott et al. "Predicting global atmospheric ice nuclei distributions and their impacts on climate". In: *Proceedings Of The National Academy Of Sciences Of The United States Of America* 107.25 (2010), pp. 11217–11222. ISSN: 0027-8424. DOI: `10.1073/pnas.0910818107`.

[23] L. J. Donner et al. "Transport Of Radon-222 and Methyl Iodide By Deep Convection In The GFDL Global Atmospheric Model AM2". In: *Journal Of Geophysical Research-Atmospheres* 112.D17 (2007), p. 18.

[24] Leo J. Donner et al. "The Dynamical Core, Physical Parameterizations, and Basic Simulation Characteristics of the Atmospheric Component AM3 of the GFDL Global Coupled Model CM3". English. In: *Journal Of Climate* 24.13 (2011), pp. 3484–3519. ISSN: 0894-8755. DOI: 10.1175/2011JCLI3955.1.

[25] C. F. Durman et al. "A comparison of extreme European daily precipitation simulated by a global and a regional climate model for present and future climates". In: *Quarterly Journal Of The Royal Meteorological Society* 127.573 (2001), pp. 1005–1015. DOI: 10.1002/qj.49712757316.

[26] L. K. Emmons et al. "Description and evaluation of the Model for Ozone and Related chemical Tracers, version 4 (MOZART-4)". In: *Geoscientific Model Development* 3.1 (2010), pp. 43–67. ISSN: 1991-959X.

[27] R.J. Ferek et al. "Drizzle suppression in ship tracks". In: *J. Aerosol Sci.* 57 (2000), pp. 2707–2728.

[28] Christopher B Field et al. *Managing the risks of extreme events and disasters to advance climate change adaptation. Special report of the Intergovernmental Panel on Climate Change.* 2012.

[29] I. Folkins et al. "Testing Convective Parameterizations With Tropical Measurements Of HNO3, CO, H2O, and O3: Implications For The Water Vapor Budget". In: *Journal Of Geophysical Research-Atmospheres* 111.D23 (2006). Folkins, Ian Bernath, P. Boone, C. Donner, L. J. Eldering, A. Lesins, Glen Martin, R. V. Sinnhuber, B. -M. Walker, K.

[30] P. Forster et al. "Changes in atmospheric constituents and in radiative forcing". In: *Climate change* 30 (2007).

[31] P. Frich et al. "Observed coherent changes in climatic extremes during the second half of the twentieth century". In: *Climate Research* 19.3 (2002), pp. 193–212. DOI: 10.3354/cr019193.

[32] Dilip Ganguly et al. "Fast and slow responses of the South Asian monsoon system to anthropogenic aerosols". In: *Geophysical Research Letters* 39 (2012). ISSN: 0094-8276. DOI: 10.1029/2012GL053043.

[33] Peter R. Gent et al. "The Community Climate System Model Version 4". English. In: *Journal Of Climate* 24.19 (2011), pp. 4973–4991. ISSN: 0894-8755. DOI: 10.1175/2011JCLI4083.1.

[34] P. Ginoux et al. "Sources and distributions of dust aerosols simulated with the GOCART model". In: *J. Geophys. Res.* 106(D17) (2001), pp. 20,255–20,273.

[35] Bidyut B. Goswami et al. "Simulation of Indian summer monsoon intraseasonal oscillations in a superparameterized coupled climate model: need to improve the embedded cloud resolving model". In: *Climate Dynamics* 41.5-6 (2013), pp. 1497–1507. ISSN: 0930-7575. DOI: 10.1007/s00382-012-1563-1.

[36] W. W. Grabowski. "Coupling cloud processes with the large-scale dynamics using the Cloud- Resolving Convection Parameterization (CRCP)". In: *J. Atmos. Sci.* 58 (2001), 978997.

[37] James J. Hack. "Parameterization of moist convection in the National Center for Atmospheric Research Community Climate Model (CCM2)". English. In: *Journal Of Geophysical Research-Atmospheres* 99.D3 (1994), pp. 5551–5568. ISSN: 0148-0227.

[38] S. Van den Heever and W.R. Cotton. "Urban aerosol impacts on downwind convective storms". In: *J. Appl. Meteorol.* 46 (2007), pp. 828–850.

[39] A. Heymsfield and G. McFarquhar. "Microphysics of INDOEX clean and polluted trade cumulus clouds". In: *J. Geophys. Res.* 106(D22) (2001), doi: 10.1029/2000JD900776.

[40] R. W. Higgins, V. E. Kousky, and P. Xie. "Extreme Precipitation Events in the South-Central United States during May and June 2010: Historical Perspective, Role of ENSO, and Trends". English. In: *Journal Of Hydrometeorology* 12.5 (2011), pp. 1056–1070. ISSN: 1525-755X. DOI: 10.1175/JHM-D-10-05039.1.

[41] R. W. Higgins et al. "Improved United States precipitation quality control system and analysis". In: *NCEP/Climate Prediction Center ATLAS* 7 (2000), p. 40. URL: http://www.cpc.ncep.noaa.gov/research_papers/ncep_cpc_atlas/7/toc.html.

[42] J. M. Hoell et al. "Pacific Exploratory Mission in the tropical Pacific: PEM-Tropics A, August-September 1996". In: *Journal Of Geophysical Research-Atmospheres* 104.D5 (1999), pp. 5567–5583. ISSN: 0747-7309.

[43] C. R. Hoyle et al. "Representation of tropical deep convection in atmospheric models - Part 2: Tracer transport". In: *Atmospheric Chemistry And Physics* 11.15 (2011), pp. 8103–8131.

[44] W. C. Hsieh, D. Rosa, and W. D. Collins. "Global dust simulations in the multiscale modeling framework". In: *Journal Of Advances In Modeling Earth Systems* 5.1 (2013), pp. 15–31. ISSN: 1942-2466. DOI: 10.1029/2012MS000150.

[45] J. G. Hudson and S. S. Yum. "MaritimeContinental Drizzle Contrasts in Small Cumuli". In: *J. Aerosol Sci.* 58 (2001), pp. 915–926.

[46] N. Huneeus et al. "Global dust model intercomparison in AeroCom phase I)". In: *Atmos. Chem. Phys.* 11 (2011), 77817816.

[47] J. P. Iorio et al. "Effects of model resolution and subgrid-scale physics on the simulation of precipitation in the continental United States". In: *Climate Dynamics* 23.3-4 (2004), pp. 243–258. DOI: 10.1007/s00382-004-0440-y.

[48] IPCC. *2013: Climate Phenomena and their Relevance for Future Regional Climate Change. In: Climate Change 2013: The Physical Science Basis. Contribution of Working Group I to the Fifth Assessment Report of the Intergovernmental Panel on Climate Change*. ed. Stocker, T.F., D. Qin, G.-K. Plattner, M. Tignor, S.K. Allen, J. Boschung, A. Nauels, Y. Xia, V. Bex and P.M. Midgley. Cambridge University Press, Cambridge, United Kingdom and New York, NY, USA, 2013.

[49] T. Iversen and O. Seland. "A scheme for process-tagged SO4 and BC aerosols in NCAR CCM3: validation and sensitivity to cloud processes". In: *J. Geophys. Res.* 107, 4751 (2002), doi:10.1029/2001jd000885.

[50] D. J. Jacob et al. "Evaluation and intercomparison of global atmospheric transport models using Rn-222 and other short-lived tracers". In: *Journal Of Geophysical Research-Atmospheres* 102.D5 (1997), pp. 5953–5970.

[51] D. J. Jacob et al. "The Arctic Research of the Composition of the Troposphere from Aircraft and Satellites (ARCTAS) mission: design, execution, and first results". In: *Atmospheric Chemistry And Physics* 10.11 (2010), pp. 5191–5212.

[52] D. J. Jacob et al. "Transport and Chemical Evolution over the Pacific (TRACE-P) aircraft mission: Design, execution, and first results". In: *Journal Of Geophysical Research-Atmospheres* 108.D20 (2003), pp. 1–19.

[53] XN Jiang, T Li, and B Wang. "Structures and mechanisms of the northward propagating boreal summer intraseasonal oscillation". In: *Journal Of Climate* 17.5 (2004), pp. 1022–1039. ISSN: 0894-8755. DOI: `10.1175/1520-0442(2004)017<1022:SAMOTN>2.0.CO;2`.

[54] C. Jones, N. Mahowald, and C. Luo. "Observational evidence of African desert dust intensification of easterly waves". In: *Geophysical Research Letters* 31.17 (2004). ISSN: 0094-8276. DOI: `10.1029/2004GL020107`.

[55] E Kalnay et al. "The NCEP/NCAR 40-year reanalysis project". In: *Bulletin Of The American Meteorological Society* 77.3 (1996), pp. 437–471.

[56] Y. J. Kaufman et al. "Dust transport and deposition observed from the Terra-Moderate Resolution Imaging Spectroradiometer (MODIS) spacecraft over the Atlantic ocean". In: *journal of geophysical research-atmospheres* 110.D10 (2005). ISSN: 2169-897X. DOI: `10.1029/2003JD004436`.

[57] M. F. Khairoutdinov, C. DeMott, and D. A. Randall. "Evaluation of the simulated interannual and subseasonal variability in an AMIP-Style simulation using the CSU multiscale modeling framework". In: *Journal of Climate* 21.3 (2008), pp. 413–431.

[58] M. F. Khairoutdinov and D. A. Randall. "A cloud resolving model as a cloud parameterization in the NCAR Community Climate System Model: Preliminary results". In: *Geophysical Research Letters* 28.18 (2001), pp. 3617–3620.

[59] M. F. Khairoutdinov and D. A. Randall. “Cloud resolving modeling of the ARM summer 1997 IOP: Model formulation, results, uncertainties, and sensitivities”. In: *Journal Of The Atmospheric Sciences* 60.4 (2003), pp. 607–625. ISSN: 0022-4928.

[60] M. F. Khairoutdinov, D. A. Randall, and C. Demott. “Simulations Of The Atmospheric General Circulation Using A Cloud-Resolving Model As A Superparameterization Of Physical Processes”. In: *Journal Of The Atmospheric Sciences* 62.7 (2005). Part 1, pp. 2136–2154.

[61] Akio Kitoh et al. “Monsoons in a changing world: A regional perspective in a global context”. In: *Journal Of Geophysical Research-Atmospheres* 118.8 (2013), pp. 3053–3065. ISSN: 2169-897X. DOI: 10.1002/jgrd.50258.

[62] I. Koren et al. “Aerosol invigoration and restructuring of Atlantic convective clouds”. In: *Geophysical Research Letters* 32.14 (2005). ISSN: 0094-8276. DOI: 10.1029/2005GL023187.

[63] M. A. Kritz, S. W. Rosner, and D. Z. Stockwell. “Validation Of An Off-Line Three-Dimensional Chemical Transport Model Using Observed Radon Profiles - 1. Observations”. In: *Journal Of Geophysical Research-Atmospheres* 103.D7 (1998), pp. 8425–8432.

[64] J.-F. Lamarque et al. “CAM-chem: description and evaluation of interactive atmospheric chemistry in CESM”. In: *Geoscientific Model Development Discussions* 4.3 (2011), pp. 2199–2278. URL: http://www.geosci-model-dev-discuss.net/4/2199/2011/.

[65] KM Lau, MK Kim, and KM Kim. “Asian summer monsoon anomalies induced by aerosol direct forcing: the role of the Tibetan Plateau”. In: *Climate Dynamics* 26.7-8 (2006), pp. 855–864. ISSN: 0930-7575. DOI: 10.1007/s00382-006-0114-z.

[66] Y. H. Lee, K. Chen, and P. J. Adams. “Development of a global model of mineral dust aerosol microphysics”. In: *Atmos. Chem. Phys.* 9 (2009), 24412458.

[67] M. A. Lemone and E. J. Zipser. “Cumulonimbus Vertical Velocity Events In Gate .1. Diameter, Intensity and Mass Flux”. In: *Journal Of The Atmospheric Sciences* 37.11 (1980), pp. 2444–2457.

[68] Z. Levin, E. Ganor, and V. Gladstein. “The effects of desert particles coated with sulfate on rain formation in the eastern Mediterranean”. In: *Journal Of Applied Meteorology* 35.9 (1996). 6th World-Meteorological-Organization Scientific Conference on Weather Modification, Paestum, Italy, May-Jun -, 1994, pp. 1511–1523. ISSN: 0894-8763. DOI: 10.1175/1520-0450(1996)035<1511:TEODPC>2.0.CO;2.

[69] F. Li, P. Ginoux, and V. Ramaswamy. “Distribution, transport, and deposition of mineral dust in the Southern Ocean and Antarctica: Contribution of major sources”. In: *J. Geophys. Res.* 113, D10207 (2008), doi:10.1029/2007JD009190.

[70] F. Li et al. "Impact of horizontal resolution on simulation of precipitation extremes in an aqua-planet version of Community Atmospheric Model (CAM3)". In: *Tellus Series A-Dynamic Meteorology And Oceanography* 63.5 (2011), pp. 884–892. DOI: 10.1111/j.1600-0870.2011.00544.x.

[71] F. Li et al. "Response of precipitation extremes to idealized global warming in an aqua-planet climate model: towards a robust projection across different horizontal resolutions". In: *Tellus Series A-Dynamic Meteorology And Oceanography* 63.5 (2011), pp. 876–883. DOI: 10.1111/j.1600-0870.2011.00543.x.

[72] F. Li et al. ""Super-parameterization": A better way to simulate regional extreme precipitation?" English. In: *Journal Of Advances In Modeling Earth Systems* 4 (2012). ISSN: 1942-2466. DOI: 10.1029/2011MS000106.

[73] S. C. Liu, J. R. Mcafee, and R. J. Cicerone. "Rn-222 and Tropospheric Vertical Transport". In: *Journal Of Geophysical Research-Atmospheres* 89.Nd5 (1984), pp. 7291–7297.

[74] C. Lucas, E. J. Zipser, and M. A. Lemone. "Vertical Velocity In Oceanic Convection Off Tropical Australia". In: *Journal Of The Atmospheric Sciences* 51.21 (1994), pp. 3183–3193.

[75] C. Luo, N. M. Mahowald, and J. del Corral. "Sensitivity study of meteorological parameters on mineral aerosol mobilization, transport, and distribution". In: *J. Geophys. Res.* 108 (D15), 4447 (2003), doi:10.1029/2003JD003483.

[76] N. M. Mahowald, P. J. Rasch, and R. G. Prinn. "Cumulus parameterizations in chemical transport models". In: *Journal Of Geophysical Research-Atmospheres* 100.D12 (1995), pp. 26173–26189. ISSN: 0148-0227.

[77] N. M. Mahowald et al. "Change in atmospheric mineral aerosols in response to climate: Last glacial period, preindustrial, modern, and doubled carbon dioxide climates". In: *J. Geophys. Res.* 111, D10202 (2006), doi:10.1029/2005JD006653.

[78] N. M. Mahowald et al. "Dust sources and deposition during the last glacial maximum and current climate: A comparison of model results with paleodata from ice cores and marine sediments". In: *J. Geophys. Res.* 104 (1999), pp. 15,589–15,916.

[79] N. M. Mahowald et al. "Interannual variability in atmospheric mineral aerosols from a 22-year model simulation and observational data". In: *J. Geophys. Res.* 108(D12), 4352 (2003), doi:10.1029/2002JD002821.

[80] N. M. Mahowald et al. "Model insight into glacialinterglacial paleodust records". In: *Quaternary Science Reviews* 30, 7-8 (2011), 832854.

[81] N. M. Mahowald et al. "Transport Of (222)Radon To The Remote Troposphere Using The Model Of Atmospheric Transport and Chemistry and Assimilated Winds From ECMWF and The National Center For Environmental Prediction NCAR". In: *Journal Of Geophysical Research-Atmospheres* 102.D23 (1997), pp. 28139–28151.

[82] B. Marticorena and G. Bergametti. “Modeling the atmospheric dust cycle: 1. Design of a soil-derived dust emission scheme”. In: *J. Geophys. Res.* 100 (1995), 16415 16430.

[83] B. Marticorena et al. “Modeling the atmospheric dust cycle: 2. Simulation of Saharan dust sources”. In: *J. Geophys. Res.* 102 (1997), 4387 4404.

[84] G. M. Martin et al. “The HadGEM2 family of Met Office Unified Model climate configurations”. English. In: *Geoscientific Model Development* 4.3 (2011), pp. 723–757. ISSN: 1991-959X. DOI: 10.5194/gmd-4-723-2011.

[85] J. H. Martin. “Glacial-interglacial CO2 change: The iron hypothesis”. In: *Paleoceanography* 5(1) (1990), pp. 1–13.

[86] P. T. May and D. K. Rajopadhyaya. “Vertical velocity characteristics of deep convection over Darwin, Australia”. In: *Monthly Weather Review* 127.6, Part 1 (1999), pp. 1056–1071. ISSN: 0027-0644.

[87] R. L. Miller, I. Tegen, and J. Perlwitz. “Surface radiative forcing by soil dust aerosols and the hydrologic cycle”. In: *journal of geophysical research-atmospheres* 109.D4 (2004). ISSN: 2169-897X. DOI: 10.1029/2003JD004085.

[88] S. K. Min et al. “Human contribution to more-intense precipitation extremes”. In: *Nature* 470.7334 (2011), pp. 378–381. DOI: 10.1038/nature09763.

[89] S. K. Min et al. “Signal detectability in extreme precipitation changes assessed from twentieth century climate simulations”. In: *Climate Dynamics* 32.1 (2009), pp. 95–111. DOI: 10.1007/s00382-008-0376-8.

[90] “Multimodel ensemble simulations of present-day and near-future tropospheric ozone”. In: 111 (). URL: http://www.agu.org/pubs/crossref/2006/2005JD006338.shtml.

[91] D. M. Murphy, D. S. Thomson, and T. M. J. Mahoney. “In situ measurements of organics, meteoritic material, mercury, and other elements in aerosols at 5 to 19 kilometers”. In: *Science* 282.5394 (1998), pp. 1664–1669. ISSN: 0036-8075.

[92] K. V. Ooyama. “A dynamic and thermodynamic foundation for modeling the moist atmosphere with parameterized microphysics”. In: *Journal Of The Atmospheric Sciences* 58.15 (2001), pp. 2073–2102. DOI: 10.1175/1520-0469(2001)058<2073:ADATFF>2.0.CO;2.

[93] Enio B. Pereira, Pedro L. Silva Dias, and Daniel J.R. Nordemann. “Radon concentrations profiles over the brazilian Amazon Basin during the wet season”. In: *Revista Brasilera de Geofisica* 91.2 (1991). ISSN: 0102-26 1 X.

[94] J. C. Petch, P. N. Blossey, and C. S. Bretherton. “Differences in the lower troposphere in two- and three-dimensional cloud-resolving model simulations of deep convection”. English. In: *Quarterly Journal Of The Royal Meteorological Society* 134.636 (2008), pp. 1941–1946. ISSN: 0035-9009. DOI: 10.1002/qj.315.

[95] V Ramanathan et al. “Atmospheric brown clouds: Impacts on South Asian climate and hydrological cycle”. In: *Proceedings Of The National Academy Of Sciences Of The United States Of America* 102.15 (2005), pp. 5326–5333. ISSN: 0027-8424. DOI: 10.1073/pnas.0500656102.

[96] V. Ramaswamy et al. “Radiative Forcing of Climate Change in Climate Change 2001: The Scientific Basis. Contribution of Working Group I to the Third Assessment Report of the Intergovernmental Panel on Climate Change”. In: *DJ Griggs, M Noguer, PJ van der Linden, X Dai, K Maskell and CA Johnson (Cambridge: Cambridge University Press) pp* 350 (2001), p. 416.

[97] D. Randall et al. “Breaking the Cloud Parameterization Deadlock”. In: *Bull. Am. Met. Soc* 84 (2003), pp. 1547–1564.

[98] J. L. Raper et al. “Pacific Exploratory Mission in the tropical Pacific: PEM-Tropics B, March-April 1999”. In: *Journal Of Geophysical Research-Atmospheres* 106.D23 (2001), pp. 32401–32425. ISSN: 0747-7309.

[99] P. J. Rasch, N. M. Mahowald, and B. E. Eaton. “Representations of transport, convection, and the hydrologic cycle in chemical transport models: Implications for the modeling of short-lived and soluble species”. In: *J. Geophys. Res.* 102 (1997), 28,12728,138.

[100] P. J. Rasch et al. “A comparison of scavenging and deposition processes in global models: results from the WCRP Cambridge Workshop of 1995”. In: *Tellus B* 52 (2000), 10251056.

[101] P. J. Rasch et al. “A description of the global sulfur cycle and its controlling processes in the National Center for Atmospheric Research Community Climate Model, version 3”. In: *J. Geophys. Res.* 105 (2000), 13671386.

[102] P. J. Rasch et al. “Characteristics of atmospheric transport using three numerical formulations for atmospheric dynamics in a single GCM framework”. In: *Journal Of Climate* 19.11 (2006), pp. 2243–2266. ISSN: 0894-8755.

[103] “Role of Deep Cloud Convection in the Ozone Budget of the Troposphere”. In: 264 (). URL: http://www.sciencemag.org/content/264/5166/1759.abstract.

[104] D. Rosa and W.D. Collins. “A case study of subdaily simulated and observed continental convective precipitation: CMIP5 and multiscale global climate models comparison”. In: *Geophysical Research Letters* 40.22 (2013), pp. 5999–6003.

[105] D. Rosa, J.-F. Lamarque, and W. D. Collins. “Global transport of passive tracers in conventional and superparameterized climate models: Evaluation of multi-scale methods”. English. In: *Journal Of Advances In Modeling Earth Systems* 4 (2012). ISSN: 1942-2466. DOI: 10.1029/2012MS000206.

[106] D. Rosenfeld. “Suppression of Rain and Snow by Urban and Industrial Air Pollution”. In: *Science* 287 (5459) (2000), pp. 1793–1796.

[107] S. H. Schneider et al. *Assessing key vulnerabilities and the risk from climate change, in Climate Change 2007: Impacts, Adaptation and Vulnerability. Contribution of Working Group II to the Fourth Assessment Report of the Intergovernmental Panel on Climate Change*. Ed. by M. L. Parry et al. Cambridge, U. K.: Cambridge Univ. Press, 2007, pp. 779–810.

[108] M. Schulz et al. "Radiative forcing by aerosols as derived from the AeroCom present-day and pre-industrial simulations". In: *Atmospheric Chemistry and Physics* 6 (2006), pp. 5225–5246. ISSN: 1680-7316.

[109] E. Scoccimarro et al. "Effects of Tropical Cyclones on Ocean Heat Transport in a High Resolution Coupled General Circulation Model." English. In: *Journal of Climate* 24.24 (2011), pp. 4368–4384. DOI: 10.1175/2011JCLI4104.1.

[110] J. H. Seinfeld and S. N. Pandis. *Atmospheric Chemistry and Physics*. New York. John Wiley, 1997.

[111] Y. Shao. "A model for mineral dust emission". In: *J. Geophys. Res.* 106 (2001), pp. 20,239–20,254.

[112] Y. Shao and L. M. Leslie. "Wind erosion prediction over the Australian continent". In: *J. Geophys. Res.* 102 (1997), pp. 30,091–30,105.

[113] Y. Shao, M. R. Raupach, and J. F. Leys. "A model for predicting aeolian sand drift and dust entrainment on scales from paddock to region". In: *Aust. J. Soil Res.* 34 (1996), pp. 309–342.

[114] H. B. Singh et al. "Chemistry and transport of pollution over the Gulf of Mexico and the Pacific: spring 2006 INTEX-B campaign overview and first results". In: *Atmospheric Chemistry And Physics* 9.7 (2009), pp. 2301–2318. ISSN: 1680-7316.

[115] H. B. Singh et al. "Overview Of The Summer 2004 Intercontinental Chemical Transport Experiment - North America (Intex-A)". In: *Journal Of Geophysical Research-Atmospheres* 111.D24 (2006). Singh, H. B. Brune, W. H. Crawford, J. H. Jacob, D. J. Russell, P. B. 59 Amer Geophysical Union 118lg, p. 17.

[116] Graeme L. Stephens et al. "Dreary state of precipitation in global models". English. In: *Journal Of Geophysical Research-Atmospheres* 115 (2010). ISSN: 0148-0227. DOI: 10.1029/2010JD014532.

[117] Q. Tang, M. J. Prather, and J. Hsu. "Stratosphere-troposphere exchange ozone flux related to deep convection". In: *Geophysical Research Letters* 38 (2011).

[118] W. K. Tao et al. "A Multiscale Modeling System. Developments, Applications, and Critical issues". In: *Bull. Am. Met. Soc* (2009), DOI:10.1175/2008BAMS2542.1.

[119] Karl E. Taylor, Ronald J. Stouffer, and Gerald A. Meehl. "An Overview Of Cmip5 And The Experiment Design". English. In: *Bulletin Of The American Meteorological Society* 93.4 (2012), pp. 485–498. ISSN: 0003-0007. DOI: 10.1175/BAMS-D-11-00094.1.

[120] I. Tegen and I. Fung. “Contribution to the atmospheric mineral aerosol load from land surface modification”. In: *J. Geophys. Res.* 100 (1995), pp. 18,707–18,726.

[121] I. Tegen and I. Fung. “Modeling of mineral dust in the atmosphere: Sources, transport, and optical thickness”. In: *J. Geophys. Res.* 99 (1994), pp. 22,897–22,914.

[122] H. Tost et al. “Uncertainties in atmospheric chemistry modelling due to convection parameterisations and subsequent scavenging”. In: *Atmospheric Chemistry And Physics* 10.4 (2010), pp. 1931–1951. ISSN: 1680-7316.

[123] S. Twomey. “Pollution And Planetary Albedo”. In: *Atmospheric Environment* 8.12 (1974), pp. 1251–1256. ISSN: 1352-2310. DOI: `10.1016/0004-6981(74)90004-3`.

[124] K. N. Uma and T. Narayana Rao. “Characteristics of Vertical Velocity Cores in Different Convective Systems Observed over Gadanki, India”. In: *Monthly Weather Review* 137.3 (2009), pp. 954–975.

[125] A. Voldoire et al. “The CNRM-CM5.1 global climate model: description and basic evaluation”. English. In: *Climate Dynamics* 40.9-10, SI (2013), pp. 2091–2121. ISSN: 0930-7575. DOI: `10.1007/s00382-011-1259-y`.

[126] B. Wang and Q. H. Ding. “Changes in global monsoon precipitation over the past 56 years”. In: *Geophysical Research Letters* 33.6 (2006). DOI: `10.1029/2005GL025347`.

[127] J. Warner. “A reduction in rainfall associated with smoke from sugar-cane fires: an inadvertent weather modification”. In: *J. Appl. Meteorol.* 7 (1968), 247251.

[128] S. Watanabe et al. “MIROC-ESM 2010: model description and basic results of CMIP5-20c3m experiments”. English. In: *Geoscientific Model Development* 4.4 (2011), pp. 845–872. ISSN: 1991-959X. DOI: `10.5194/gmd-4-845-2011`.

[129] M. F. Wehner et al. “The effect of horizontal resolution on simulation of very extreme US precipitation events in a global atmosphere model”. In: *Climate Dynamics* 34.2-3 (2010), pp. 241–247. DOI: `10.1007/s00382-009-0656-y`.

[130] WHO. *Air Quality Guidelines Global Update 2005: Particulate Matter, Ozone, Nitrogen Dioxide and Sulfur Dioxide.* Copenhagen: WHO Regional Office for Europe, 2006. ISBN: 9289021926.

[131] Alastair G. Williams et al. “The Vertical Distribution of Radon in Clear and Cloudy Daytime Terrestrial Boundary Layers”. In: *Journal Of The Atmospheric Sciences* 68.1 (2011), pp. 155–174.

[132] D. L. Williamson. “Convergence of aqua-planet simulations with increasing resolution in the Community Atmospheric Model, Version 3”. In: *Tellus Series A-Dynamic Meteorology And Oceanography* 60.5 (2008), pp. 848–862. DOI: `10.1111/j.1600-0870.2008.00339.x`.

[133] Tongwen Wu. “A mass-flux cumulus parameterization scheme for large-scale models: description and test with observations”. English. In: *Climate Dynamics* 38.3-4 (2012), pp. 725–744.

[134] S. C. Xie et al. “Intercomparison and evaluation of cumulus parametrizations under summertime midlatitude continental conditions”. In: *Quarterly Journal Of The Royal Meteorological Society* 128.582, Part B (2002), pp. 1095–1135. ISSN: 0035-9009.

[135] K. M. Xu et al. “An intercomparison of cloud-resolving models with the atmospheric radiation measurement summer 1997 intensive observation period data”. In: *Quarterly Journal Of The Royal Meteorological Society* 128.580, Part B (2002), pp. 593–624. ISSN: 0035-9009.

[136] Song Yang and Eric A. Smith. “Convective-stratiform precipitation variability at seasonal scale from 8 yr of TRMM observations: Implications for multiple modes of diurnal variability”. English. In: *Journal Of Climate* 21.16 (2008). 27th Conference on Hurricanes and Tropical Meteorology, Monterey, CA, APR 24-28, 2006, pp. 4087–4114. ISSN: 0894-8755. DOI: 10.1175/2008JCLI2096.1.

[137] X. Yue et al. “Simulation of dust aerosol radiative feedback using the Global Transport Model of Dust: 1. Dust cycle and validation”. In: *J. Geophys. Res.* 114, D10202 (2009), doi:10.1029/2008JD010995.

[138] W. Zahorowski, S. D. Chambers, and A. Henderson-Sellers. “Ground based radon-222 observations and their application to atmospheric studies”. In: *Journal Of Environmental Radioactivity* 76.1-2, Sp. Iss. SI (2004), pp. 3–33.

[139] Charles S. Zender, Huisheng Bian, and David Newman. “Mineral Dust Entrainment and Deposition (DEAD) model: Description and 1990s dust climatology”. In: *J. Geophys. Res.* 108, D14 (2003), doi:10.1029/2002JD002775.

[140] G. J. Zhang and N. A. Mcfarlane. “Sensitivity Of Climate Simulations To The Parameterization Of Cumulus Convection In The Canadian Climate Center General-Circulation Model”. English. In: *Atmosphere-Ocean* 33.3 (1995), pp. 407–446. ISSN: 0705-5900.

[141] K. Zhang et al. “Evaluation of the atmospheric transport in a GCM using radon measurements: sensitivity to cumulus convection parameterization”. In: *Atmospheric Chemistry And Physics* 8.10 (2008), pp. 2811–2832. ISSN: 1680-7316.